Institute of High Pressure Physics
Polish Academy of Sciences

Integrated optical systems based on GaN laser diodes and some applications to spectroscopy

Katarzyna Anna Holc

Ph.D. Disseratation written under the supervision of

doc. dr hab. Piotr Perlin

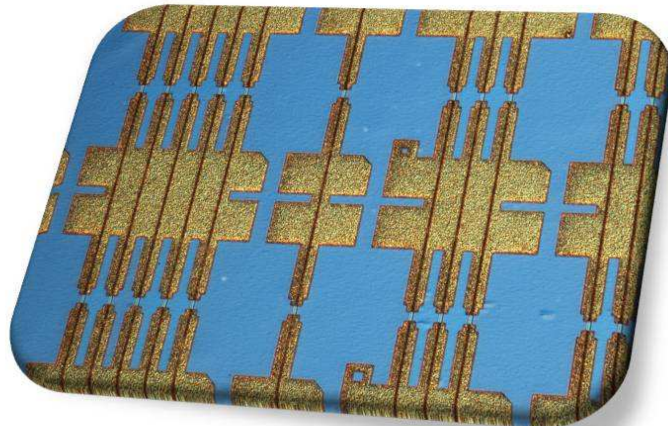

October 2010

Contents

Acknowledgements **III**

Abstract **1**

1 Introduction **7**
1.1 Optical semiconductor devices and their optoelectronic applications 7
1.2 Milestones in the evolution of nitrides 9

2 Lasing action in semiconductor media **13**

3 Laser diode: significance and influence of structure design on laser's performance **19**
3.1 Substrate 20
3.2 Carriers and photon confinement 23
3.2.1 Separate confinement heterostructure 23
3.2.2 Active region – quantum wells 25
3.2.3 Electron Blocking Layer 32
3.2.4 Ridge geometry 32
3.3 Mirrors 33

4 Laser devices **37**
4.1 LD structures under investigation 38
4.2 Typical laser structure 38
4.3 Characterization of LDs 40
4.3.1 Basic operation parameters 41
4.3.2 Optical gain 43
4.3.3 Optical properties 45
4.3.4 Gaussian telescope for near-field to far-field measurements 48
4.4 Optimizing transversal confinement 54
4.4.1 Plasmonic cladding 56
4.4.2 Waveguide mode simulations 59

5 Nitride LDs for spectroscopic applications **65**
5.1 External Cavity Tuning 67
5.1.1 ECDL and tuning results 67

5.2 Temperature tuning 70
5.2.1 Experimental setup and Measured Tuning Range 70
5.3 Cavity Ring Down Spectroscopy 75
5.3.1 NO_2 detection with pulsed diode lasers 76
5.3.2 The outlook: cw LDs for atomic spectroscopy 79

6 SLEDs **81**
6.1 SLED structure and fabrication 82
6.2 Device characterization 83
6.3 Temperature dependence of superluminescence 85

7 Nitride Laser Diode Arrays **91**
7.1 Mini-array structure - first constructions 92
7.1.1 Characterization 93
7.1.2 Optical coupling between emitters 98
7.2 New generation arrays 101

8 Conclusions **105**

Acknowledgements

I would firstly like to acknowledge the role of my supervisor doc. dr hab. Piotr Perlin. I would like to thank him for providing ideas, motivation and advice in all aspects of this research.

I would like to thank prof. Tadeusz Suski for his guidance through the years of my scientific work.

I would also like to thank prof. Ulrich Schwarz for providing the opportunity to visit Regensburg and perform optical characterization measurements. I thank him for many discussions and guidance during our collaboration. Additionally, I would like to acknowledge support I received from all group members from the Regensburg University, in particular Harald Braun and Wolfgang Scheibenzuber.

I would like to thank prof. Tadeusz Stacewicz, Jacek Wojtas, Adam Czyzewski and prof. Zbigniew Bielecki for offering the opportunity to participate in CRDS measurements.

Also I would like to thank prof. Witold Trzeciakowski for encouraging me to start my PhD research.

Additionally, I would like to thank all my colleagues from Unipress and TopGaN, in particular:
– Szymon Grzanka for many discussions and useful remarks,
– Robert Czernecki, Grzegorz Targowski, Marcin Sarzynski, Jurek Plesiewicz for growing samples for my research,
– the whole processing group: Agnieszka Sarzynska, Agata Bering, Wojtek Purgal, Robert Jachymek, Jacek Kacperski, Wiktor Krupczynski, Sylwia Celinska, Adam Libura, Grzegorz Nowak, Renata Wisniewska, Irina Makarowa and Ania Nowakowska-Siwinska for fabricating wonderful devices,

– Przemek Wisniewski and Aleksander Khachapuridze for their remarks on technical issues,
– Jacek Walenta for his advice and support in realizing my constructions, and for his many amusing stories,
– Jakub Goss, Lucja Marona and Grzegorz Staszczak for cooperation, support and nice atmosphere.

Special thanks to my friend, Dodo!

Above all, I would like to thank Janek. Without his constant support, enormous patience and love many things would just not be possible.

Abstract

The progress in design and fabrication of nitride LDs allowed them to reach certain maturity. Based on the experience gained on laser diodes, constructions of more complex systems became possible. The newly designed optical devices are of great interest due to many existing and potential applications.

The following dissertation addresses issues related to integrated optical devices based on the construction of a conventional nitride laser diode of ridge-type waveguide. In the introductory part, early stages of nitride research (Chapter 1) and the principles of laser diode operation (Chapter 2) are presented. In Chapter 3 the design of a nitride laser diode structure is discussed in more detail.

The second part of the dissertation presents results of my research carried out at the Institute of High Pressure Physics, Polish Academy of Sciences. Chapter 4 is devoted to the study (both experimental and theoretical) on the internal structure of an InGaN laser diode, in particular to the problem of the transversal confinement of the optical mode. Drawing on the experience which I gained during my visit to Regensburg University, I developed a measurement setup, which allows to measure the near-field of LDs and laser-based integrated structures and now serves as a part of a standard characterization of devices fabricated at the Institute of Physics, Polish Academy of Sciences and its *spin-off* TopGaN Ltd.

In Chapter 5 the issues of adapting InGaN LDs to molecular and atom spectroscopy are addressed. In particular, tuning of a laser diode by means of external cavity (formed by a diffraction grating) and by means of temperature are discussed. Next, an example of NO_2 detection on a single *ppb* level using Cavity Ring Down Spectroscopy is reported. A construction of an external cavity frequency stabilized laser diode using Littrow configuration is described.

Chapter 6 introduces second in the world demonstration of Superluminescent Light Emitting Diodes, and describes in detail the study on temperature characteristics of these devices.

Finally, Chapter 7 deals with the integrated systems of mini laser arrays, where a systematic characterization of these systems is presented. The research showed that for old epitaxial design the mini-arrays were optically coupled through the leaking mode due to insufficient transversal optical confinement. The new generation of arrays did not show any coupling.

Research results presented throughout this dissertation have been published in the following articles:

1. **K. Holc**, A. Sarzynska, M. Bockowski, R. Czernecki, M. Leszczynski, T. Suski, R. Kucharski and P. Perlin, ***InGaN mini-laser diode arrays with cw output power of 500 mW***, Phys. Status Solidi C (accepted for publication).

2. **K. Holc**, Z. Bielecki, J. Wojtas, P. Perlin, J. Goss, A. Czyzewski, P. Magryta and T. Stacewicz, ***Blue laser diodes for trace matter detection***, Optica Applicata **40** (3), pp. 641-651 (2010).

3. **K. Holc**, L. Marona, R. Czernecki, M. Bockowski, T. Suski, S. Najda, and P. Perlin, ***Temperature dependence of superluminescence in InGaN-based superluminescent light emitting diode structures***, J. Appl. Phys. **108**, 013110 (2010)

4. P. Perlin, **K. Holc**, M. Sarzynski, W. Scheibenzuber, L. Marona, R. Czernecki, M. Leszczynski, M. Bockowski, I. Grzegory, S. Porowski, G. Cywinski, P. Firek, J. Szmidt, U.T. Schwarz, and T. Suski, ***Application of a composite plasmonic substrate for the suppression of an electromagnetic mode leakage in InGaN laser diodes***, Appl. Phys. Lett. **95**, 261108 (2009)

5. **K. Holc**, M. Leszczynski, T. Suski, R. Czernecki, H. Braun, U. Schwarz, and P. Perlin, ***Nitride laser diode arrays***, SPIE proceedings **7216**, 721618 (2009)

6. **K. Holc**, P. Wisniewski, M. Leszczynski, T. Suski, I. Grzegory,R. Czernecki, S. Grzanka and P. Perlin, ***Violet blue laser mini-bars***, Phys. Status Solidi C **6**, No. S2, S837-S839 (2009)

7. Z. Bielecki, M. Leszczynski, **K. Holc**, L. Marona, J. Mikolajczyk, M. Nowakowski, P. Perlin, B. Rutecka, Tadeusz Stacewicz, J. Wojtas, ***Sub-ppb NO_x detection by a cavity enhanced absorption spectoscopy system with blue and infrared diode lasers***, Transactions on Modeling and Computer Simulation **48**, 203-215 (2009)

8. **K.Komorowska**, P.Perlin, M.Leszczynski, R.Czernecki, I.Grzegory, S.Porowski, T.Stacewicz, J.Goss, J.Wojtas, Z.Bielecki, A.Czyzewski, ***Zastosowanie niebieskich laserow do detekcji substancji sladowych***, VII Krajowa Konferencja Elektroniki, Materialy konferencyjne, t. **1**, str. 169, (2008)

9. **K. Komorowska**, P. Wisniewski, R. Czernecki, P. Prystawko, M. Leszczynski, T. Suski, I. Grzegory, S.Porowski, S. Grzanka, T. Swietlik, L. Marona, T. Stacewicz, P. Perlin, ***16 nm tuning range of blue InGaN laser diodes achieved by 200 K temperature increase*** (Proceedings Paper), Proceedings Vol. **6894**, Gallium Nitride Materials and Devices III, 68940Q (2008)

10. **K. Komorowska**, P. Wisniewski, R. Czernecki, P. Prystawko, M. Leszczynski, T. Suski, I. Grzegory, S.Porowski, S. Grzanka, M. Maszkowicz, P. Perlin, ***Tunable broad-area InGaN laser diodes in external cavity*** (Proceedings Paper), SPIE Proceedings Vol. **6485**, Novel In-Plane Semiconductor Lasers VI, 648502 (2007)

Other papers published in international journals:

11. P. Perlin, P. Wisniewski, R. Czernecki, P. Prystawko, M. Leszczynski, T. Suski, I. Grzegory, L. Marona, T. Swietlik, **K. Komorowska**, S. Porowski, ***Load dislocation density broad area high power CW operated InGaN laser diodes*** (Proceedings Paper), SPIE Proceedings Vol. **6184**, Semiconductor Lasers and Laser Dynamics II, 61840H (2006)

12. A. Bercha, F. Dybala, **K. Komorowska**, P. Adamiec, R. Bohdan, W. Trzeciakowski, J. A. Gupta, P. J. Barrios, G. J. Pakulski, A. Delage, Z. R. Wasilewski, ***Pressure tuning of GaInNAs laser diodes in external cavity*** (Proceedings Paper), SPIE Proceedings Vol. **5722**, Physics and Simulation of Optoelectronic Devices XIII, pp.565-572 (2005).

The results were also presented in at the following international conferences:

- 2010, September 19-24, International Workshop on Nitride Semiconductors (IWN2010) (Tampa, USA)
  Title: *Optimizing Waveguide Design for InGaN Laser Diodes Using a Composite Plasmonic Substrate* (ORAL PRESENTATION)
  Title: *InGaN Mini- Laser Diode Arrays with CW Output Power of 500 mW* (ORAL PRESENTATION)

- 2010, September 13-17, E-MRS 2010 Fall Meeting (Warsaw, Poland)
  Title: *Optical characterization of InGaN/GaN laser diode arrays* (INVITED TALK)

- 2010, June 19 - 24, XXXIX "Jaszowiec" International School and Conference on the Physics of Semiconductors (Krynica, Poland)
  Title: *Temperature dependence of superluminescence in blue InGaN Superluminescent LEDs* (POSTER)

- 2009, June 19 - 26, XXXVIII International School and Conference on the Physics of Semiconductors "Jaszowiec" 2009 (Krynica, Poland)
  Title: *Coupling of optical modes in gallium nitride based, multi-emitter laser diode structures* (ORAL PRESENTATION)

- 2008, October 6 - 10, International Workshop on Nitride Semiconductors, IWN2008 (Montreux, Switzerland)
  Title: *High power blue laser mini-bars* (ORAL PRESENTATION)

- 2008, June 7 - 13, XXXVI International School on the Physics of Semiconducting Compounds "Jaszowiec 2008" (Jaszowiec, Poland)
  Title: *High power blue laser mini-bars* (POSTER)

- 2008, January 19 - 24, SPIE Photonic West 2008 (San Jose, USA), Gallium Nitride Materials and Devices III

Title: *16nm tuning range of blue InGaN laser diodes achieved by 200K temperature increase* (ORAL PRESENTATION)

- 2007, June 9 - 15, XXXVI International School on the Physics of Semiconducting Compounds "Jaszowiec 2007" (Jaszowiec, Poland)
  Title: *External Cavity and Temperature Tuning of Broad-Area InGaN Laser Diodes* (ORAL PRESENTATION)

- 2007, January 20 - 25, SPIE Photonic West (San Jose, USA), OPTO 2007
  Title: *Tunable broad - area InGaN laser diodes in external cavity* (ORAL PRESENTATION)

Chapter 1

Introduction

1.1 Optical semiconductor devices and their optoelectronic applications

Looking back on its history, semiconductor technology and the development of semiconductor based optoelectronics achieved tremendous success providing a variety of devices that served as light sources in many different applications. The highlights are light emitting diodes (LEDs), considered as perfect replacement for incandescent lamps due to their reliability, high brightness and low power consumption. Nowadays they are commonly used e.g. in traffic lights, screen displays or as interior lightning in cars, buses and trains.
One of the most powerful and bright example are semiconductor laser diodes (LDs), which became more and more frequently utilized type of laser device. The wavelength range covered with semiconductor LDs extends from approximately $0.3\,\mu m$ to around $11\,\mu m$, if we consider only the *conventional* semiconductor lasers, where the emission wavelength depends on the semiconductor bandgap.[1]
Numerous applications and commercial perspectives have drown considerable attention of many research groups and companies, starting in the early 1960ties. In the beginning, the main interest was concentrated on optical information storage – introducing compact discs (CDs) had revolutionized data storage systems throughout the world. A very important application was in communication solutions, in which LDs served as carrier and pumping sources. Finally, high power LDs were widely employed in optical pumping of YAG lasers.

[1]With quantum cascade lasers (QCLs), relaying on intraband transitions, the range spreads to the mid-infrared (3 - 25 μm) and to a large part of the far-infrared region (50-300 μm).

In view of promising progress in the long wavelengths region a lot of effort was put into shifting the emission towards green and blue. II-VI group of semiconductors was explored to go from green (CdZnSe) to blue (ZnSe) emitters. Unfortunately, despite major research worldwide, ZnSe blue light-emitting devices suffered from very short lifetimes due to defects in the material that quenched the light emission. Availability of efficient and reliable short-wavelength emitters was finally set up with the choice of nitride materials – GaN, AlN and InN and their ternary and quaternary compounds. However, before reaching maturity in their fabrication, many technological obstacles had to be overcome. The room-temperature band gap energy of AlGaInN compounds extends from $0.7\,eV$ for pure InN through $3.4\,eV$ for GaN to $6.2\,eV$ for AlN and can be controlled by alloy composition. This direct bandgap material system features not only the capability of band engineering from infrared to ultraviolet emission wavelengths, but also excellent physical and chemical stability as well as exceptional thermal conductivity, all equally important from the point of view of practical applications. With the advent of nitrides, emitters of the three primary colors (red, green and blue) became available, which made it finally possible to obtain efficient white-light emitters as well as full-color and large-screen displays. Recent display applications like pocket projectors or laser TV are already in advanced stage of development. Shorter wavelengths also mean smaller size of focusing spot, determined by the diffraction limit, which is inversely proportional to the square of the wavelength. Thus new optoelectronic applications like *Blu-ray* disks with increased storage capacity or improved resolution of printing devices, employing laser diodes and laser diode arrays, are only first advantages to be disclosed.

At this point one should also mention spectroscopic applications of optoelectronics of which major part is based on laser spectroscopy. Semiconductor LDs are frequently employed not only due to their reliability and compact size, but mostly because they can be designed for a specific wavelength owing to band engineering. Additional advantage comes from the unique possibility of further adjustment of the emitted radiation through wavelength tuning, by means, e.g. of temperature or in external cavity set-ups, which facilitates tuning into the resonant transition lines of the analyzed samples.

Benefits from the above mentioned aspects can be found not only in the field of basic research but also in many practical applications – detectors and sensors of chemical and biological species, environmental pollutants, drugs and cancer

recognition, or detection of certain explosive materials. One of particularly interesting application, a novel type of device in the blue spectral range, is a Superluminescent Light Emitting Diode (SLED) which has unique properties of spatial coherence (similar to laser diodes) combined with broadband, continuous emission (similar to LEDs) and which is used in biomedical and industrial imaging based on optical coherence tomography (OCT).

1.2 Milestones in the evolution of nitrides

Report on fabrication of the first gallium nitride based LED, by *Pankove et al.* date to 1971 [1]. However, most of the early research programs in nitride technology were unsuccessful, and eventually abandoned, due to fundamental material problems. Thermodynamic properties of GaN, in particular extreme melting point conditions with melting temperature of around 2220 °C obtained under equilibrium nitrogen pressure of $6\,GPa$ [2] excluded standard techniques of growing high quality bulk crystals from a stoichiometric solution by the Czochralski or Bridgman methods, commonly used in other material systems.

As no suitable bulk-crystal technology for producing gallium nitride substrates was available, heteroepitaxy had to be applied. In consequence of high lattice mismatch, thermal-expansion-coefficient differences and chemical incompatibility, nitride epilayers exhibited high dislocation densities and poor surface morphology. First GaN layers on sapphire were obtained from a vapor phase by Hydride Vapor Phase Epitaxy (HVPE) [3], in which gallium was transported as a chloride after a reaction with HCl gas. As for the source of nitrogen, NH_3 was used, and the applied growth temperature of GaN epilayers was around 900 °C. The high n-type background doping was inherent with the growth method due to unintentional contamination with oxygen, which eventually hampered successful fabrication of p-type materials for almost two decades.

Development of the Metal Organic Chemical Vapor Deposition (MOCVD) [4] brought in the mid 1980ties the idea to use low temperature nucleation layers of AlN [5, 6] and GaN [7], which resulted in in a successful growth of high quality GaN films with mirror-like flat surfaces, despite a 15% lattice mismatch between a sapphire substrate and GaN.

The above mentioned problem of fabricating a p-type material was of major concern for the early research in nitrides. Three factors delimited obtaining sig-

nificant p-type conduction: hydrogen passivation of acceptors, low p-type carrier mobility, and high background n-type carrier concentrations. In the beginning all nitride material that was doped with acceptors had dopant levels that were too deep, dopants that were passivated by hydrogen atoms, or too few dopants to achieve net p-type conduction. Magnesium was the most promising candidate for an effective acceptor impurity. However, large concentrations of Mg were required due to the relatively high (between 150-250 meV in GaN) ionization energy limiting the fraction of activated ions to 1% at room temperature. The most significant problem was hydrogen passivation of acceptors. Molecular hydrogen served as the carrier gas for ammonia during the MOCVD process. In addition to ammonia-induced compensation, electrically inactive Mg-H complexes were formed and thus magnesium no longer contributed p-type carriers. In 1989 Amano *et al.* obtained p-type conductivity from initially highly resistive Mg-doped GaN applying a post-growth irradiation by a low-energy electron beam (LEEBI). The research was followed by a demonstration of the first III-nitride-system-based p-n junction LED [8].

The origin of the acceptor compensation mechanism was not correctly recognized until 1992, when Nakamura *et al.* demonstrated that Mg-doped GaN could also be made conductive by thermal annealing (700 °C) in an N_2 ambient [9]. The process was observed to be reversible with the GaN reverting to insulating compensated material when annealed under NH_3. Hydrogen was thus identifed as the critical compensating agent. The discovery was further confirmed by theoretical calculations by Neugebauer *et al.* [10].

Another breakthrough was associated with further improvements of the MOCVD technique, leading to a successful deposition of a high quality InGaN layers, designed to form the active region of the blue light emitting devices. Using a self-designed two-flow MOCVD reactor Nakamura *et al.* [11] succeeded in growing an InGaN/GaN multiple quantum well (MQW) structure with enhanced photoluminescence intensity at room temperature [12]. This was the starting point for the mass production of bright blue and green LEDs, deposited on sapphire substrates. Soon thereafter further optimization of the growth technology and improvement in the structure design promoted a demonstration of the first room temperature (RT) pulse-operated LD [13], followed by a fabrication of the first room-temperature III-nitride-system-based LD working in continuous wave (cw) regime [14]. Further improvements including a demonstration of strained

AlGaN/GaN superlattices, which allowed to grow thicker cladding layers [15] and finally obtaining low defect density GaN substrates by epitaxial lateral overgrowth (ELO) [16] successfully prolonged the devices lifetimes and led to commercialization of the entire production technology [17].

Chapter 2

Lasing action in semiconductor media

To understand the concepts that make laser diodes work some basics to the principles of their operation are needed. Semiconductors, in the very beginning, were not even considered for lasers as they are absorptive and would attenuate the band-edge light emission. Clearly, the view has changed after discovering that a semiconductor can be made transparent by optically or electrically injecting large concentrations of electrons and holes into the lasing medium via a *p*-*n* junction.

Lasing action is a consequence of several intricate processes, which take place simultaneously in a semiconductor medium. There are three basic radiative transitions describing the interaction between light and matter. The situation, where the injected electrons can recombine with holes to give off photons is termed *spontaneous emission*, wherein spontaneous means that the probability of the process does not depend on the presence of other photons. In a different process termed *absorption*, a photon can be taken up by a valence electron exciting the latter into the conduction band. Of particular interest is *stimulated absorption* in which the probability depends on the presence of other photons of the same energy. Finally, when accompanied by another photon, a conduction band electron recombines with a hole creating a new photon, *stimulated emission* occurs. The newly generated photon shares the same phase, direction, energy, and polarization as the stimulating one, contributing to amplification of the electromagnetic wave. A scheme of all three processes is shown in Fig. 2.1.

Conditions that lead to lasing in a semiconductor medium require considering all three radiative processes, which occur simultaneously and which are strong

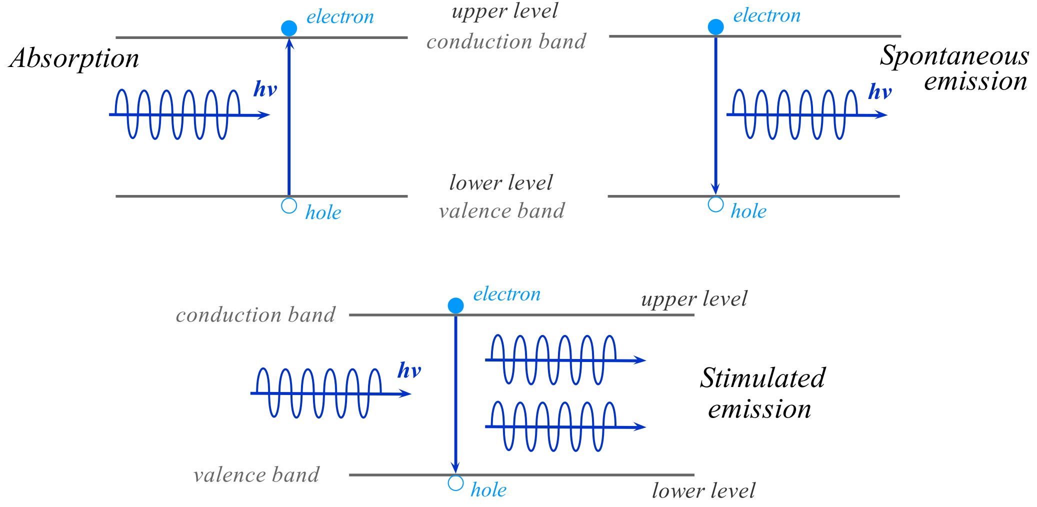

Figure 2.1: Schematic diagrams of three basic radiation processes: *(stimulated) absorption, spontaneous emission and stimulated emission.*

functions of the conduction and valence band structures. In the absence of the stimulated emission, the light is attenuated and overall losses are experienced, therefore no lasing can be obtained. The opposite situation, when stimulated emission occurs (which is only possible beyond transparency), gain is achieved sustaining the electromagnetic wave.

In order to reach lasing the stimulated emission must dominate over the absorption process. This means that non-equilibrium conditions need to be imposed upon the carrier distributions, resulting in a higher population of free carriers in the upper state (conduction band) than in the lower state (valence band), which is described as a *population inversion*. The occupation probabilities for energy levels E_2 and E_1 of the conduction and valence bands (f_2 and f_1, respectively) can be described applying Fermi statistics even under non-equilibrium conditions. Using a separate *quasi-Fermi level* the occupation probabilities are [18]:

$$\text{valence band} \qquad f_1 = \frac{1}{e^{(E_1 - E_{Fv})/kT} + 1} \tag{2.1a}$$

$$\text{conduction band} \qquad f_2 = \frac{1}{e^{(E_2 - E_{Fc})/kT} + 1} \tag{2.1b}$$

When the semiconductor is pumped beyond transparency, in terms of population it means that the separation between the quasi-Fermi levels of the conduction E_{Fc}

and the valence E_{Fv} bands is greater than the semiconductor bandgap E_g [18]:

$$E_{Fc} - E_{Fv} > E_g \tag{2.2}$$

This condition demands that the voltage across a *p*-*n* junction must be greater than the bandgap to achieve gain in the active region.

Fig. 2.2 schematically shows the upward and downward transitions across the bandgap, illustrating the previously mentioned processes. Initially the top of the valence band is filled with electrons. With photon absorption (*step 1* in Fig. 2.2a) optical exctitation occurs, transferring the electron vertically from a deeper state within a valence band into the conduction band. The vertical transition denote the momentum conservation (the photon momentum is negligible). Almost instantly the excited electron thermalizes down to the bottom of the conduction band, depicted as *step 2* in Fig. 2.2a. The process of thermalization is determined by the rate of dominant scattering mechanism, which is polar optic phonon scattering in compound semiconductors taking place at picosecond scale [19]. Having an electron at the bottom of the conduction band and a hole at the top of a valence band means that population inversion is created. The condition is retained for a time period of the order of $1\,ns$, which corresponds to recombination time of an electron with a hole at the top of the valence band (*step 3*). Again, a thermalization process occurs and the electron nearly instantly leaves the top of the valence band, which is illustrated by *step 4*. The idea of transparency illustrates the diagram shown in Fig.2.2b, where the separation between energy levels E_2 and E_1 (defining absorption) is larger than the photon energy created through recombination from the bottom of the conduction band to the top of the valence band.

Finally, when the semiconductor is pumped and transparent, the optical electromagnetic wave can be amplified owing to the conversion of the medium from an absorptive to an amplifying one. Illustrated in Fig. 2.2c, the loss in a semiconductor is a function of energy. When approaching transparency by optical or electrical pumping, the loss is reduced towards zero at the onset of transparency and transformed into gain. For photon energies exceeding the separation of quasi-Fermi levels, the gain changes to loss. If the pumping level is increased, the separation between the quasi-Fermi levels is greater and the gain extends to higher energies [19].

Obtaining photon densities high enough to reach lasing was a non-trivial problem.

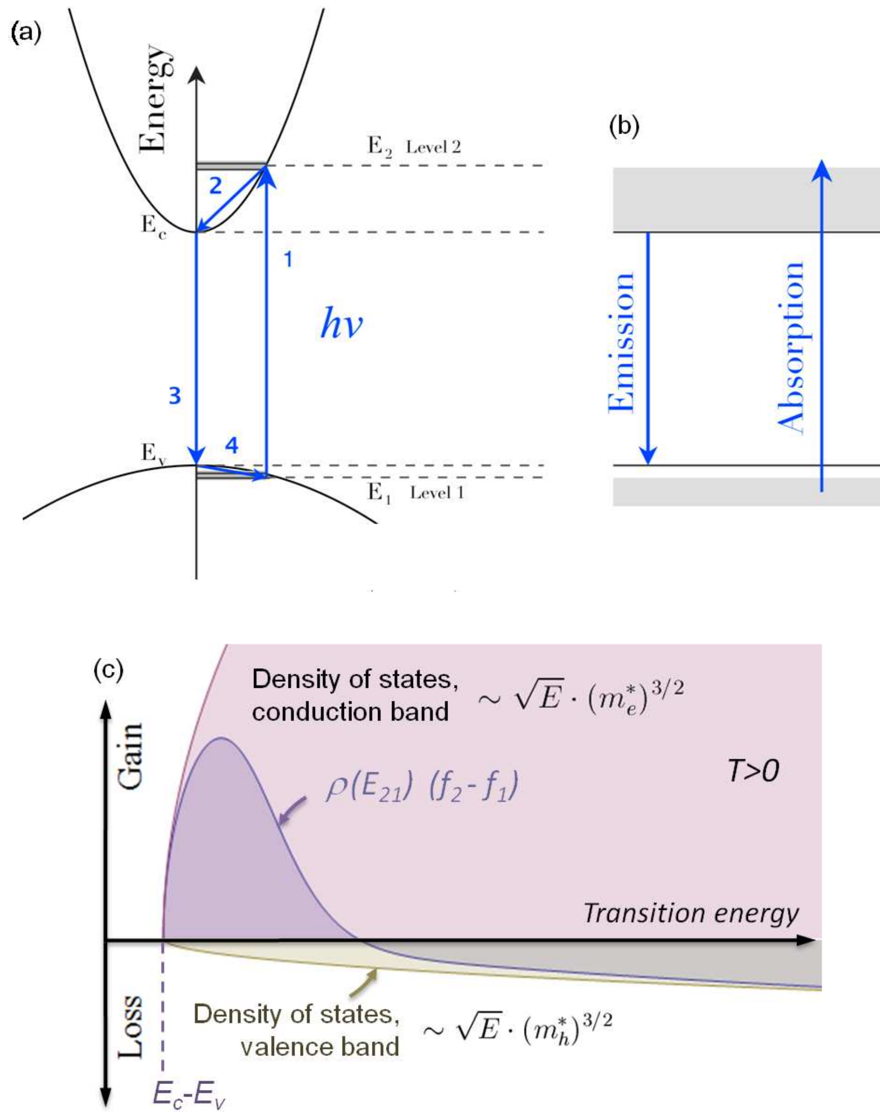

Figure 2.2: Optical transitions in semiconductors: (a) excitation (process 1), followed by relaxation to the bottom of the conduction band (process 2, $\tau \sim 10^{-12}\,s$), radiative recombination with photon emission (process 3, carrier lifetime - time interval before recombination - $\sim 10^{-9}\,s$) and electron relaxing to a hole state created by process 1 (process 4); (b) schematic representation of absorption and emission processes in a semiconductor beyond transparency; (c) gain/loss diagram for a semiconductor at T $> \ 0\,K$ for a pumping level beyond transparency. Profile of the gain curve is determined by the product of the joint density of states and the Fermi factor.

In the early stages of GaAs lasers bulk p-n junctions were used and only gain guiding induced by injection of electrons existed. Because of the large volumes that had to be pumped, operation was limited to only cryogenic temperatures. With the introduction of double heterostructures it became possible to confine both the carriers and the optical field to a very small volume maximizing the stimulated emission, which allowed for both room temperature and continuous (cw) operation. Details of the waveguide design will be the subject of a closer analysis presented in chapters 3 and 4.

Chapter 3

Laser diode: significance and influence of structure design on laser's performance

A semiconductor laser diode is a highly directional and nearly a monochromatic light source that emanates from a leaky optical cavity [19]. When electrically driven, the carriers (electrons and holes) are injected into the active region, where they can recombine radiatively and the process of light amplification occurs, provided the gain is adequate to stimulated operation. One of the unique attributes of those lasers is the built-in optical waveguide, which is realized by manipulating the composition of alloys that contrast in the refractive index and energy bandgap, and which is termed *heterostructure* design. Waves encountering the total internal reflections are supported by the waveguide and are called the waveguide modes. In case of *in-plane* LDs, the structure comprises a three dimensional optical cavity with three distinct waveguide modes, namely: *lateral* – which is in plane of the epitaxially grown layers, *transversal* – perpendicular to the epilayers and *longitudinal* which is the direction of the light propagation along the laser's waveguide. The latter is the direction in which an optical feedback is provided through cavity mirrors, which completes the condition for lasing action. In this chapter an overview on the construction of a laser diode will be presented, briefly discussing the design and its influence on the overall performance of a laser. Fig.3.1 shows a scheme of a LD structure, the next sections analyze key aspects of the construction of nitride lasers.

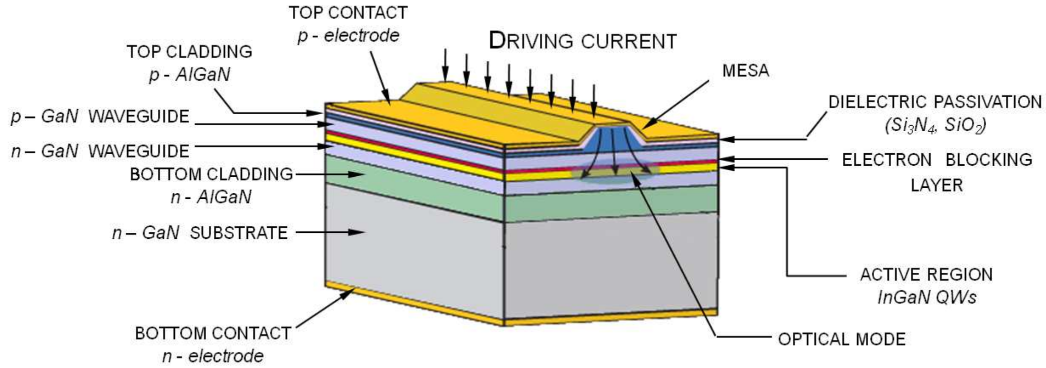

Figure 3.1: A scheme of an *in-plane* ridge-waveguide laser diode.

3.1 Substrate

The choice of a proper substrate material for the growth of GaN and nitride-based structures for many years was burdened with plenty of nontrivial difficulties due to the lack of the native GaN bulk crystals. Majority of the problems that hindered the progress in nitrides had two main origins of which the lattice mismatch was responsible for stacking faults and dislocations, whereas the thermal mismatch caused epilayers to crack on cooling during the growth and post-growth processes.

GaN, AlGaN and InGaN were grown primarily on $(0\,0\,0\,1)$ - sapphire, but also on other surfaces, namely $(2\,1\,\bar{3}\,1)$, $(1\,1\,0\,\bar{1})$, $(1\,\bar{1}\,0\,2)$ and $(1\,1\,\bar{2}\,0)$. Besides, the III–V nitrides were tried on a plethora of substrates: SiC, Si, NaCl, GaP, InP, ZnO, $MgAl_2O_4$, TiO_2, and MgO [20]. The lattice-mismatch lead to a substantial density of misfit and threading dislocations, which was in the range of $10^8 - 10^{10}\,cm^{-2}$. A partial solution to this problems came with the selective epitaxy followed by coalescence, which went by many names in literature, such as epitaxial lateral overgrowth (ELO), lateral epitaxial overgrowth (LEO), and epitaxial lateral overgrown GaN (ELOG). The approach allowed for reduction of dislocation densities down to $10^6\,cm^{-2}$.

The basic concept of the method was to reduce defect propagation in masked regions of the substrate where the laterally overgrown GaN was defect free (see Fig. 3.2). For example, Nakamura developed the ELOG technique, in which a silicon dioxide mask was used to block dislocation propagation, and a "defect-free"film was achieved in the laterally overgrown region. After 100 microns of growth, a fully coalesced GaN thin film was obtained, and a proprietary (*Nichia*)

process removed the sapphire substrate. Laser diodes with InGaN/GaN multiple quantum well (MQW) active regions were then grown on top of such virtual bulk GaN substrate. The active regions were thus defect free and could operate under high current densities ($3\,kA/cm^2$) [21].
Studies of the optical properties of LEO GaN [22, 23] and InGaN quantum wells [24] have revealed that threading dislocations act as non-radiative recombination centers, which manifest themselves as energy states in the forbidden energy bandgap reducing the quantum efficiency as well as producing scattering centers. Other adverse effects of structural and point defects are that impurities diffuse more readily along threading dislocations, and carrier transport is either impeded, as in lateral transport, or aided, as in vertical transport [20].
The minority carrier diffusion length ($\sim 200\,nm$) is smaller than the average distance between threading dislocations, so the emission mechanisms of the carriers that do recombine radiatively appear to be unaffected by moderate threading dislocation densities ($\sim 10^6 - 10^9\,cm^{-2}$). However, reduction of those defects results in suppression of the reverse leakage current by approximately 3 orders of magnitude in GaN p-n junctions [25], and in InGaN single [26] and multiple [27] quantum well LEDs. The use of epitaxial lateral overgrown GaN has also resulted in marked improvements of InGaN/GaN laser diodes lifetimes [28].

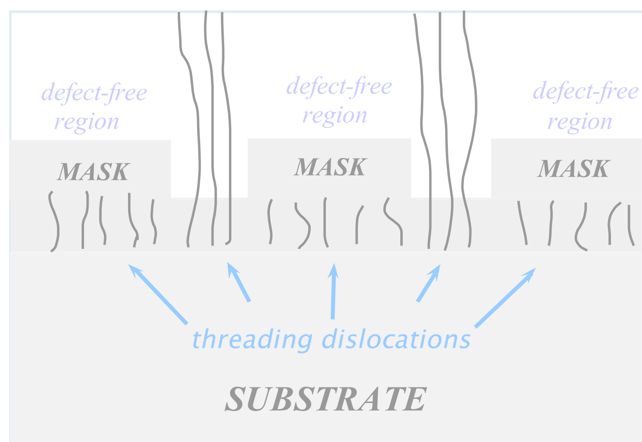

Figure 3.2: The idea of an ELOG: Epitaxial Lateral Overgrown GaN. Mask regions are fabricated with SiO_2 layers. During re-growth process dislocations propagate in the opened regions, leaving the masked areas defect-free.

State-of-the-art in the GaN substrate technology is based mainly on hydride vapor phase epitaxy (HVPE) [29, 30]. The strong point of this technology is its ability to

produce at high growth rates relatively thick films of high quality, which after delamination from a sapphire or other material substrate could be further used as a quasi-substrate, being frequently termed as *freestanding GaN*. Unfortunately, due to the lack of native seeds, the freestanding GaN is bowed and not stress-free. In addition to HVPE, which can produce substrates with dislocation densities close to $10^4 - 10^5\,cm^{-2}$ there is the high-pressure high-temperature (HPHT) growth method, combining high temperatures (of about 1500 °C) with extremely high nitrogen pressure ($\sim 15\,kbar$),which can give the ultimate in terms of low defect density [31]. Such high pressures, however, prevent the use of large growth chambers. This imposes limitations on crystals size, which are typically not larger than an inch in diameter.

Table 3.1: State of the art in GaN substrate technology.

Technology	Supplier	Typical dislocation density	Target applications
HVPE	Sumitomo Electric *(Japan)*	$\sim 10^4\,cm^{-2}$	405 nm LDs for *Blu-ray* discs and Sony PS3
	Kyma Technologies *(USA)*	$5 \cdot 10^6\,cm^{-2}$	LEDs
	TDI Oxford Instruments *(UK)*	$10^4 - 10^5\,cm^{-2}$	high brightness LEDs, LDs, HEMTs
	Lumilog *(France)*	$\sim 10^6\,cm^{-2}$	LEDs
	Hitachi Cable *(Japan)*	$10^5 - 10^6\,cm^{-2}$	LEDs, LDs
	Mitsubishi Chemical *(Japan)*	$\sim 2 \cdot 10^5\,cm^{-2}$	LEDs
	TopGaN *(Poland)*	$10^5 - 10^6\,cm^{-2}$	LDs
HPHT	TopGaN *(Poland)*	$10^2\,cm^{-2}$	LDs
Ammonothermal growth	Ammono *(Poland)*	$5 \cdot 10^3\,cm^{-2}$	bulk substrates for LDs, LEDs, HEMTs

Progress in GaN substrate fabrication is very much anticipated with the recently developed technique of ammonothermal growth [32, 33] of truly bulk gallium nitride crystals of excellent quality with the lowest defect densities uniformly distributed over the large 2-inch, strain-free, mirror-like flat wafers. From the point of view of their fabrication, the growth processes are highly controllable and reproducible at relatively low process temperatures ($500 - 600\,°C$) and pressures ($0.2 - 0.5\,GPa$) and are relatively easy scalable. An overview of presently available substrates is given in Table 3.1, where methods of fabrication, crystal quality and leading suppliers are compared.

3.2 Carriers and photon confinement

The importance of incorporating proper confinement into a LD structure was already announced in the previous sections. Confinement of carriers in transversal direction is realized by a thin slab of undoped active material sandwiched between p- and n-type cladding layers which have a higher conduction–valence band energy gap. Because the bandgap of the cladding layers is larger, light generated in the active region will not have sufficient photon energy to be absorbed in them, i.e. $E_{21} = h\nu < E_{g_{cladding}}$. Under forward bias, electrons and holes are injected from the n-type and p-type regions into the active region, where they are confined through the potential barrier. Due to the fact that gain is a function of carrier density and of the Fermi factor ($f_2 - f_1$), quantum wells are used for efficient carrier confinement. In consequence, an increase of the radiative recombination rate and simultaneously a decrease in the recombination lifetime are observed. However, a slight modification to the design is needed, which is termed *separate confinement heterostructure (SCH).*

3.2.1 Separate confinement heterostructure

To minimize the material volume to be pumped for obtaining population inversion and thus to make the injection current that is required to reach the transparency condition as small as possible, a very thin active regions, quantum wells, are used. Such a construction provides much better confinement of carriers but also leads to a substantial reduction of losses, minimizing the number of undesired recombination centers (such as dislocations) introduced into the active region. However, as a quantum well thickness is only of a few nanometers, proper waveg-

uiding of the optical mode is needed. Figure 3.3 (after Ref.[19]) illustrates the idea of a construction, in which InGaN quantum well region is surrounded by an intermediate bandgap GaN *separate* photon *confinement* region and sandwiched between the large bandgap p- and n- type AlGaN cladding layers. The thickness and composition of the cladding layers have a profound influence on the laser's performance since insufficient confinement of the optical mode results in the leakage of the radiation. In consequence of the optical field escaping from an unoptimized waveguide to a transparent substrate, pumping of the structure to reach lasing is very difficult, if not impossible, and requires very high driving currents. The problem of the mode leakage from the n- type cladding, giving rise to substrate modes will be the subject of a detailed study reported in Chapter 4.

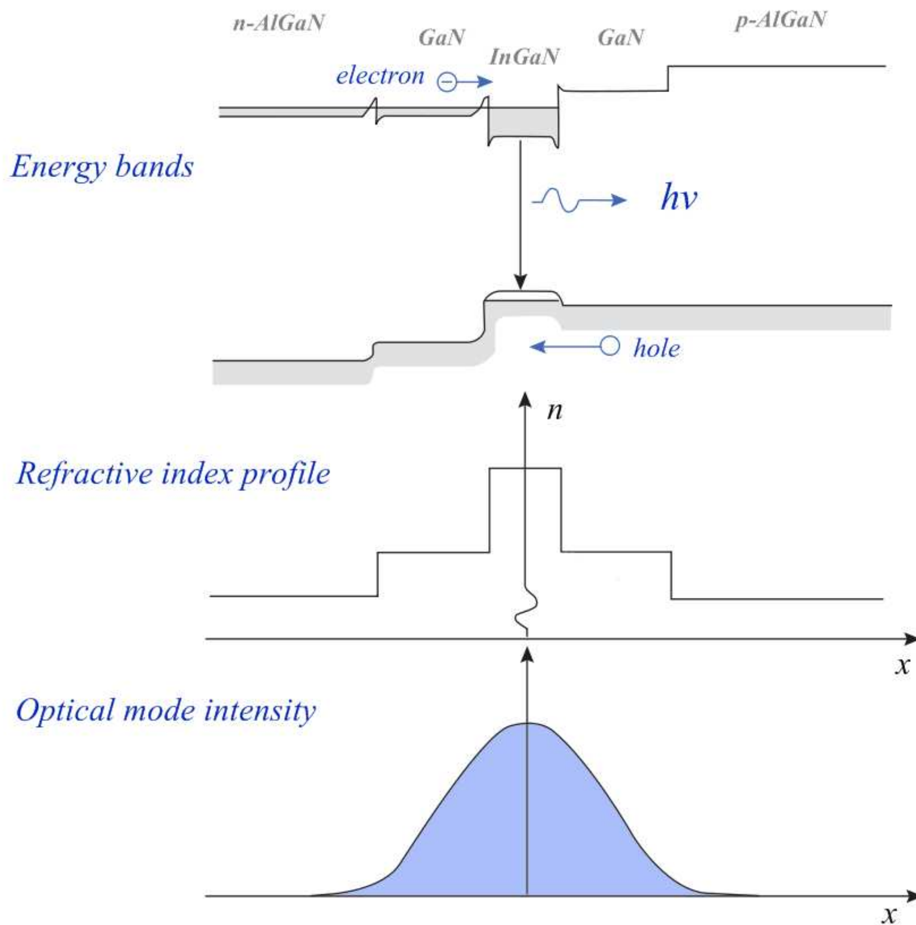

Figure 3.3: From the top: transverse profiles of the bandgap, refractive index and the optical field intensity in a separate confinement heterostructure.

Because the cavity volume occupied by the photons V_p is larger than the active region volume occupied by electrons V, we need to account for this electron-photon overlap factor, V/V_p, which is generally referred to as the *confinement factor* Γ [18] and is a basic parameter in SCH structure description.
Finally, beyond the unqestionable advantages of the design, there are also problems associated with heterojunctions. One of the critical difficulty manifests in the resistance introduced by the heterointerfaces. As schematically shown in Fig. 3.3a, the abrupt interfaces between materials of different composition induce transfer of carriers from the larger-bandgap alloy to the smaller-bandgap material resulting in bending of the bands and formation of a small potential barrier. Under forward bias, carriers transferring from one semiconductor to the other must overcome this barrier by either tunneling or by thermal emission over the barrier. The resistance caused by heterojunctions can have a strong deleterious effect on device performance, especially in high power devices since thermal power produced by heterostructure resistances leads to heating of the active region, thereby decreasing the radiative efficiency [34].

3.2.2 Active region – quantum wells

A blueprint for the emission wavelength of a semiconductor laser requires choosing the appropriate composition of the active region alloy that forms quantum wells. Ternary and quaternary compounds of the AlInGaN material system allow for continuous bandgap tuning, from the deep ultraviolet to the far infrared [19]. The choice of the barriers' height, the width of the quantum wells as well as their composition are limited by several important physical and technological effects that need to be taken into account. Of particular importance is the problem of indium segregation and indium phase separation. On the other hand the effects connected with spontaneous and piezoelectric polarization also have a profound influence on laser parameters.

Indium segregation and indium phase separation

Fabrication of semiconducting alloys with a possibility of independent tuning of the bandgap and the lattice parameter is of great importance. An accurate matching of the alloy lattice constant to that of the neighboring material results in less defective structure, and thus better operation quality of the laser. Very often the range of tuning is given by assuming a linear variation in energy gaps

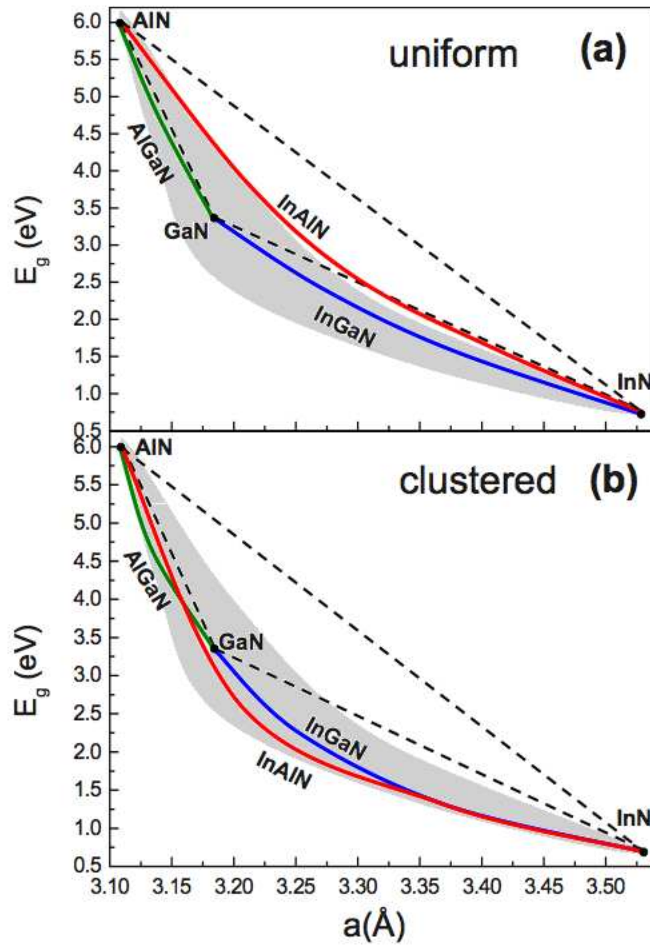

Figure 3.4: Energy gaps of $Ga_xAl_{1-x}N$, $In_xGa_{1-x}N$, and $In_xAl_{1-x}N$ as functions of lattice parameter, (a) for a uniform and (b) clustered distribution of cations. The triangle formed by dashed lines corresponds to a linear approximation of the relation between band gaps and lattice parameters. The shaded area covers the region where the experimental points are lying. *Courtesy of Iza Gorczyca.*

with lattice parameters (e.g. [35]). However, recent theoretical calculations by Gorczyca *et al.* [36] revealed that the assumption, in case of nitride alloys, could be particularly misleading. Fig.3.4 shows results of *ab initio* calculations as well as experimental data displaying large deviations from linearity in case of both uniform and clustered distributions of the admixed cations. The growth of InGaN alloys has proven to be exceedingly challenging, mostly due to the trade-off between the quality of the epilayers and the amount of InN admixture into the alloy as the growth temperature is changed. At the maximum temperature typically used for the epitaxial growth of $In_xGa_{1-x}N$ (800 °C), which usually results

in high crystalline quality, the amount of InN in the solid is limited to low values because of the high volatility of nitrogen over InN [37].
Theoretical calculations revealed that at this temperature the solubility of indium in GaN is less than 6% and that the critical temperature for phase separation is 1250 °C [38], indicating that $In_xGa_{1-x}N$ alloys are unstable over most of the composition range at normal growth temperatures. Attempts to obtain higher indium concentrations showed that by using MOVPE and lowering the growth temperature from 800 to 500 °C an increase of indium concentrations was observed, but at the expense of reduced crystalline quality [37]. Efforts to increase the InN concentration in the solid by raising indium vapor pressure resulted in In droplets on the surface [39]. Phase separation was reported still in the early (1975) experiments, after $In_xGa_{1-x}N$ samples with $x \geq 0.1$ were annealed in argon ambience at various temperatures below 700 °C [40]. Calculations reported by Teles *et al.* [41] confirmed the existence of a broad miscibility gap for growth temperatures around 1000 K for unstrained $In_xGa_{1-x}N$ alloys and that the region of spontaneous decomposition is reduced by strain. In particular, high indium content regions have been observed around screw dislocations [42, 43], which are believed to act as seeds for spiral growth of hillocks, creating favorable conditions for In segregation. Measurements of wavelength-dependent cathodoluminescence (CL) in InGaN quantum wells allowed to correlate those defects with the indium rich regions, where the observed CL intensity was much brighter due to the migration of carries into high indium concentration areas [43], in which the bandgaps are relatively smaller.

This spatial variation in composition inevitably affects optical properties of fabricated samples leading to inhomogeneous broadening of the gain spectra as well as of the electroluminescence spectra, due to potential fluctuations [44, 45]. As a consequence of this inhomogeneous broadening and other adverse effects like defects-associated high indium concentration regions acting as non-radiative recombination sites for carriers, the laser threshold currents were substantially increased, resulting in degradation of laser's performance. Lastly, the material barrier (associated with indium clustering) to provide good quality layers and push the emission toward longer wavelengths had only been solved recently.

For example, studies by Krysko *et al.* [46] revealed that adequate preparation of a substrate can influence the way in which indium incorporates during InGaN growth. By using slightly misoriented substrates, of around 0.2° to 2° miscut

angle in the direction $[11\bar{2}0]$ with respect to the wurzite crystallographic c-plane, it is possible to obtain growth conditions in which a flow of the atomic steps takes place during the epitaxial structure build-up. Such misorientation of the substrate is presumed to control the spacing of growth steps at the growth surface and, in consequence, to influence the diffusion of ad-atoms to these steps, independent of temperature and III/V ratio [46]. In principle, a larger miscut angle should give rise to a reduced spacing of surface steps and thus promote In clustering at step edges, while a smaller miscut should lead to wider spacings and, in turn, possibly to homogeneous formation of two-dimensional nuclei on the terraces between the steps. The possible origin of the differences in In content of terraces' treads and rises can be explained by surface thermodynamics [47].
Finally, a very interesting effect attributed to miscut-induced growth mechanisms on the small steps of terraces has been reported by Suski *et al.* [48]. Experimental studies showed that a relatively small (up to $2\,^{\circ}$) GaN substrate misorientation can also strongly change the hole concentration in Mg-doped GaN layers grown by MOVPE. Typically, due to relatively large activation energy of Mg acceptors ($150 - 200\,meV$) as well as high unintentional donor concentration (inherent with the growth process), hole carrier concentrations are limited to the magnitude not exceeding $5 \cdot 10^{17}\,cm^{-3}$ at $300\,K$. The use of a misoriented substrate lead to an increase in the hole carrier concentration to the level above $10^{18}\,cm^{-3}$ and a decrease in GaN:Mg resistivity below $1\,\Omega cm$. This effect does not originate from higher Mg incorporation, as it was verified by secondary ion mass spectroscopy (SIMS) measurements and also confirmed by a closer analysis of the temperature dependence of electrical transport. Introducing relatively low density of Mg acceptors enables to avoid formation of defects consisting of Mg in non-acceptor states, wheras a decrease in unintentional donor density is responsible for the observed increase in the hole concentration.

Polarization effects

Dissimilar to most of the III-V semiconductor compounds, like GaAs or InP which crystallize in the zinc blende structure, GaN and related alloys are grown usually in the hexagonal wurzite symmetry. Although a zinc blende symmetry GaN can be grown using cubic substrates like Si [49], 3C-SiC [50] or GaAs [51], its character is metastable and leads a significantly lower crystal quality. Unfortunately, there is a disadvantage of the wurzite configuration that originates from the lowered

symmetry in those crystals due to lack of the centre of inversion symmetry of the crystallographic structure along the *c*-axis. In consequence, crystals grown along [0001] direction in hexagonal symmetry are subject to strong built-in electric fields, which in case of nitrides are highly pronounced.

There are two components inducing material polarization in the wurzite symmetry of nitrides. The first originates from the intrinsic asymmetry of the partly ionic bond in the equilibrium crystal structure of lowered symmetry. As a result a bulk net displacement of the negative charge towards nitrogen along [0001] direction occurs, leading to formation of *spontaneous polarization* [52]. This effect is particularly important, when heterointerfaces between two nitride semiconductors with varying electronegativity are involved, which manifests as a polarization charge at the heterointerfaces.

The other component of the internal electric field is a strain-induced *piezoelectric polarization*, which originates partially from the lattice mismatch between the GaN substrate and InGaN-based quantum wells and partially from thermal strain caused by the thermal expansion coefficeint difference between the substrate and the epitaxial layers [53]. As a result of this mismatch, QWs in the active region are subject to compressive biaxial strain induced in a junction plane. In order to preserve the volume of a unit cell, additional distortion along *c*-axis appears leading to piezoelectric polarization. In case of gallium nitride, piezoelectric coefficients are an order of magnitude higher than in many of the traditional group III-V semiconductors [54, 53, 55, 56, 57]. The total amount of internal electric fields can reach up to $1\,MV/cm$ for a typical In content in a quantum well of less than 10%. The effect was originally predicted by means of *ab initio* calculations [54] and confirmed by experimental measurements [58, 59].

Spontaneous and strain-induced piezoelectric polarization can influence the final status of the interfacial free-charge density (sheet carrier density) in heterostructures. For multiple interface heterostructures, the sheet carrier density and barrier thickness, but also the width of quantum wells are all to be taken into account, because the potential drop across the structure is directly proportional to the product of polarization field and the well width.[1] Polarization discontinuity at the interfaces implies a net spatial separation of carriers, resulting in a bound charge appearing on each interface and being a source of a step-like change in the electric field. This electric field causes band bending to the extent of transforming

[1] using a constant field approximation, when free-carrier screening is neglected [20]

otherwise square quantum well potential distribution to a triangular distribution in the constant field approximation [20], which in turn is responsible for a red shift in radiative recombination transition energy. The problem is referred to as a *quantum confined Stark effect* and is additionally a current-dependent phenomenon [60]. Presence of the electric field induces a spatial separation of electron and hole envelope wavefunctions towards triangular potential minima at opposite interfaces of a QW (see Figure 3.5), resulting in a reduction of the oscillator strength and thus the radiative recombination rate along with the optical gain.

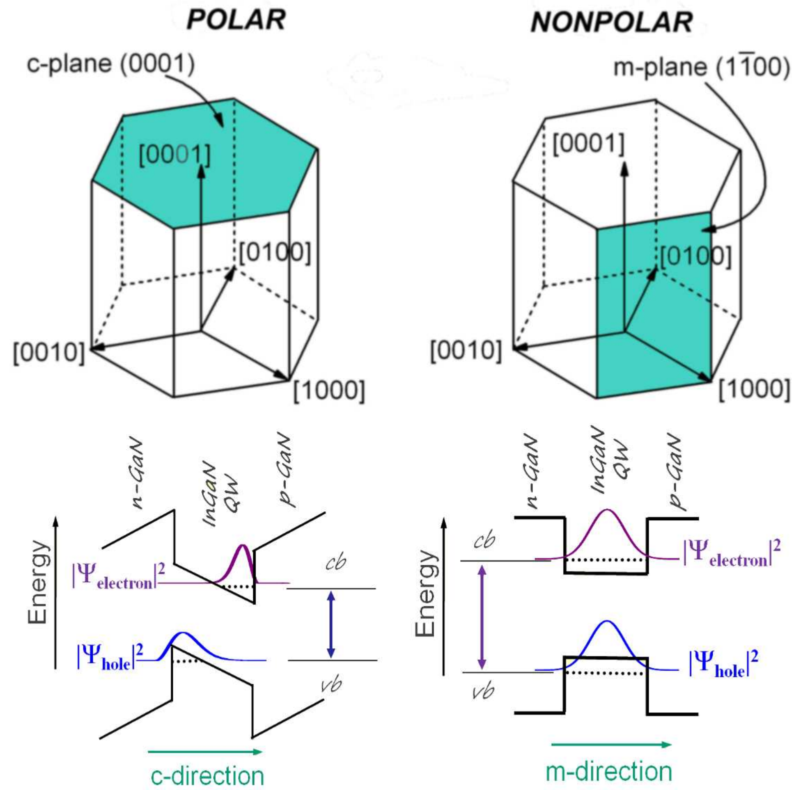

Figure 3.5: Crystal planes exposed to the epitaxial growth oriented in polar (c-plane) and nonpolar (m-plane) directions. Below, corresponding energy band diagrams and the position of electron and hole wavefunctions.

Fortunately, the internal fields in quantum wells can be efficiently screened by high injection levels of carriers [61, 62] and also through heavy barrier doping with Si donors (of densities reaching $10^{19}\,cm^{-3}$) [62], reestablishing efficient electron - hole recombination. The effect of polarization can be straightforwardly observed by means of time-resolved photoluminescence measurements [63].
The problem of internal electric field takes stronger effect in case of laser struc-

tures with thick InGaN quantum wells as well as for QWs with higher indium contents, usually designed for operation in a blue-green spectral range [64]. The thickness, however is usually kept within an effective Bohr radius a^*_{Bohr}, which remains in the range of a few nanometers, opposing a decrease in spatial overlapping of the wavefunctions.

Number of quantum wells

The number of quantum wells used in a laser design is correlated with the total of optical losses within the resonator. Transparency condition needed to reach lasing requires gain high enough to overcome losses, which can be expressed by the following formula:

$$\Gamma \mathrm{g_{th}} = \alpha_\mathrm{i} + \alpha_\mathrm{m} \tag{3.1}$$

where $\Gamma \mathrm{g_{th}}$ is the modal gain at threshold, Γ is the confinement factor and α_i and α_m are the internal and mirror losses, respectively. From this condition, when the number of quantum wells (and thus Γ) is increased, compensation of losses becomes possible at lower pumping levels in the wells. This happens, however, at the expense of higher currents flowing through the structure and in consequence to generation of heat. An increase in technological maturity, resulting in the improvement of laser homogeneity (reduction of absorption) and interface smoothness (reduction of scattering) would, for a given mirror design (fixed α_m), lead to a small optimum number of quantum wells, for which a minimal threshold is obtained. The first InGaN quantum laser construction reported by Nakamura *et al.* [13] utilized 26 periods of 25 Å-thick $In_{0.2}Ga_{0.8}N$ quantum well layers separated by 50 Åthick $In_{0.05}Ga_{0.95}N$ barrier layers. The structures that followed incorporated MQWs with as little as 7 periods [14], and eventually got reduced to 3 periods being, parallel to a single quantum well, the most frequently employed laser design.

Finally, the last issue to be pointed out concerns historically a technological problem of closing the active region with a thin buffer layer on top of the InGaN layers that would prevent their dissociation during the growth of the subsequent wider bandgap layers, which required much higher substrate temperatures. Later it turned out that the presence of such buffer layer can greatly improve the overall performance of devices, acting as a blocking layer for electrons to prevent their escape from the active region. More detailed description of the *electron blocking layer* (EBL) will be given in the following section.

3.2.3 Electron Blocking Layer

As it was already stated, the presence of EBL has a profound influence on laser parameters, of which internal quantum efficiency is the most apparent. There are several key issues to be resolved in order to achieve high efficiency devices and these include carrier leakage from the active region. Due to the difference in electron and hole masses in nitride semiconductors, electrons tend to escape from the active region and holes are injected to the active region rather poorly. For comparison, the effective mass of a conduction band electron is estimated to be $0.2\,m_0$, while the effective mass of a heavy hole valence subband carrier to $1.5\,m_0$ [65]. In contrast to high electron mobility that can reach at room temperature $2 \cdot 10^3\,cm^2\,V^{-1}s^{-1}$ and that induces a strong tendency for the electron overflow into the p-type layers, hole mobility in III-nitride based epitaxial layers is strongly impeded by heavy doping with Mg acceptors ($\sim 10^{20}\,cm^{-3}$). Such heavy doping is necessary to obtain free hole concentrations leveled with the electronic ones, which are on the order of $10^{18}\,cm^{-3}$. The problem originates from the deep nature of Mg acceptor and its large activation energy in GaN ranging between $150\,meV$ and $250\,meV$ [66], in contrast to Si donor activation energy, which is only around $20\,meV$ [67]. In consequence, excess scattering mechanisms reduce the room temperature hole mobility to the value of $2\,cm^2\,V^{-1}s^{-1}$ [65]. Such a discrepancy leads to a drift of electron-hole recombination from the active region into the p-type layer, reducing the QW emission, which significantly affects the optical efficiency of a LD and its temperature stability. Therefore, inclusion of a thin (typically of around $20\,nm$) but of rather high composition AlGaN electron blocking layer (usually of $\sim$ 20% Al) is essential to overcome this problem. Unfortunately EBL acts as a potential barrier not only for electrons to stop their leakage, but also for holes, diminishing their injection from the p-side into the active region. A thicker EBL may prevent electrons from tunneling through the barrier to the p-side, but at the expense of hindered hole injection, thus a careful balance of EBL thickness and its composition is required.

3.2.4 Ridge geometry

Stable fundamental mode operation, preferably up to high optical output powers is of chief importance in case of blue laser diodes. Particularly if we have in mind applications like data storage or printing, where a tight and reproducible focus

is essential. To facilitate focusing, the beam divergence in both perpendicular directions ($\Theta_\perp$ and $\Theta_\parallel$) should be similar, which means that a low aspect ratio is required. One way of engineering this is to decrease the lateral (i.e. in plane of epitaxial layers) dimension of the waveguide. In consequence, an increased lateral divergence is obtained. At the same time the optical confinement factor Γ is increased, which effects the threshold current to drop. First reports in nitrides from Nakamura *et al.* [68] on implementing the ridge geometry (also known as *mesa structure*) compared the stripe- and ridge- LDs that were fabricated with the only difference of the mesa etched down the p-type cladding in case of the latter laser. The measured characteristics demonstrated an improved performance of the ridge LD, namely twice smaller threshold current density and much higher differential quantum efficiency. The result is due to the limited lateral current spreading and much better lateral confinement of the optical field. Further research showed that both the height and the width of the ridge forming the laser diode waveguide determine threshold current density and have a profound influence on lateral stability of the mode and the far-field distribution [69, 70].
Several studies of transverse far-field distributions discuss the optimization of the vertical layer structure to maximize the confinement factor Γ at the lowest possible far-field angle [71, 72, 73, 74, 75]. One delimiting aspect is the problem of the mode leakage into parasitic modes of the contact or buffer layers, or even of the substrate if the vertical waveguide layer is not thick enough and the binding of the mode becomes too weak. The issue of the substrate modes and the problem of their suppression will be further discussed in Chapter 4, where details of the new idea of plasmonic cladding will be presented.

3.3 Mirrors

The optical cavity mirrors can be formed by cleaving or by etching facets. In either case dielectric coatings are deposited on the surfaces to obtain desired reflectivities. Owing to their large bandgaps, GaN-based structures are characterized by relatively low refractive indices of typical value of 2.5, which implies that the uncoated semiconductor – air interface has a theoretical reflectivity of around 18% for an ideally smooth facet. In most semiconductor systems the preferred method for facet formation is cleaving[2], because it allows to obtain smooth,

[2] *Cleavage*, by definition, is the ability of a crystal to break along definite crystallographic directions, while *parting* is the splitting of a crystal along a plane that does not normally cleave,

vertical planes. This method, however, can be relatively easy applied to structures grown practically only on bulk gallium nitride in c-direction, because for non-polar directions there are no *easy cleavage* planes. For other substrates like sapphire, which does not cleave readily due to many cleavage planes that have approximately equal cleave strength and are within a small angular distance, parting in many directions is observed instead of smooth vertically cleaved faces. Despite these obstacles there were attempts of such fabrication of devices, for example Stocker *et al.* [76] reported on fabrication of InGaN/GaN lasers grown on c-plane sapphire with cleaved facets of roughness of 16 nm, which corresponds to a reflectivity of only 4%.

On the other hand, etching methods of facet fabrication usually require special efforts to develop recipes for producing high quality surfaces. Among typically used techniques are methods of dry etching like *Reactive Ion Etching* (RIE) or *Chemically Assisted Ion Beam Etching* (CAIBE) [77, 78], which allow to obtain vertical planes within 1° - 2°, but the process requires precise masking of each facet. Using the latter technique, Kneissl *et al.* [78] fabricated facets with roughness of around 5 nm, which is comparable to results of cleaved facets on free-standing GaN obtained by Nakamura *et al.* [79]. Also the use of mechanical polishing and *Focused Ion Beam* (FIB) polishing were reported [80]. Although it is possible to attain smooth and close to vertical facets, these methods are labor intensive and cannot be easily scaled to mass production. A comparison of obtained facet roughness using different methods of fabrication and corresponding reflectivities determined using model proposed by Stocker *et al.* [76] are summerized in Table 3.2.

Fabrication of facet coatings to reach desired mirror reflectivity is usually performed using e-beam evaporation technique to deposit a stack of alternating quarterwavelength layers with high and low values of refractive indices. The appropriate design of facet coatings allows to reduce threshold currents in laser structures and also prevents from oxidation of the surface. The impact on threshold current can be seen from Eq. 3.1 describing lasing threshold condition, where α_m can be expressed as:

$$\alpha_m = \frac{1}{L} ln\, R_1\, R_2, \tag{3.2}$$

L is the Fabry-Perot cavity length and R_1 and R_2 are mirror reflectivities.

---

and can be caused by stress, defects, or other perturbations of the crystal structure.

Table 3.2: Comparison of facet fabrication methods for structures grown on different substrates.

Group	Fabrication method	Roughness Δ d [nm]	Maximum Reflectivity $R/R_0{}^*$	Ref.
Unipress/TopGaN	cleavage: *bulk GaN*	< 1	1	[81]
APA Optics	cleavage: *spinel substrate*	< 1	1	[82]
UCSB	etching: RIE, $Cl_2 - based$ then FIB polished	< 1	1	[80]
Xerox	etching: *CAIBE*	5	0.8	[78]
Nichia	cleavage: *free-standing GaN*	5	0.8	[79]
UCSB	cleavage: *c-sapphire*	16	0.22	[76]

* R_0 is the theoretical reflectivity from a perfectly smooth facet, as given by the Fresnel equations. For group-III nitride laser facets $R_0 \approx 18\%$.

Chapter 4

Laser devices

In this chapter I describe the structure and general properties of laser diodes under investigation (sections 4.1 and 4.2). In section 4.3 results of basic characteristics of LDs, which I measured during my research, are presented. Next, I describe more advanced characterization of the studied LDs addressing issues like optical gain spectra obtained by means of Hakki-Paoli measurements and optical properties of the laser waveguide. The latter I examined by measuring the near-field patterns of our samples. The obtained results allowed to identify the problem of transversal mode leakage for these structures. Section 4.4. discusses the design of conventional approach of transversal mode confinement. Next I introduce the new method proposed to provide sufficient mode confinement in nitride laser diodes – plasmonic cladding. Its application in the waveguide structure resulted in improved electrical and optical characteristics of the new generation of LDs. Finally, I describe a simple model that was employed to simulate the optical mode distribution in the laser structure under study. The simulations confirmed the experimental results obtained for old and new structure designs.

Laser structures, which are the subject of the study presented in this dissertation, were entirely fabricated at the Institute of High Pressure Physics Polish Academy of Sciences and its *spin-off* company TopGaN, which hold the requisite facility and know-how of manufacturing high-tech devices.
A large part of optical characterization was performed during my two visits to Regensburg University (Germany) at the laboratory of prof. Ulrich Schwarz, where I could use the existing setups for optical gain, near-field and far-field measurements.

4.1 LD structures under investigation

LD structures were deposited epitaxially on bulk gallium nitride crystals supplied by the Crystallization Laboratory of the Institute of High Pressure Physics. These substrates were grown either by HPHT (high-pressure high-temperature) method or by HVPE (hydride vapor phase epitaxy), both growth techniques provide good quality substrates with low threading dislocation densities. Also substrates grown by ammonothermal method and provided by Ammono Ltd. were used. Prior to epitaxial deposition, surface preparation of the substrate crystal is required. This preparation includes primarily mechanical polishing, which results in uniform thickness of the substrate and allows to introduce the desired misorientation for optimum growth conditions. Because Ga- and N- terminated sides of a bulk GaN crystal show different chemical properties, apposite surface treatment need to be developed separately. While N-terminated side of a GaN crystal is chemically active, chemical etching in 1:5 water solution of KOH allows to obtain a perfectly flat surface without defects introduced by mechanical polishing. Ga-terminated facet, on the other hand, remains chemically inert and demands procedures of mechanochemical polishing.
Metal-organic chemical vapor deposition (MOCVD) of epitaxial layers constituting laser structure employed a vertical-flow reactor with SiC-coated graphite susceptor heated by an inductive coil, which defined the growth temperature through the current flow. Purified to *ppb* level molecular nitrogen (N_2), hydrogen (H_2) and ammonia (NH_3) are used for chemical reaction with metalorganic compounds: trimethyl gallium (TMG), trimethyl aluminum (TMA) and trimetyl indium (TMI), being the sources of group-III metals. The source of Mg for p-type doping is Cp2Mg, for n-type doping SiH_4 as a source of Si. Typically, the growth temperature of GaN layers is 1050 °C, 800 °C in case of InGaN and 1090 °C in case of AlGaN. Deposition rates are monitired by a laser reflectometry with a resolution of a few angstroms, which is essential for precise control of the width of grown quantum wells.

4.2 Typical laser structure

Typically, laser structure is grown on top of the gallium side of the GaN crystal and begins with 600 nm silicon doped $Al_{0.08}Ga_{0.92}N$ bottom cladding followed by a 50 nm silicon doped lower GaN waveguide and 50 nm $In_{0.02}Ga_{0.98}N$ injection

layer. The active region consists of three $In_xGa_{1-x}N$ quantum wells with indium content varying from 0.02 to 0.15 to choose the desired emission wavelength within the range of 380 to 430 nm. The thickness of QW is usually 3.5 nm, which ensures effective carrier capture and confinement. Quantum barriers of typical thickness of 8 nm are formed by Si-doped $In_{0.02}Ga_{0.98}N$ layers. The multi-quantum well (MQW) active region is followed by a 20 nm $Al_{0.2}Ga_{0.8}N$:Mg electron blocking layer (EBL). The upper waveguide and upper cladding layers are formed by 80 nm GaN and 330 nm $Al_{0.08}Ga_{0.92}N$:Mg, respectively. Epitaxial structure ends with a 30 nm-thick GaN layer, heavily doped with Mg, which serves as a subcontact layer. Fig.4.1 shows a schematic layer design of the epitaxial structure and a TEM image of a grown sample.

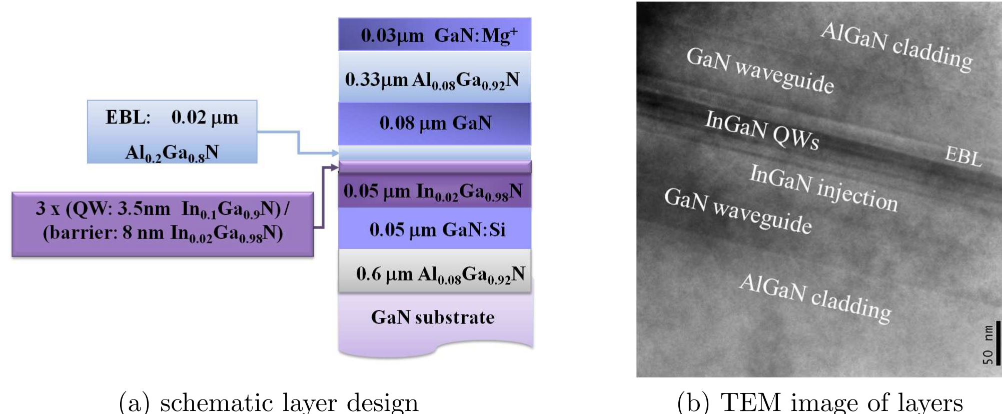

(a) schematic layer design

(b) TEM image of layers

Figure 4.1: LD structure: (a) schematic epitaxial design, (b) TEM image of MOCVD grown layers.

A typical LD is processed as a ridge-waveguide, oxide isolated device with mesa structure formed by *Inductively Coupled Plasma Reactive Ion Etching* (ICP RIE) of a standard height of 300 nm (i.e. etched down to the upper cladding layer). The stripe width for various devices varies from 3 up to 20 μm. Subsequently, the current flow region is defined by surface isolation with 200 nm of Si_3N_4, which is deposited using *Plasma-Enhanced Chemical Vapor Deposition* (PECVD). Then, by means of a lift-off procedure an opening through the isolating layer is formed to deposit p-side metallic contacts of 25/75 nm Ni/Au layers using e-beam evaporation. Typical low-current resistance of the contact is on the order of $10^{-4}\,\Omega\,cm^2$. Contacts to the highly-conductive n-type GaN substrate consist of Ti/Au/Ni/Au

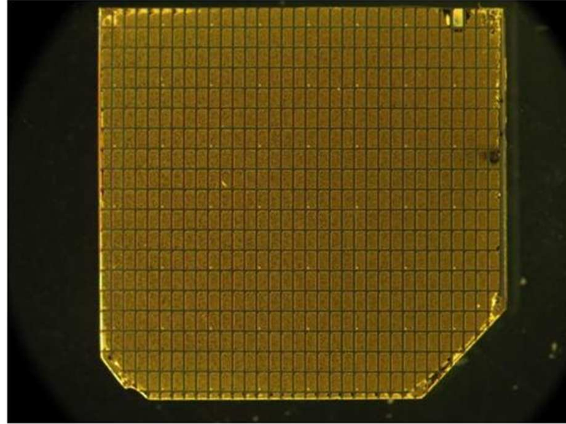

Figure 4.2: A photo of a $1\,\mathrm{cm}^2$ wafer with processed devices

stack (30/70/10/50 nm thick, respectively). The stripe length can be set between 500 to 1000 μm with most typical value of 700 μm. To balance mirror losses and light extraction from the device, dielectric coatings are applied on laser facets. The coatings are deposited by e-beam evaporation and consist of quarter-wavelength stacks of ZrO_2/SiO_2 layers providing 95% and 20% reflectivity for the back and front mirrors, respectively. In Fig 4.2 is a photo of a wafer with processed devices.

4.3 Characterization of LDs

Selective etching studies on fabricated devices reveal that the initial value of threading dislocation densities imposed by the substrate quality increases from the initial number of $10^2\,cm^{-2}$ (in case of the best substrates) to the level of $5 \cdot 10^4 - 1 \cdot 10^5\,cm^{-2}$ [83]. Formation of dislocations is a result of the lattice mismatch and a subsequent strain release between GaN and its ternary compounds (In,Al)GaN [84]. Although the thickness of the epitaxial layers and the lattice mismatch are preserved within the amount of strain away from its critical value at which the cracking of layers occurs, the strain is still large enough to increase the density of dislocations [84]. The majority of threading dislocations originates from the highly lattice mismatched $Al_{0.2}Ga_{0.8}N$ EBL and propagate through the p-type layers towards the surface. However, very small dimensions of the ridge secure relatively low number of dislocations throughout the active region, leaving QWs almost unaffected.

4.3.1 Basic operation parameters

The relation between output power P_{out} versus driving current I, which is referred to as $L-I$ characteristics, above threshold I_{th} is described by an expression taking into account carrier injection and radiative efficiencies (through internal quantum efficiency η_i), internal and mirror losses (α_i and α_m, respectively) and emission energy ($h\nu$) and can be derived from the carrier- and photon-rate equations in a laser medium [18]:

$$P_{out} = \eta_i(\frac{\alpha_m}{< \alpha_i > + \alpha_m})\frac{h\nu}{q}(I - I_{th}) \tag{4.1}$$

A typical light-current ($L - I$) and voltage-current ($I - V$) characteristics along with the emission spectrum of a cw operated laser diode are shown in Fig. 4.3. Above lasing threshold, P_{out} is a linear function of current – in an ideal situation, when all carriers recombine in quantum wells and there are no internal losses, $L-I$ slope would reach around $3\,W/A$ for an energy corresponding to the emission wavelength of a GaN-based LD of around $400\,nm$. In real devices, this linearity is usually disturbed when spatial inhomogeneities in carrier and temperature distribution induce changes if the effective index of refraction in the active region. This triggers off switching between the laser cavity modes and is observed as kinks appearing in the $L - I$ curve. With much further increase of the driving current the excess heat generated by its flow usually cannot be efficiently dissipated by the mounting and cooling system. This leads to *thermal roll-over*, which can be identified in the characteristics as a large bending of the curve, making $L-I$ signal almost flat and means that at such operation conditions the potential barriers in the active region do not efficiently confine carriers. High thermal energy allows them to escape from quantum wells and further contribute to the increased non-radiative recombination.

An ideal voltage-current characteristic for a GaN-based laser would show the threshold value V_{th} slightly above $3.5\,V$. However, in a real device the major overall voltage drop is higher and originates from a high resistance of a p-type contact electrode, which needs further optimizing. The best reported values of threshold voltages remain close to $3.8\,V$ (Samsung).

The emission spectra shows multimode character, typically the full width at half maximum (FWHM) is between 0.5 to $1.5\,nm$ and depends on the stripe size.

The input electrical power at threshold is typically about 15 - 35 kW/cm^2. Taking into account that only a small fraction of applied energy is converted into light

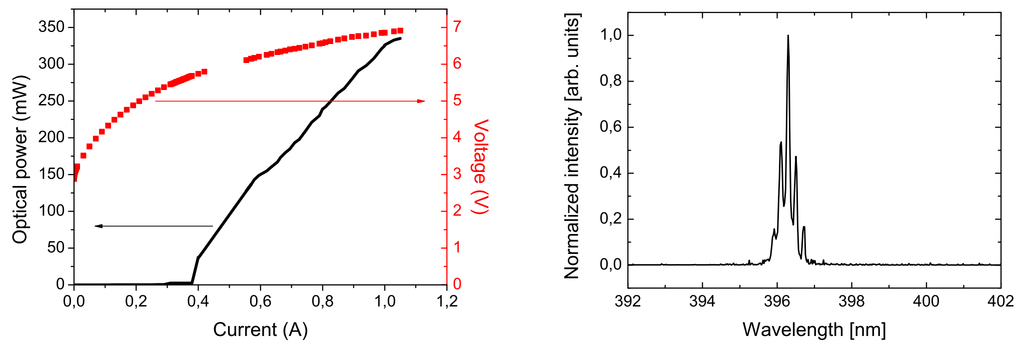

(a) $L - I$ and $I - V$ characteristics (b) Emission spectra

Figure 4.3: (a) Light-current and voltage-current characteristics of a typical LD with ridge dimensions of $700\,\mu m$ x $10\,\mu m$, (b) emission spectra showing multi-mode operation, specific for broad-ridge devices.

emanating from the laser, the amount of heat to be dissipated by the device's mounting system is of considerable volume. For better thermal management chips are mounted on a diamond heat spreaders and a standard laser housing, which uses a ϕ $5.6\,mm$ TO can with proper air-tight sealing. Fig. 4.4 shows a standard $5.6\,mm$ TO can housing and a SEM image of a mounted laser chip.

(a) standard TO-can housing

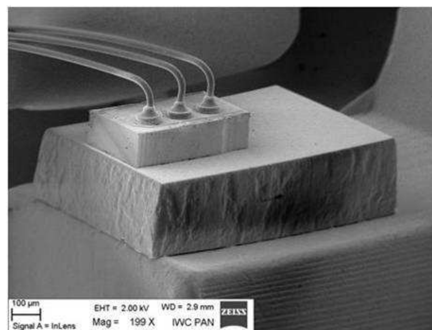

(b) LD chip mounting

Figure 4.4: Packaging and mounting of a laser diode: (a) standard TO-can, (b) SEM image of a chip with bonds providing electrical connection, mounted on a diamond heat spreader.

4.3.2 Optical gain

The performance of a laser depends on the optical losses in the structure, but equally important is the ability of the system to amplify light in the active region, which is determined by the gain as the lasing condition requires the mode gain to reach the total optical loss at the threshold. The gain is supplied by the material gain of the InGaN quantum wells.

Using *Fermi's Golden Rule,* the material gain G_{12} at given transition energy E_{21} is composed of two factors, one of them is material-related, the other depends on carrier population [18]:

$$\begin{aligned} G_{21} &= g_m(E_{21}) \ (f_2 - f_1) \\ &= \frac{2\pi}{\hbar} \frac{\mid H'_{21} \mid^2}{v_g N_p} \rho_r(E_{21}) \ (f_2 - f_1) \end{aligned} \tag{4.2}$$

The material property $g_m(E_{21})$ is given by:

- the matrix element: $\mid H'_{21} \mid^2$,
- the density of available state pairs corresponding to the transition energy E_{21}: $\rho_r(E_{21})$,
- the photon population in a considered optical mode: N_p,
- and the group velocity of the electromagnetic wave: v_g.

The difference $(f_2 - f_1)$ is the *Fermi factor* dependent on the injection level, f_2 and f_1 are the quasi-Fermi levels in the conduction and valence bands, respectively.

The material-dependent component defines the maximum material gain possible under entire population inversion ($f_2 = 1, f_1 = 0$). For nitride materials, the maximum material gain value is about $10^4\, cm^{-1}$ and usually only about 30% of the maximum material gain is suffucient to obtain lasing. Selection rules determined by the symmetry and the overlap between wavefunction envelopes allow only for transitions between state pairs of the same subband number (level) in quantum wells. Only those pairs yield a dominant contribution to the total gain spectrum, of highest importance are states occupying the first level.

A common approach to gain measurements is the *Hakki-Paoli* method based on the analysis of a longitudinal mode modulation depth [85, 86] and therefore requires a high resolution spectrometer. In this approach modal gain can be

retrieved from electroluminescence spectra provided that a single longitudinal mode of the laser cavity is excited, thus spectra are registered below threshold. The spacing $\Delta\lambda$ of the longitudinal modes is given by:

$$\Delta\lambda = -\frac{\lambda^2}{2Ln}\left(1 - \frac{\lambda}{n}\frac{dn}{d\lambda}\right)^{-1}, \quad (4.3)$$

where n is the effective refractive index of the waveguide and L is the cavity length. The term in brackets is a dispersion related correction. For resonator length $L = 700\,\mu m$ and wavelength of maximum gain $\lambda_{max} = 410\,nm$ the longitudinal mode spacing $\Delta\lambda$ is around $0.043\,nm$ at λ_{max}.

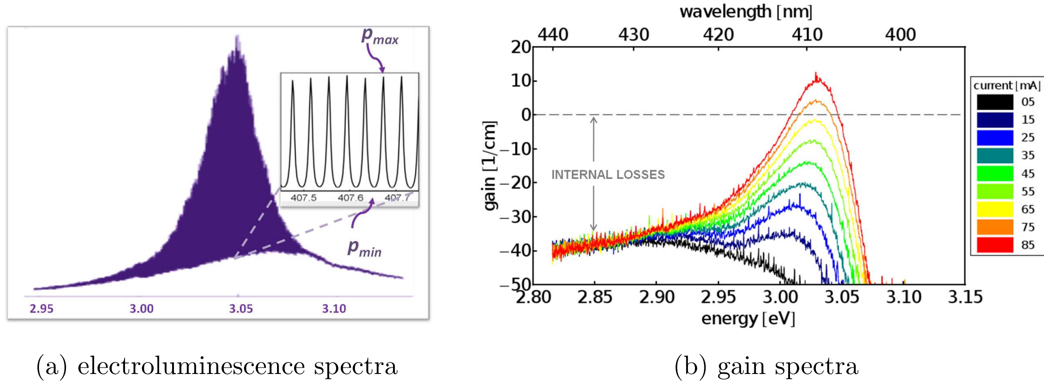

(a) electroluminescence spectra

(b) gain spectra

Figure 4.5: Hakki-Paoli gain measurements: (a) high resolution electroluminescence spectra at $I = 0.8I_{th}$, (b) Gain spectra at different currents for sample LD4760d65 with $3\,\mu m$ ridge. Relatively large optical losses indicate that further optimization of the structure is needed.

Modal gain g is given by modulation depth of the Fabry-Perot modes of the laser resonant cavity [87] (see Fig. 4.5a):

$$\begin{aligned} g &= \Gamma G - \alpha_i \\ &= \frac{1}{L} ln\left(\frac{\sqrt{p_{max}/p_{min}}+1}{\sqrt{p_{max}/p_{min}}-1}\right) + \frac{1}{2L} ln(R_1 R_2), \end{aligned} \quad (4.4)$$

where G is the material gain, α_i stands for internal losses, Γ is the confinement factor, L - the cavity length and $R_{1,2}$ are the mirror reflectivities. The measurement setup utilized a double monochromator of $85\,cm$ focal length with

1800 $lines/mm$ in second scattering order, which allowed to obtain dispersion of 0.1 nm/mm in the exit plane of the monochromator. Light was detected by an optical multichannel detector. The setup's spectral resolution was limited by optical aberration of the monochromator to $5 \cdot 10^{-3}\, nm$.
An example of highly-resolved electroluminescence spectra and gathered optical gain spectra retrieved for different currents are presented in Fig. 4.5. The measurements were performed for sample LD4760d65 with a cavity length of $L = 700\, \mu m$, and $3\, \mu m$ wide ridge. Mirror reflectivities were 95% and 20% for the back and the front facet, respectively thus yielding theoretical mirror losses of about $12\, cm^{-1}$. Total losses obtained from the gain spectra are around $40\, cm^{-1}$, which is a rather high value and implies that further structure optimization is necessary.

4.3.3 Optical properties

As briefly mentioned in chapter 3, an *in-plane* laser diode is a three dimensional optical resonator. The resonant mode, originating from radiative recombination within InGaN quantum wells, is guided by a GaN-based waveguide and an $Al_{0.08}Ga_{0.92}N$ claddings, which account for transversal (across the epitaxial structure) optical mode confinement. Lateral confinement (in plane of epitaxial layers) is realized by a mesa structure with walls covered with an insulating layer of Si_3N_4 limiting injection of carriers only to a thin stripe region, thereby reducing current spreading. This stripe defines the axis and the width of a laser cavity, its length is determined by dimensions of the chip. Due to the limited charge flow, so called *gain guiding* takes place and despite its diverging wavefront properties [88], a spatial variation in a distribution of injected carriers induces a constant mode profile in the lateral direction. The lateral mode guiding effect is additionally supported by a weak *index guiding* originating from the difference in refractive indices between GaN waveguide, an insulating Si_3N_4 layer and the air or metal interface. Beyond the borders between electrically excited and unexcited regions, increased losses keep a semiconductor material below the optical transparency level. Spatially varying distribution of injected carriers determines a gain stripe beneath the p-type contact electrode, along which a guided mode can be sustained.

The optical mode distribution in a waveguide is described analyzing time- and space-dependent wave equations according to Maxwell's theory:

$$\nabla^2 E = \mu\epsilon \frac{\partial^2 E}{\partial^2 t} \tag{4.5}$$

For a semiconductor laser, this relation can be satisfied by time-harmonic field propagating in a dielectric waveguide oriented along the z-axis:

$$E(x, y, z, t,) = \mathbf{\hat{e}_i} E_0 U(x, y) e^{i(\omega t - \tilde{\beta} z)} \tag{4.6}$$

The unit vector $\mathbf{\hat{e}_i}$ defines either TE or TM polarization, E_0 is the wave amplitude (in volts) and U(x,y) stands for the scalar normalized electric field profile in the plane perpendicular to the propagation axis. Optical gain and internal propagation losses are described by the complex propagation constant $\tilde{\beta}$.
Putting expression (4.6) into (4.5) yields to a time-independent relation, which must be satisfied by the dielectric field distribution $U(x, y)$:

$$\nabla^2 U(x, y) + [\, n^2 {k_0}^2 - \tilde{\beta}^2 \,] U(x, y) = 0, \tag{4.7}$$

where k_0 and n stand for the free-space wave vector and the effective refractive index of a given mode, respectively. All laser cavity modes are unique solutions to Maxwell's equations, which fulfill the continuity conditions of tangential field components at the boundaries. $U(x, y)$ corresponds to the distribution of intensity profile of a standing electromagnetic wave in a laser cavity. In practice, the transversal field profile of a guided mode has a maximum at the active region and takes the form of evanescent waves.
At the output facet the optical wave emerges from the laser resonator and diffracts freely into surrounding air. Diffraction theory refers to the field emitted from the laser waveguide as the *near-field*. Near field waves are approximately planar, but upon diffraction gradually evolve into spherical waves. After traveling a distance larger than $\frac{w^2}{\lambda}$, where w is the spatial dimension of a source emitting radiation at a given wavelength λ, the diffracted field of spherical shape with a radius of curvature measured from the center of the emitted mode is referred to as *far field* [18]. A complimentary definition is based on the criterion of Rayghleigh

range, z_R, derived from the theory of Gaussian beams propagation:

$$z_R = \frac{\pi w_0^2}{\lambda}, \tag{4.8}$$

where w_0 is the beam waist and λ is the emission wavelength. The far-fied is observed for distances larger than z_R from the source.
According to an approach introduced by Huygen, each area element at the emitting facet is a source of a spherical wavelet, which propagates into the air and contributes to the overall diffraction pattern. The field is a superposition of cyclic functions of different periods and orientations and can be expanded into propagating and evanescent waves [89]. The number of evanescent waves depends on the amount of details in the field distribution $U(x, y)$, which are smaller than the wavelength of emitted radiation. For any evanescent wave, the *on-axis* component is imaginary, which means it propagates mostly in the x-y plane and is not observed in the far-field pattern. The smaller the detail, the greater weight of the evanescent distribution in the *on-axis* direction. In consequence, the very fine features of the field distributions on the laser facet are undistinguished from the distance greater than a few nanometers. They provide, however, a critically important information on waveguiding properties by showing the shape of a guided mode and its evolution in time. Fig.4.6 depicts an image of a laser near field, overlayed on a schematic LD structure and an illustration of the far field pattern origin. Details of the experimental setup for near field and far field measurements will be given in the following section.

Knowing the spatial field distribution $U(x, y)$, the angular far field intensity profile can be deduced using the following expression [18] (see Fig.4.6 for reference):

$$U_F(\theta_r) = \int\int U(x,y)\frac{e^{-ikr}}{r}[\,\frac{i}{\lambda}cos\theta_r\,]\;dxdy \tag{4.9}$$

Because waveguide dimensions for in-plane edge-emitting lasers differ significantly - transversal size is much smaller than lateral, defined by the mesa stripe - the angular spread of the far field is considerably asymmetric, reaching 9° in lateral and 25° in transversal direction off the resonator axis. Despite elliptical intensity distribution, as indicated by Eq. 4.9, the emitted laser beam preserves the spherical symmetry, while it propagates in space. A detailed analysis of waveguiding properties of the laser structure supported by the near field measurements and

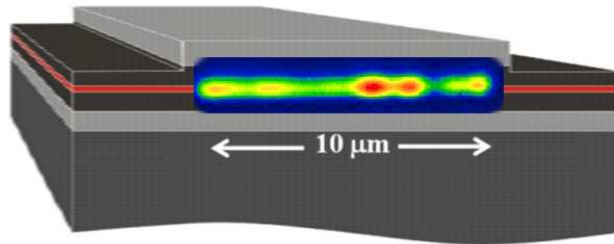

(a) Near field pattern

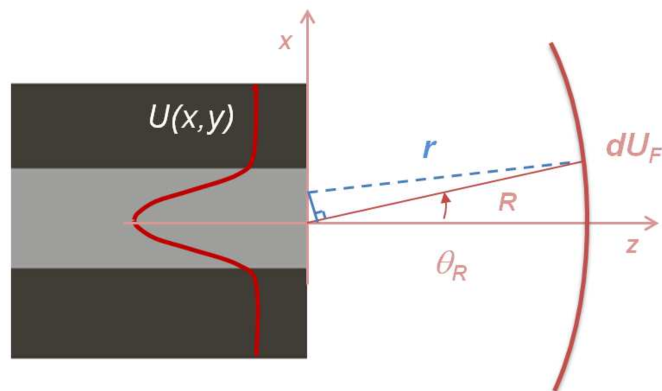

(b) Illustration of a near-field pattern $U(x, y)$, and far-field element, dU_F, a distance R from the facet at the waveguide axis in the $x - z$ plane.

Figure 4.6: (a) Near field image overlayed on a scheme of a laser structure and (b) an illustration of formation of the far-field.

near- to far-field evolution constitute a powerful tool capable of examining the efficiency of a given laser design, as will be shown in the next sections.

4.3.4 Gaussian telescope for near-field to far-field measurements

To measure the near-field of our LDlaser diode samples an imaging setup in a configuration known as *Gaussian telescope* was utilized [90]. The measurements were performed in the laboratory of prof. Ulrich Schwarz, at the University of Regensburg, Germany.

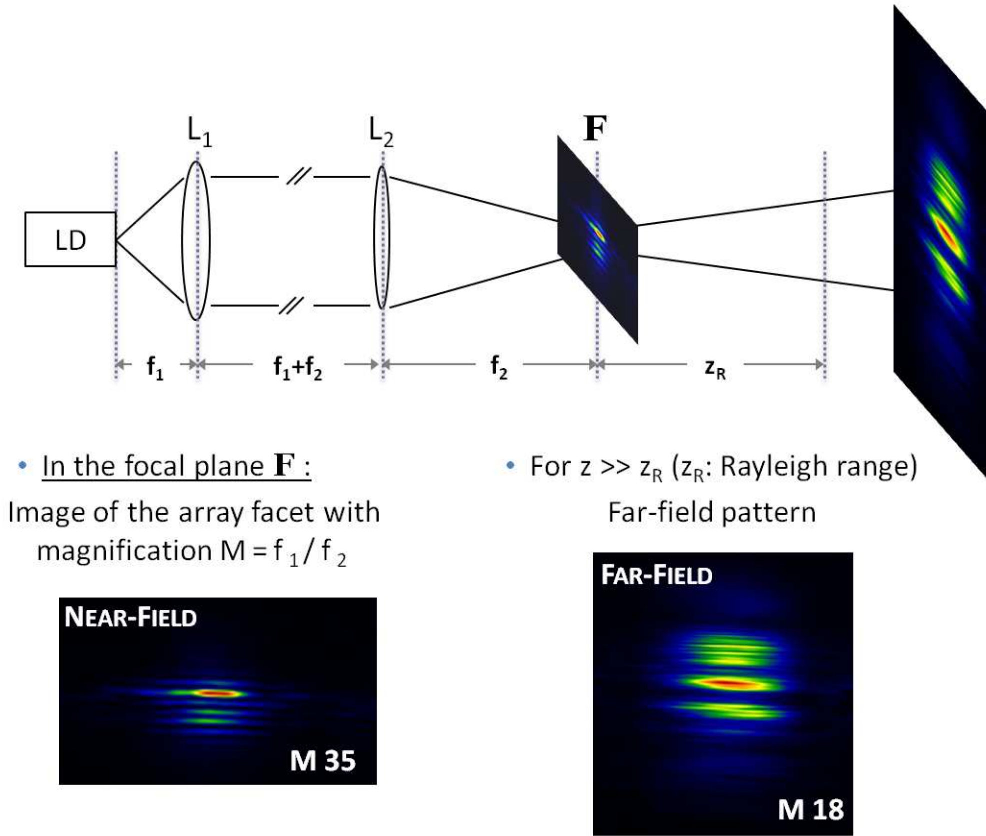

Figure 4.7: A scheme of a measurement setup utilizing a *Gaussian telescope*. The registered images show field distributions for samples LD4551, revealing weak transversal confinement of the optical mode. The near-field image was measured with magnification of 35, for far-field magnification 18 was used. The ridge width of LD4551 samples was 7 μm. The device was pulsed operated with pulse duration of $50\,ns$ and $10\,kHz$, at driving current of $1.5\,I_{th}$.

In general, a Gaussian telescope[1] consists of two lenses L_1 and L_2 with focal lengths f_1 and f_2, respectively. L_1 and L_2 are aligned in such a way that the distance between them equals the sum of their focal lengths. Such alignment ensures that the transformed beam contains the correct phase distribution, which is important if we want to analyze the evolution of the mode profile from the laser facet (near-field) into the far-field. The magnification of the telescope is given by the ratio of f_1/f_2, for near-field measurements we used magnification of 35. An image of the front facet was projected onto a CCD camera array chip, situated in the focal plane of the imaging setup. The obtained near-field intensity distribu-

[1] also referred to as the beam expander

tion was consistent with other methods of its measurement [90]. A scheme of the system set-up is presented in Fig. 4.7, placed images of the near-field and far-field were taken for an old generation of laser diodes, series LD4551. The ridge with for these samples was $7\,\mu m$, the devices were operated in pulsed regime with pulse duration of $50\,ns$ and with the repetition rate of about $10\,kHz$.
The measurements allowed to identify the problem of weak transversal confinement in the old generation of our laser structures, which suffered from a leakage of the optical mode down into the gallium nitride substrate. Strongly modulated near-field pattern and a number of side lobes observed in the far-field, which in case of (Al,In)GaN LDs are assigned to substrate modes [91, 92, 93], clearly indicated the necessity to optimize the waveguide design. A detailed description of the newly proposed approach to improve the transversal optical confinement will be presented in section 4.4 of this chapter.
For spectral measurements we could alternatively place a single mode fiber, also positioned in the focal plane of the imaging system. The single mode fiber was used in combination with a high resolution spectrometer (of about $0.005\,nm$), capable to reveal longitudinal mode structure.
The combined measurement of near-field and far-field allows to retrieve the phase of the laser mode and therefore address issues like beam steering, carrier induced or thermal lensing, and also formation of filaments. Investigations of the near-field pattern performed at different driving currents below and above the lasing threshold permits for direct observation of the dynamics of the optical mode distribution with changing operating conditions. An example of such study is demonstrated in Fig. 4.8, performed for samples LD4551, for which the weak transversal waveguidnig resulting in a leakage of optical modes was identified.

There are several mechanisms responsible for changes induced in the optical field pattern in a chaotic system of a laser diode. Under carrier injection close to the lasing threshold, the spatial distribution of the electromagnetic field is approximately uniformly spread on a LD facet, which is associated with diffraction effects and the wavefront divergence due to non-uniform distribution of injected carriers across the laser ridge. Such behavior is consistent with theoretical predictions studying the formation of an optical wavefront under conditions close to lasing threshold [94]. The low laser beam intensity and no gain saturation ensure that the current flow path induces excited carrier distribution, which in turn modifies the refractive index, decreasing its value as the carrier concentration increases.

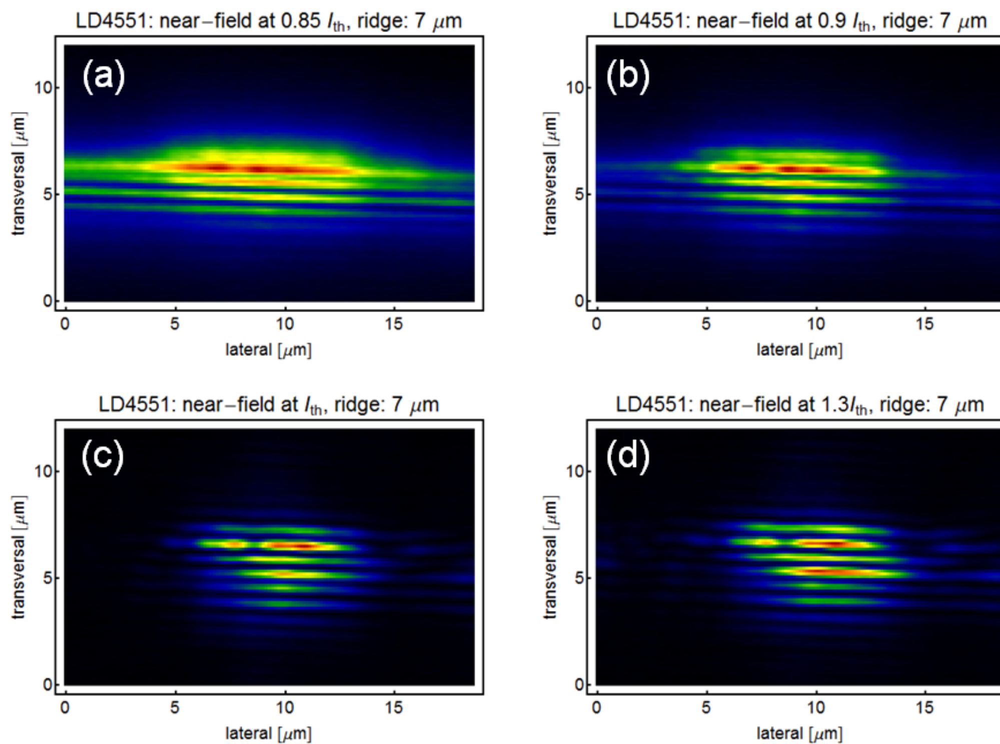

Figure 4.8: LD4551: near-field image taken at different currents: (a) $0.85\,I_{th}$, (b) $0.9\,I_{th}$, (c)I_{th} and (d) $1.3I_{th}$.

On the other hand are temperature induced effects, which act in opposite direction. Defocussing of the laser beam, on account of increased carrier concentrations, which takes place beneath the upper p-type electrode is counterbalanced by a stronger, temperature-induced waveguiding in both lateral and transversal directions. Finally, the impact caused by the antiguiding of the gain medium and diffraction effects make the beam wavefront divergent.

Antiguiding of a gain medium is responsible for the effect of detuning lasing frequency from the value corresponding to the maximum of the gain curve and originates from the carrier concentration noise in a laser's active region [87]. This effect can be estimated by the antiguiding factor R_{ant}, which is a measure of the magnitude of the amplitude-phase coupling, arising from the strong refractive index dependence on the carrier density. R_{ant}, also known as *linewidth enhancement factor*, is given by a relation between the medium refractive index n, its change δn induced by carrier density and the differential gain $\partial g/\partial N$ experienced by

photons of a given wave vector $\vec{k}$ [87]:

$$R_{ant} = -\frac{k}{n}\frac{\frac{\partial(\delta n)}{\partial N}}{\frac{\partial g}{\partial N}} \tag{4.10}$$

For nitride materials the values of the antiguiding factor are rather large and extend from 4 to 15, depending on a carrier injection level and thickness of quantum wells, as reported in theoretical [95] as well as experimental [87] investigations. These relatively large values originate from nitride's high joint densities of states, which is a consequence of a wider bandgap and larger electron and hole effective masses, as compared with conventional III-V compounds.
One of the adverse effects of large antiguiding factor's value results in greater tendency to formation of filaments. At sufficiently high excitation levels above threshold, the intensity distribution of a laser cavity mode causes spatial hole burning along the resonator, reducing the carrier density in those regions and leading to saturation of gain. In consequence, a local increase of the refractive index along the resonator results in enhanced focusing of the lasing mode, which burns a deeper hole in spatial carrirer distribution and even stronger focusing (see Fig. 4.9). The phenomenon is frequently reffered to as *filamentation* [88].
Filamentation results in a shift of emission wavelength and significant spectral broadening, in response to changes in the excited carriers density [18]. In addition, the localization of filaments is enhanced by inhomogeneities of the crystalline structure associated with dislocations. Excited carriers, which are left undepleted by the fundamental mode, contribute to a multi-mode operation and weaken spatial coherence of the laser beam. This results in a multi-lobe far-field pattern, which denies the device suitability for applications where sharp beam focusing is essential (e.g. high-density optical data storage). In case of broad area lasers working in high-power regime, formation of filaments is unavoidable as evidenced in a number of experimental reports [94, 96, 97]. As predicted by theoretical analysis [95], the diffraction limit of a single filament is around $3\,\mu m$. Therefore, the lateral single mode operation of a LD is limited to ridge widths close to $2\,\mu m$ [92, 98].
In addition, in structures with wider ridge higher order lateral modes are subject to higher gain, as observed experimentally [69] and confirmed theoretically [70], which stems from a different overlap of the lossy p-type layers. The higher order modes have more degrees of freedom to optimize overlap with the active region

and at the same time minimize overlap with the p-layers. For example, for structures with etch depths close to the p-cladding / p-waveguide interface, the ridge edge pushes the outer lobes of higher order lateral modes into the n-waveguide region.

In Fig. 4.9 is a comparison of near-field images and high resolution spectra with distinguishable longitudinal Fabry-Perot modes of laser's resonant cavity. Measurements were taken around lasing threshold for sample LD4760 d48 with improved transversal optical mode confinement. The ridge width was 6 μm, the cavity length was 700 μm and the device was pulsed operated with pulse duration of 50 ns at repetition rate of 10 kHz. In near-field images the presence and formation of filaments can be identified.

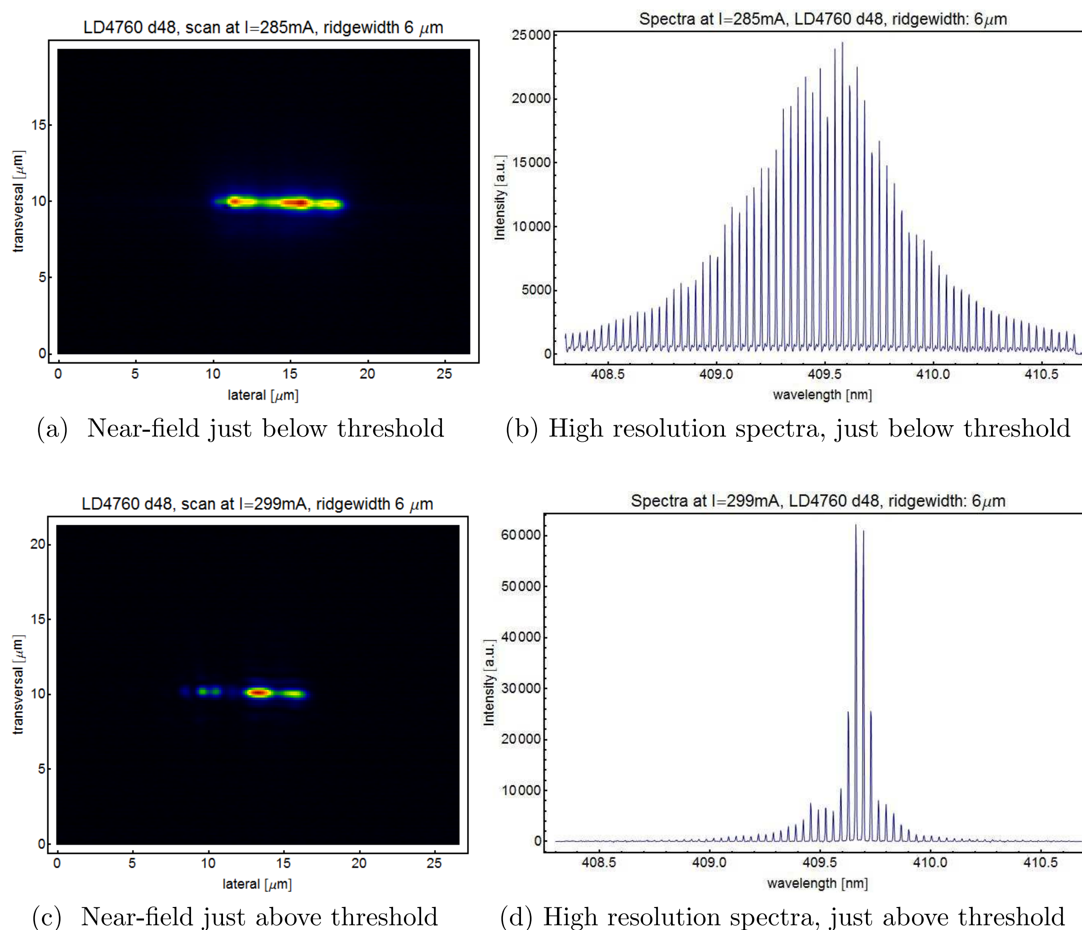

(a) Near-field just below threshold

(b) High resolution spectra, just below threshold

(c) Near-field just above threshold

(d) High resolution spectra, just above threshold

Figure 4.9: A comparison of near-field images and high resolution spectra taken around lasing threshold for sample LD4760 d48 with improved transversal confinement. The ridge width was 6 μm. In the near-field the presence and formation of filaments can be identified. Spectral resolution allows to see the longitudinal modes structure of laser's cavity.

4.4 Optimizing transversal confinement

The transversal confinement of an optical mode is always realized through the refractive index engineering [18]. In conventional GaAs/AlAs systems one has almost full freedom of choice of layers content and thickness, owing to the good lattice match existing between GaAs and AlAs. In case of InGaN-GaN-AlGaN system, wider bandgap AlGaN alloy forms cladding layers providing optical confinement. However, as a result of significantly smaller lattice constants of this compound, flexibility in design of LDs cladding is severely limited due to the presence of tensile strain in AlGaN layers deposited on gallium nitride substrate. Excessive build-up of this strain leads to numerous problems, such as macroscopic epistructure bowing, cracking or creation of misfit dislocations [99]. On the other hand, the lack of the proper transversal mode confinement transforms the transparent gallium nitride substrate into a parasitic waveguide for the LD emission, taking away significant fraction of the radiation traveling through the laser cavity. The importance of this effect was pointed out by Smolyakov *et al.* [100, 74] who gave the nickname *ghost modes* to these modes propagating in the substrate, which may couple to the waveguide mode through evanescent waves in the cladding layer. The lasing mode in waveguide layers exists as an evanescent wave, whose intensity exponentially decays into the cladding layers. If the thickness of the cladding layer is much larger than the penetration depth of the decaying mode, optical losses associated with the penetration of laser emission into the passive waveguides are negligible. This penetration depth depends on the refractive index step at the GaN waveguide / AlGaN cladding layer interfaces. In case of nitride-based laser diodes the reasons to use relatively thin claddings are justified by allowing to avoid an increase in the series resistance of the diode, to avoid generation of cracks and other defects and to reduce the growth time. The light partially propagating in the substrate increases internal losses and decreases the confinement factor for the waveguide mode. Lasing occurs in a higher-order mode with modifications in the modal spatial profile, observed both in the near-field and the far-field. Because the parasitic modes are typically sustained by the GaN substrate or buffer layers, the effect is also referred to as *substrate modes* [101]. In order to suppress the mode leakage, leading technological groups use a thick AlGaN cladding as it is feasible to take into account the strain accumulation. For instance, the group of Nichia Chemical reported on using a very thick, $5\,\mu m$ $Al_{0.05}Ga_{0.95}N$: Si lower cladding layer [102]. OSRAM

Opto Semiconductors achieved a suppression of substrate modes by increasing the thickness of the lower cladding layer to $2\,\mu m$ [101].
A kind of a fingerprint of the existence of substrate modes was found during degradation studies performed on our LD structures. From a SEM image of an aged LD sample a package-induced failure was identified with carbon deposits on the facet. The pattern of the deposits corresponds well with the electric field oscillating modes, clearly propagating outside the active region as can be seen in Fig. 4.10. This was in agreement with our near-field measurements performed on operating devices. The package-induced failure was then eliminated by sealing in a proper mixture of nitrogen and oxygen. The problem of the weak transversal confinement of the mode for the old generation of our laser structures could be solved using an alternative approach of the mode leakage suppression by using cladding layer with reduced refractive index.

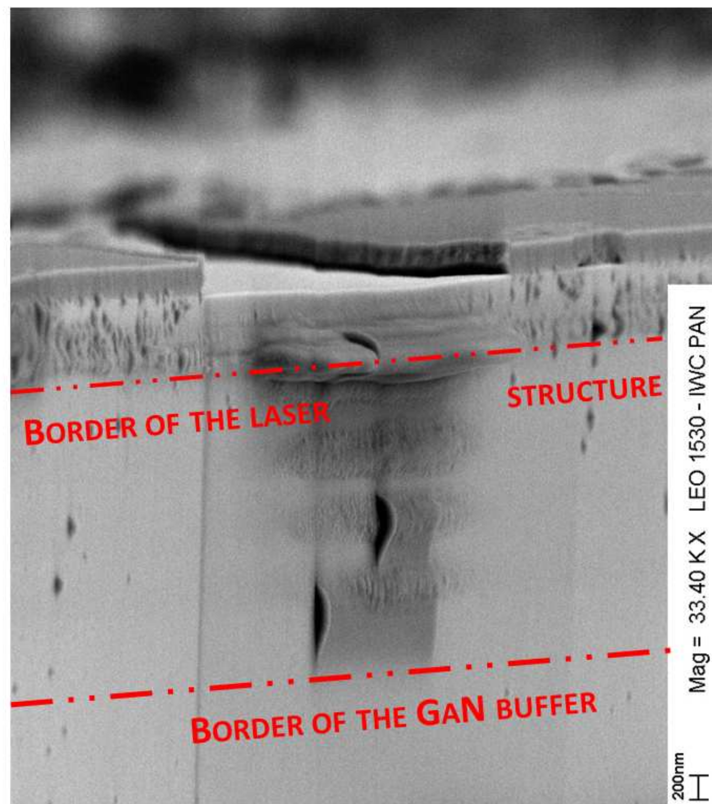

Figure 4.10: SEM image of an aged LD sample. On the facet we can see some deposits which correspond to the pattern of an oscillating electromagnetic field, penetrating the substrate.

4.4.1 Plasmonic cladding

Introducing an additional layer of highly oxygen-doped gallium nitride deposited on the top of a bulk GaN substrate resulted in a complete suppression of the mode leakage without increasing the thickness of the AlGaN cladding layer. This choice was inspired by a well known fact in semiconductor physics – a strong dependence of the dielectric function of semiconductors on free carrier concentration in the vicinity of the plasma frequency. In this region the dielectric function $\varepsilon(\omega)$ can be expressed as [103]:

$$\varepsilon(\omega) = \varepsilon_\infty \left[1 - \frac{{\omega_p}^2}{\omega(\omega + i\gamma)}\right], \tag{4.11}$$

where ε_∞ is the optical dielectric constant, γ is the electron damping term and ω_p is the plasma frequency given by the following relation:

$${\omega_p}^2 = \frac{Ne^2}{m^* \varepsilon_\infty \varepsilon_0}, \tag{4.12}$$

with N - free electron concentration, e - the electronic charge, m^* - the effective mass of the electron and ε_0 - the vacuum permittivity.
Experimental studies on the plasma frequency in gallium nitride plasmonic material report that ω_p is in the range of 2500 - 2800 cm^{-1} [104]. If we neglect the electron damping term, the approximated dielectric function is expressed as:

$$\varepsilon(\omega) = \varepsilon_\infty \left(1 - \frac{{\omega_p}^2}{\omega^2}\right), \tag{4.13}$$

From the last expression one can immediately see that for ω values reasonably close to the plasma frequency, a substantial decrease of the dielectric constant and therefore of the refractive index occurs. Materials with high enough electron concentration can thus serve as a cladding layer and will be referred to as *plasmonic cladding.* The additional advantage of a plasmonic material is that the lattice mismatch between low and high electron concentration layers is rather low in contrast with high strain introduced by increasing Al composition in AlGaN alloys, conventionally used for claddings [105]. For example, a 10% AlGaN layer grown on GaN substrate is exposed to a tensile strain, which is 10 times stronger as compared to the compressively strained plasmonic-GaN cladding grown on bulk GaN. The refractive index of this high-electron concentration GaN plasmonic layer was measured experimentally using spectrally resolved ellipsometry.

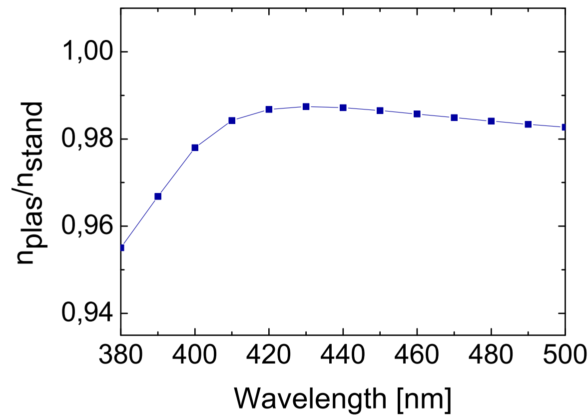

Figure 4.11: The ratio between the low and high free electron concentration gallium nitride. Measurements were performed using spectrally resolved ellipsometry.
In collaboration with Piotr Firek and Jan Szmidt, Institute of Microelectronics and Optoelectronics Warsaw University of Technology.

As depicted in Fig. 4.11 showing the ratio between low and high free carrier density materials, at 400 nm the refractive index of the high electron concentration gallium nitride crystal is 2% lower than that of the low electron concentration material.

To incorporate the new design with plasmonic bottom cladding the InGaN LDs were fabricated on substrates prepared in the following way: first, the freestanding bulk GaN crystal obtained via hydride vapor phase epitaxy (HVPE) [106] with electron concentration of $1 \cdot 10^{18}$ cm^{-3} was mechanically polished in such a way that its surfaces (Ga-polar and N-polar) were misoriented by 0.5° with respect to the crystallographic c-plane of the crystal [31]. Subsequently, such wafer was mechanochemically polished both sides and placed into a high-pressure reactor, where it was overgrown with about 10 μm of high electron density GaN layers on both Ga- and N-polar faces. Free electron concentration in these layers was not smaller than $5 \cdot 10^{19}$ cm^{-1} and this high doping level is attributed to the high content of oxygen donors. The merit of this composite configuration (used as a substrate for subsequent growth of laser structures) was the possibility of combining the advantage of large lateral sizes and low defect density of HVPE crystals with ultra-high doping level available in the high pressure method. Laser devices were then grown and fabricated in a standard way, as it was described in the previous sections of this chapter. As a reference device, an identical epistructure was fabricated, but deposition was done on a standard HVPE gallium nitride

substrate. A schematic representation of the two designs is compared in Fig. 4.12. The comparison between the current - optical power $(I - P)$ characteristics of these two laser structures is shown in Fig. 4.13.

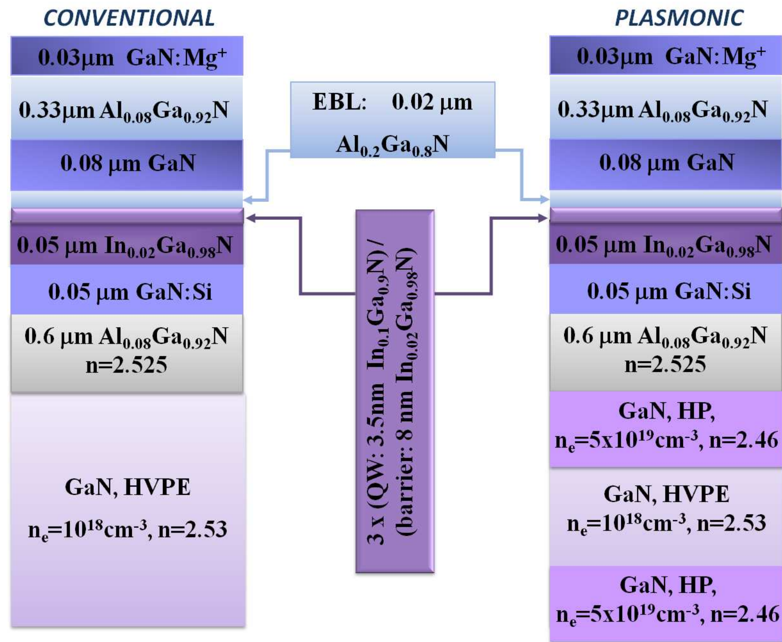

Figure 4.12: Schematic representation of two structures: an old design and a new one incorporating plasmonic cladding.

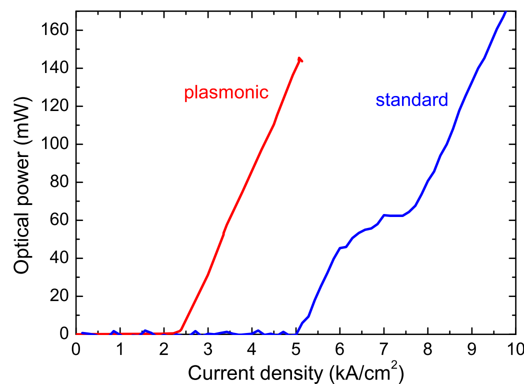

Figure 4.13: Current - optical power characteristics measured for laser structures grown on a standard HVPE substrate and on the plasmonic substrate. The stripe dimensions were 20 x 700 μm^2. The devices were cw operated, at room temperature.

A striking reduction in the threshold current density is clearly visible – it decreases from $5.2\,kA/cm^2$ for the reference structure to $2.3\,kA/cm^2$ for the structure with the plasmonic cladding. N.B., the slope efficiency for both structures remains similar, close to $0.5\,W/A$. This reduced value of the efficiency is caused by the pronounced light absorption in the p-side layers of the structure. Such problem can be solved by introducing asymmetric claddings [107] or better spatial Mg profiles. An interesting and gratifying feature was that the device fabricated with the new designed plasmonic waveguide did not show any kink in its $I-P$ curve, which can be attributed to the improvement in the vertical waveguiding properties of the modified structure. Indeed, the decrease of the threshold current density is accompanied by pronounced changes in the near field patterns observed for these two generations of devices, as can be seen comparing Fig 4.8 and 4.9.

4.4.2 Waveguide mode simulations

In order to further elucidate this strong improvement calculations of the transversal mode distribution were performed using a solver based on two-dimensional plane-wave expansion method, which includes optical gain and losses in the structure. The code was originally developed and implemented in a script language of Mathematica (Wolfram Research) within the group of prof. Ulrich Schwarz (University of Regensburg).
The simplest approach for analyzing the waveguide properties of a laser diode is to consider the analytic solutions of a symmetrical three-slab model with lossless cladding layers, which are infinite in extent. This approach, however, is not suitable for the nitride-based LDs due to their complex structure design, which is both asymmetric and lossy. To calculate the optical field profile in such structures the approach of Bergmann and Casey [71] is applied and bases on an algorithm using 2×2 complex transfer matrices formed by boundary conditions at the layer interfaces. Considering a multilayer planar waveguide (see Fig. 4.14 for reference) we search for solutions of electromagnetic fields, which fulfill Maxwell's equations. For sinusoidal time-varying fields with TE polarization – electric field oscillating in the $\hat{\mathbf{x}}$ direction – traveling in the $\hat{\mathbf{z}}$ direction – solutions have the form

$$E_x(y,z,t) = E_{x,j}(y)\; e^{i(\omega t-\beta z)} \tag{4.14}$$

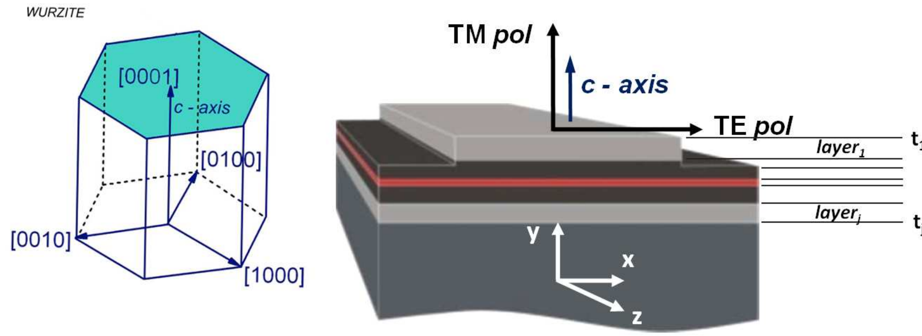

Figure 4.14: Schematic illustration of laser waveguide geometry showing transverse electric (TE) and transverse magnetic (TM) polarizations constituting two orthogonal solutions of the waveguide problem. A scheme of the interfaces positions used to define the laser structure for Transfer Matrix Method-based calculations is shown on the right.

in the $j-$th layer. The TE amplitude is denoted by $E_{x,j}(y)$ and solves the following wave equation

$$\frac{\partial^2 E_{x,j}}{\partial y^2} - \left(\beta^2 - k_0^2 \tilde{n_j}^2\right) E_{x,j}(y) = 0. \tag{4.15}$$

Each layer has a complex refractive index, $\tilde{n_j} = n + i\kappa$, where κ is the extinction coefficient. Absorption occurs when $\kappa < 0$, gain occurs when $\kappa > 0$. The free-space wave number k_0 corresponds to the frequency ω or the vacuum wavelength λ_0 of the mode through $k_0 = \omega/c = 2\pi/\lambda_0$ and β is the complex propagation constant. The general solution to Eq. 4.15 is

$$E_{x,j}(y) = A_j e^{\gamma_j (y-t_j)} + B_j e^{-\gamma_j (y-t_j)}, \tag{4.16}$$

where A_j and B_j are complex coefficients to be determined by the boundary conditions at the interfaces, $\gamma_j = \sqrt{\beta^2 - k_0^2 \tilde{n}^2}$, and t_j is the position of the boundary between the j and $j+1$ layers (see Fig. 4.14). The effective index of refraction is given by $n_{eff} = \mathrm{Re}[\beta]/\mathrm{k}_0$ and the absorption of the optical mode is given by $\alpha = 2\,\mathrm{Im}[\beta]$.

The boundary conditions for TE modes are that the electric field and its derivative normal to the interface must be continuous. These conditions, along with layer thickness defined as $d_j \equiv (t_{j+1} - t_j)$, yield to the following relations for the

coefficients:

$$\begin{aligned} A_j\ exp\ (\gamma_j\, d_j) + B_j\ exp\ (-\gamma_j\, d_j) &= A_j + B_j, \\ A_j\, \frac{\gamma_j}{\gamma_{j+1}}\ exp\ (-\gamma_j\, d_j) - B_j\, \frac{\gamma_j}{\gamma_{j+1}}\ exp\ (\gamma_j\, d_j) &= A_{j+1} - B_{j+1}. \end{aligned} \tag{4.17}$$

The last two expressions can be solved, leading to a recursive relationship:

$$\begin{bmatrix} A \\ B \end{bmatrix}_{j+1} = \underbrace{\begin{bmatrix} \left(1 + \frac{\gamma_j}{\gamma_{j+1}}\right) \frac{exp\ (\gamma_j\, d_j)}{2} & \left(1 - \frac{\gamma_j}{\gamma_{j+1}}\right) \frac{exp\ (-\gamma_j\, d_j)}{2} \\ \left(1 - \frac{\gamma_j}{\gamma_{j+1}}\right) \frac{exp\ (\gamma_j\, d_j)}{2} & \left(1 + \frac{\gamma_j}{\gamma_{j+1}}\right) \frac{exp\ (-\gamma_j\, d_j)}{2} \end{bmatrix}}_{T_j} \times \begin{bmatrix} A \\ B \end{bmatrix}_j, \tag{4.18}$$

which connects the coefficients from the first to the last layer as follows:

$$\begin{bmatrix} A \\ B \end{bmatrix}_z = T_{z-1}\, T_{z-2} \cdots T_3\, T_2\, T_1 \begin{bmatrix} A \\ B \end{bmatrix}_1 = \mathbb{T}_{total} \begin{bmatrix} A \\ B \end{bmatrix}_1 \tag{4.19}$$

For guided modes, $E_x(y \to \pm\infty) \longrightarrow 0$, and requires that $B_1 = 0$ and $A_z = 0$; the decay can be due to dielectric or absorptive process. The latter leads to a known form of a *transfer matrix* for electromagnetic field propagating in a multi-stack system:

$$\begin{aligned} \begin{bmatrix} 0 \\ B \end{bmatrix}_z &= \mathbb{T}_{total} \begin{bmatrix} A_1 \\ 0 \end{bmatrix} \\ &= \begin{bmatrix} t_{11} & t_{12} \\ t_{21} & t_{22} \end{bmatrix} \begin{bmatrix} A_1 \\ 0 \end{bmatrix}. \end{aligned} \tag{4.20}$$

The only variable in Eq.(4.20) is β, all other quantities are design and material parameters (defined by layer thicknesses and compositions). Fulfilling the last equation requires that $t_{11}(\beta) = 0$, which gives the condition the numerical algorithm uses to find a solution.

To confirm the importance of refractive index matching between the substrate and bottom cladding layers, calculations of the mode intensity distribution were performed for two sorts of waveguide design (old and new generation), differing only in the bottom part, which in case of the new one incorporated the plasmonic part of the substrate. Details of the epitaxial structure are given in Table 4.1. Fig. 4.15 illustrates the waveguide structure profile drawn due to the refractive index of epi-layers. In the calculations we neglected the presence of the low carrier density material existing below the plasmonic layer, but the thickness of

the latter ($> 10\mu$m) prevents the mode from entering deeper into the HVPE GaN substrate, as was verified by the simulations. The results are shown in Fig. 4.16.

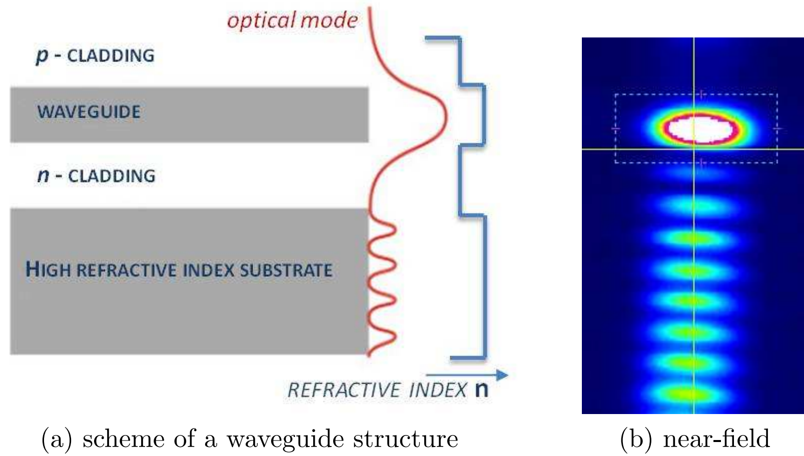

(a) scheme of a waveguide structure (b) near-field

Figure 4.15: Schematic representation of the waveguide structure given by the refractive index profile of epi-layers (a), (b) shows registered near-field image with strong substrate modes (sample LD4190d18).

Table 4.1: Waveguide - epitaxial design for old and new generation structures.

Layer	Material	Thickness [nm]	Refractive index* at 405 nm
p-subcontact	$GaN:Mg^+$	30	2.5038
p-cladding	$Al_{0.08}Ga_{0.92}N$	330	2.4484
waveguide	GaN	80	2.5038
EBL	$Al_{0.2}Ga_{0.8}N$	20	2.3441
active	$In_{0.1}Ga_{0.9N}/In_{0.02}Ga_{0.98}N$	3 x (3.5 / 8)	2.8/2.6
injection	$In_{0.02}Ga_{0.98}N$	50	2.6
waveguide	GaN:Si	50	2.5038
n-cladding	$Al_{0.08}Ga_{0.92}N$:Si	600	2.4484
new: plasmonic	*GaN-n^+*	*10 000*	2.4572
substrate	GaN, *HVPE*	120 000	2.5038

* *Refractive index values for AlGaN and InGaN were taken from Ref.[108]. In case of plasmonic GaN the refractive index value was obtained from spectrally resolved ellipsometry.*

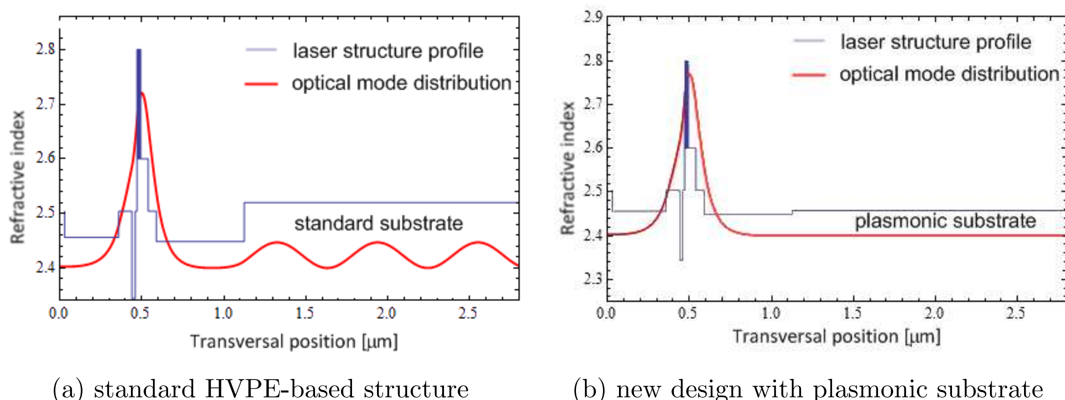

(a) standard HVPE-based structure (b) new design with plasmonic substrate

Figure 4.16: Simulations of a 1-dimensional optical mode distribution based on the Transfer Matrix method applied to nitride-based laser waveguide structure: (a) old-generation structures based on a HVPE substrate and (b) new-generation structures with plasmonic layer. In the latter case we do not observe modes propagating within the substrate.

Fig. 4.16a confirms the existence of the oscillating mode in the substrate, for structure with $Al_{0.08}Ga_{0.92}N$ layer serving as a lower cladding. Indeed, as was already mentioned earlier in this chapter, many groups developing LDs were forced to apply much thicker cladding in order to stop the mode leakage [101, 102]. In Fig. 4.16b are shown results of simulations performed for LDs with the plasmonic structure. The refractive index of the plasmonic GaN is almost identical to that of $Al_{0.08}Ga_{0.92}N$. This low refractive index value is sufficient to prevent the mode from leaking into the substrate. An additional advantage of this approach is clear from the measurement of the lattice parameter a for $Al_{0.08}Ga_{0.92}N$ and plasmonic GaN. The x-ray diffraction measurements yields the mismatch between the a-lattice parameters in the GaN-$GaN_{plasmonic}$ system of roughly 0.02%. This is one order of magnitude less than the lattice mismatch of 0.2% for $Al_{0.08}Ga_{0.92}N$-GaN system, meaning that the plasmonic cladding does not contribute to the increase of strain in the structure. Looking at the similarities of $Al_{0.08}Ga_{0.92}N$ and plasmonic-GaN refractive indicies, the question arises weather it is possible to eliminate completely the lower AlGaN cladding layer. This step would be beneficial in terms of structure simplicity and further reduction of strain. However it could lead to increased free carrier losses in the waveguide due to the presence of electron plasma. The right compromise between strain reduction and low waveguide losses has to be found in order to design a fully optimized device.

Chapter 5

Nitride LDs for spectroscopic applications

In this chapter I briefly discuss the applicability of nitride LDs to molecular and atomic spectroscopy. Then I present results of tuning of the laser diodes by two different methods. The first (section 5.1) was based on external cavity tuning with a diffraction grating in Littrow configuration, where I obtained 5.5 nm tuning range. The second method was based on temperature tuning, where I obtained a very broad range of 16 nm (section 5.2).
In section 6.3 I describe an example of adapting a pulsed-operated LD emitting around 414 nm to NO_2 concentration measurements by means of Cavity Ring Down Spectroscopy. These measurements were performed in collaboration with prof. Tadeusz Stacewicz from Warsaw University and Jacek Wojtas and prof. Zbigniew Bielecki from Military University of Technology. We were able to reach the detection level of single ppb. Finally, I present results of a frequency-stabilized cw-operated LD by a diffraction grating in Littrow configuration. The obtained spectral linewidth was close to 100 MHz and the emission stability was observed for periods of 30 minutes without using any feedback loop laser frequency control.

Having reached certain maturity, violet-blue nitride-based LDs became commercially available. With regard to their short wavelength, reliable lifetime, low power consumption they became suitable for applications such as fast laser printing, high density optical data storage and pico-size projectors. (Al,In) GaN-based LDs also find many scientific applications, e.g. in spectroscopy, where they can easily compete with expensive and large standard spectroscopic sources (gas and

solid-state lasers). However, spectroscopic requirements expect not only reliability of the laser device, stability of wavelength and power generation as well as good beam quality. Equally important is the possibility to work with the laser in a broad, adjustable spectral range. Although semiconductor LDs can be especially designed to operate at a given wavelength (varying doping and composition), broad spectral tunability is still an important feature of the device.
Spectral tuning of a laser diode can be performed in different ways, large wavelength shifts can be reached by means of pressure tuning (e.g. Ref. [109]). Smaller shifts in the emission wavelength can be obtained varying the temperature at which the laser is operating. Another possibility for fine tuning is to vary the drive current of the LD. Finally the external cavity scheme can be employed [110], where a dispersive element (e.g. a diffraction grating) is used to form an external resonator. Part of the light (the amount and spectral selection depend on the grating's characteristics) is fed back into the laser, which plays a role in the active section of the resonator, where the amplification process takes place. Roughly, selection of the lasing frequency is obtained by spatially picking out the coupled wavelength simply through changing the angle of the diffraction grating with respect to the path of the incoming beam.
The UV and blue spectral region (approximately 395 - 440 nm) – particularly interesting due to electronic absorption frequencies own by many atoms and molecules – became directly accessible with the development of nitride-LDs-based spectroscopic setups. Zybin *et al.* [111] specified 34 chemical elements displaying strong absorption lines reachable with violet-blue lasers. Precise atomic spectroscopy employing these light sources was already demonstrated for indium [112, 113], rubidium [114], potassium [115] and calcium [116]. Among compounds which are commonly present in the atmosphere, nitrogen dioxide has maximum of violet-blue absorption bands in the 370-440 nm spectral range. In this chapter results of research on tuning of laser diodes (fabricated at TopGaN Ltd.) in an external cavity system and by means of temperature will be presented. Examples of applications to detection of nitrogen dioxide in free atmosphere using Cavity Ring Down Spectroscopy (CRDS) sensor adapting (Al,IN) GaN LDs will be described.

5.1 External Cavity Tuning

For high precision atomic spectroscopy, where operation with precise wavelength is required (gas analysis, absorption spectroscopy) tuning and spectral characteristics of ridge-waveguide LDs are far from ideal. Coupling the laser to the external resonator affects the emission spectrum of the diode in addition to modification of the threshold current and total output power [110, 18]. In order to achieve single mode operation and tunability of the laser line over the range of gain of the diode medium, frequency selective feedback is applied – typically through diffraction gratings in either Littrow or Littman– Metcalf configurations.
In the more often employed Littrow configuration, the first order of diffraction is fed back directly into the laser diode waveguide while the specular reflection from the grating (0th order) forms the output beam. Tuning of the wavelength is obtained by rotation of the grating but introduces undesirable wavelength-dependent direction of the output beam. In addition, a sort of a *trade–off* on diffraction efficiency of the grating itself must be considered because a strong coupling (high diffraction efficiency in the 1st order) results in low output power.

5.1.1 ECDL and tuning results

Following Ref. [117] the present Extended Cavity Diode Laser system (ECDL) is based on an improved Littrow configuration with an additional mirror which provides fixed output direction without significant reduction of power in the 0th order of diffraction (Fig. 5.1). The laser beam is collimated through an aspheric lens (C330T form Thorlabs). A diffraction grating with groove density of $1800\,mm^{-1}$ (Edmund Optics) was used. The grating efficiency was 60 % while the cavity length L was about $10\,cm$. The spectra were registered using Spectra-Pro 500 spectrometer (Acton Research), equipped with a CCD detector. The spectral resolution of the system was 0.5 Å. Antireflection coating of a single quarterwave layer of SiO_2 (with reflectivity below 1 %) has been applied to broaden the tuning range as well as to improve the ECDL stability.
When the external cavity is aligned properly (i.e. feedback from the diffraction grating is provided) the output spectra change – multimode laser operation switches to the single mode regime, with much narrower spectrum line (Fig. 5.2). Single mode operation was obtained over the tuning range of $\Delta\lambda = 5.5\,nm$ in the

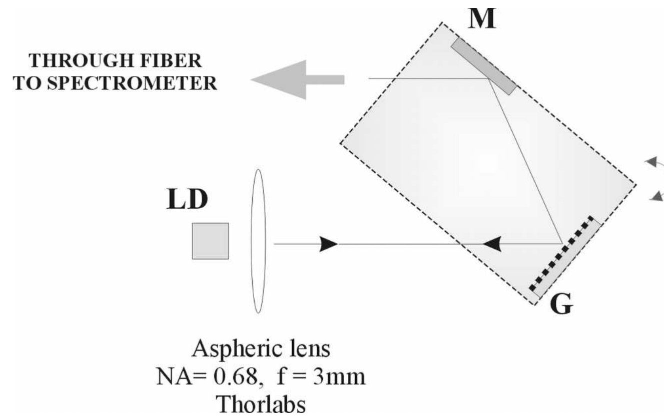

Figure 5.1: **E**xtended **C**avity **D**iode **L**aser system: **LD** – laser diode, **G** – diffraction grating, **M** – mirror

violet spectral region. The threshold current of the diode laser without external feedback was approximately $740\,mA$. To receive the best coupling to the external cavity the driving current was set just below the diode threshold ($730\,mA$) and system alignment was performed until laser action occurred.

Two operation currents were chosen to compare the performances of the constructed ECDL system, one somewhat above threshold and the other high above threshold – Fig. 5.3 demonstrates gathered spectra at different grating tilts with the two currents of $790\,mA$ and $1200\,mA$, respectively. In the first case the tuning range was $\Delta\lambda = 5.18\,nm$ and the envelope of the lines intensity was narrower comparing to the second case with the tuning range of $\Delta\lambda = 5.55\,nm$. The internal mode of the diode was laying around $398\,nm$, so the laser preferred tuning into the longer wavelengths accordingly with the gain curve asymmetric character. The remains of the internal mode, present in the middle of the tuning range (Fig. 5.3b), originate from the two registered spectra at the boundaries of the tuning range and can be explained that geometrically it is not possible to feed the beam back into the laser's waveguide, but also that the cavity mode no longer coincides with the material gain. It is worth to mention that similar type of laser was tuned within the range of $10\,nm$ by applying hydrostatic pressure [109].

The optical output power from such a system is usually diminished due to substantial losses originating from the characteristics of the applied diffraction grating, external mirror reflections and the geometrical factor (coupling efficiency) of the provided feedback. The sample presented here was operated with pulsed current ($50\,ns$ pulses, $10\,kHz$ repetition rate), the threshold current of the solitary

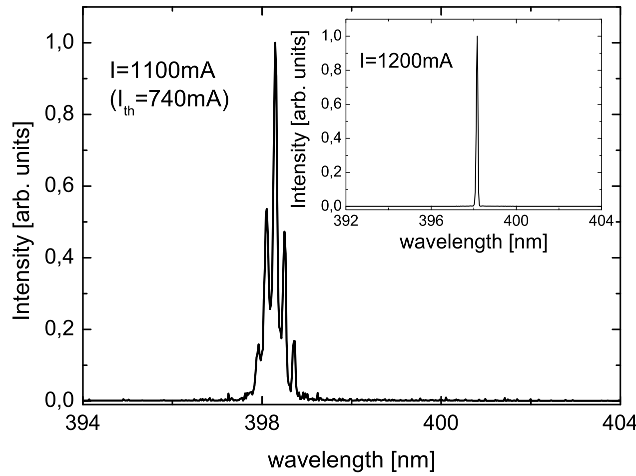

Figure 5.2: Comparison of registered spectra without coupling (free running diode, multi-line operation) and with applied feedback (single mode operation) for sample LD2761 with $10\,\mu m$ ridge.

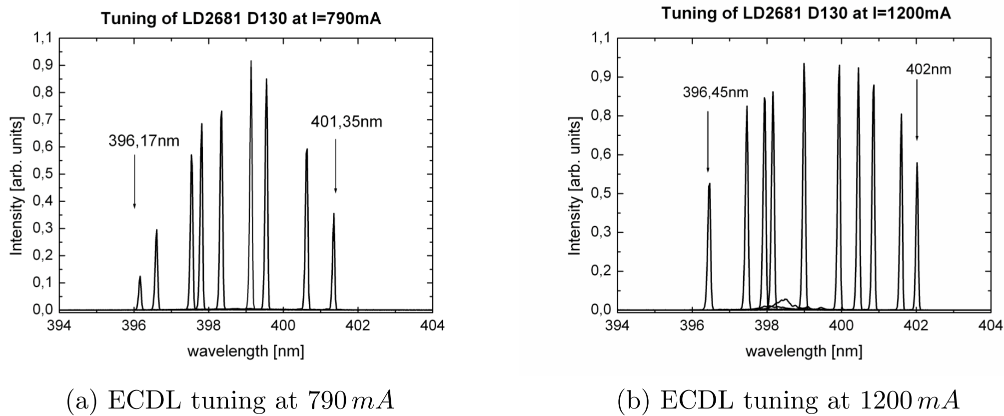

(a) ECDL tuning at $790\,mA$

(b) ECDL tuning at $1200\,mA$

Figure 5.3: Registered ECDL lines at different tilts of the grating under (a) low, $790\,mA$ and (b) high, $1200\,mA$ operating current. Sample LD2681 D130 with $20\,\mu m$ ridge.

diode was $I_{th} = 740\,mA$. The peak power at operation current $I = 1250\,mA$ of the laser diode without feedback is $170\,mW$, at the same drive current the peak power of the external cavity output beam is $39\,mW$. A very rough estimation of the coupling efficiency based on the ray−tracing in the cavity yields that only around 2.5% of the light is fed back into the laser internal cavity. Comparing the power of the output beam with and without coupling yields $\eta \simeq 23\,\%$.

5.2 Temperature tuning

Having in mind spectroscopic applications of nitride laser diodes, it was interesting to examine the possible tuning range by means of temperature. Although InGaN lasers have the wavelength–temperature coefficient slightly smaller than conventional GaAs–based devices [118, 119], they may be designed to have very large thermal stability of their threshold current. The characteristic temperature T_0 [18] — a phenomenological parameter describing lasers' threshold current dependency on temperature — may easily exceed $200\,K$. Such thermal stability makes these lasers perfect candidates for temperature–tunable devices. In this section results of temperature tuning of a pulsed-operated MQW LD (sample D1 series LD3411, 5 x 500 μm stripe) characterized by very weak temperature dependence of its threshold current will be presented.

5.2.1 Experimental setup and Measured Tuning Range

Temperature tuning was performed using a specially designed setup in order to achieve good thermal stability during measurements. The laser chip was mounted p–type down on a copper cube of the dimensions of 2.5 x 2.5 x 1.2 mm^3, which mainly served as a heat spreader. This copper packaging was placed on a ceramic heater, a high temperature sealant was used as an adhesive layer. To ensure temperature measurements as close as possible to the laser diode chip, a blind hole of the diameter of $0.9\,mm$ was drilled just beneath the chip to insert the thermocouple. The heater with the laser diode was placed inside an appropriate cover (made of Teflon) in order to minimize convection effects and improve thermal stability of the laser. A very broad temperature tuning range of $16\,nm$ was obtained by increasing the ambient temperature by almost $200\,K$. The laser diode was tuned from the initial wavelength of $415\,nm$ at room temperature up to $431\,nm$ at 201 °C. The spectra were registered using *HR4000* Spectrometer (Ocean Optics with a spectral resolution of $0.02\,nm$), selected examples of spectra taken at different temperatures are presented in Fig. 5.4.

Multi-mode emission and strong mode hopping were observed while changing the ambient temperature. The latter even appeared more explicitly when the energy of emitted photon (taken from the spectra) vs. temperature was plotted (Fig. 5.5). The figure presents results from 3 series of temperature sweep measurements taken starting from room temperature to 200°C and back. Each step

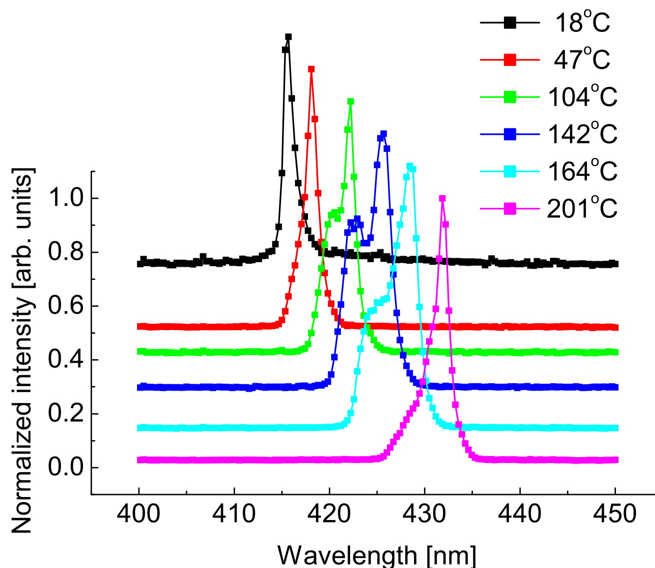

Figure 5.4: Registered spectra evidencing lasing wavelength shift of InGaN LD due to increase of ambient temperature by $200K$. Relatively large bandwidth is related to low resolution of the Ocean Optics spectrometer leading to the overlap of the lateral modes of the laser.

of heating up (cooling down) was followed by laser temperature monitoring with the thermocouple. After thermal stabilization, the LD was given a current pulse of duration $30\,ns$ and maximum value not exceeding $1.4\,A$. Emission spectra widths are plotted as error bars, emphasizing a broad multi-line emission.

Almost a linear decrease in emitted photon energy in the temperature range between 300 and $500\,K$ was observed. Roughly, the estimated slope was $\frac{dE_g}{dT} \sim -0.5\,meV/K$ (in the literature reported values of $\frac{dE_g}{dT}$ for GaN range from $-0.45\,meV/K$ to $-5.57\,meV/K$, see e.g. Ref. [120, 121, 122]). One of the empirical models to describe the temperature redshift of the bandgap, based on the electron – phonon interaction, can be expressed by the following formula:

$$E_g(T) = E_g(0) - \frac{2\alpha_B}{exp(\theta_B/T) - 1} \tag{5.1}$$

where $E_g(0)$ is the energy bandgap at $T = 0$, α_B is the strength of the electron - average phonon interaction, $[1/(exp(\theta_B/T) - 1)]$ is the Bose - Einstein statistical factor for phonon emission and absorption, θ_B is a temperature corresponding to an average phonon energy [122, 123, 124]. In order to compare the

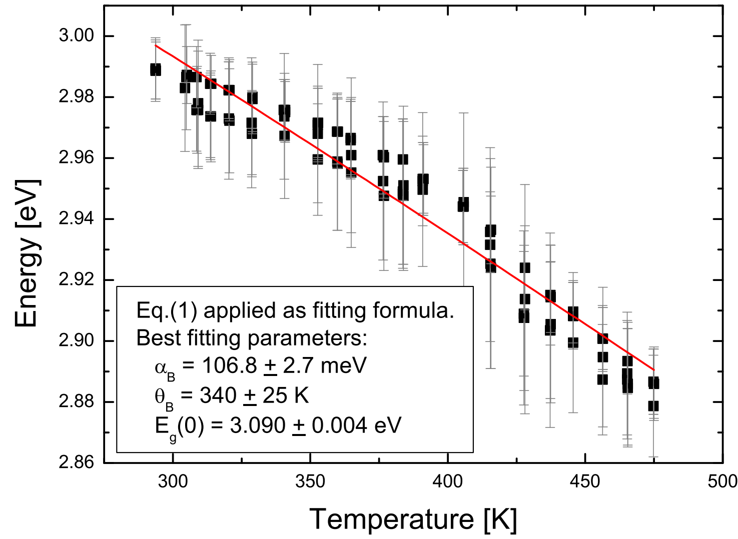

Figure 5.5: Lasing energy vs temperature. The widths of emission spectra, indicated by the error bars, confirm multiline emission demonstrated in Fig. 5.4. The solid line represents temperature induced energy bandgap shift for GaN. The best fitting parameters compare well with the literature. $E_g(0)$ in agreement with the reported values for InGaN with 8% indium content.

temperature induced shift of the emitted photon energy with the GaN bandgap behavior, experimental data were fitted using Eq. 5.1. These fitting parameters results are shown as the inset of Fig. 5.5, the best obtained values were $\alpha_B = 106.8 \pm 2.7\, meV, \theta_B = 340 \pm 25\, K$. They are in agreement with literature data on GaN (e.g. Ref. [122]). The energy gap value $E_g(0) = 3.090 \pm 0.04\, eV$ is in agreement with data reported by *Shan* [125]) for InGaN alloy with 8% indium content ($E_g(0) = 3.085\, eV$), which compares well with 10% indium composition in the case of QW layers of the investigated sample.

At λ equal to $420\, nm$ the distance between two adjacent longitudinal modes of the Fabry – Perot (F.P.) resonant cavity is around 0.7 Å. Experimental data (dots) clearly demonstrate that mode hopping occurs. Induced by temperature change, the laser's mode shifts until the the condition of F.P. resonance is lost and then another mode becomes the lasing one. In Fig. 5.6 the violet line shows temperature dependence of the wavelength shift of an arbitrary chosen longitudinal F.P. mode, determined by its refractive index *n(T)*, also temperature-dependent [122]. The temperature induced gallium nitride's energy gap shift, $E_g(T)$, was plotted as the pink line (after translating into wavelengths). The results illustrated in

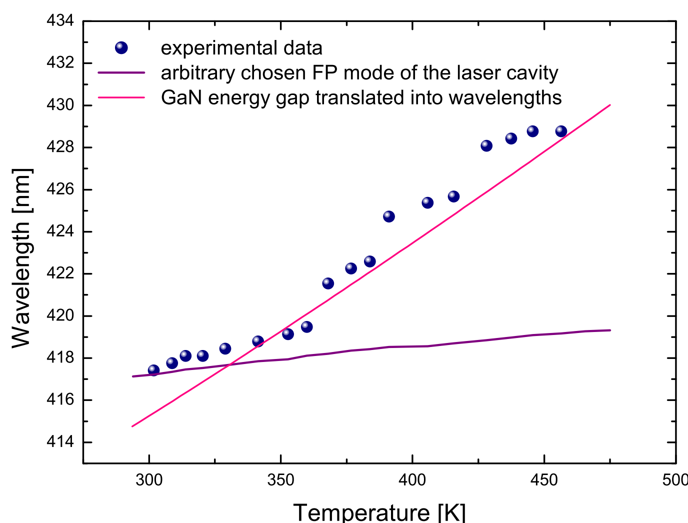

Figure 5.6: Emission wavelength vs temperature with comparison to the energy gap shift (pink) and F.P. longitudinal mode tuning due to refractive index dependence on T (violet line).

Fig. 5.6 show that laser's tuning curve characteristics in the wide temperature range follows the gallium nitride's energy gap behavior. However, looking closer at the tuning results in small temperature range, the observed mode-hop-tuning is strongly connected with sustaining the longitudinal Fabry-Perot-mode resonance condition. Usually, staying on the same mode is possible no more than within $20\,GHz$, and then lasing switches to another cavity mode.
Thermal stability of the device was examined by looking at the temperature induced threshold current shift, described by the phenomenological formula [18]:

$$I_{th}(T) = I_{th}(0) \cdot exp(T/T_0), \tag{5.2}$$

where T_0 is the characteristic temperature, a parameter which collectively represents temperature dependence of various mechanisms influencing the value of LD's threshold current – radiative and nonradiative recombination, carrier leakage, optical gain, etc. Fig. 5.7 plots threshold current (determined from L-I i.e. light-current characteristics of pulsed operated LD) as a function of temperature within the range of tuning. From around 20° C to around 50° C a decrease of the threshold current with an increase of temperature was observed, which is considered as an anomalous behavior. This anomaly has already been reported for InGaN lasers [126, 127, 128], nonuniform carrier distribution in the quantum wells

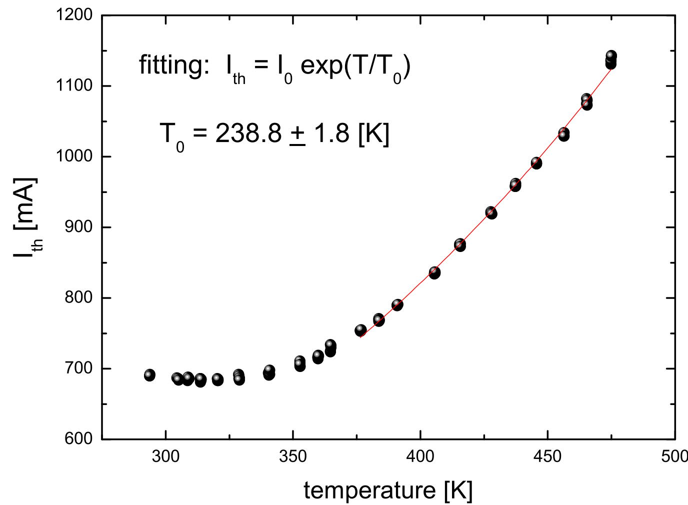

Figure 5.7: Threshold current as s function of increasing temperature. The fit was obtained using formula 5.2. The characteristic temperature T_0 determined at elevated temperatures is relatively high.

of InGaN LDs has been used to account for the origin of the phenomenon. The explanation given in Ref. [127] based on simulations of the below–threshold hole distribution and gain for temperatures from 20° C to 80° C for a two-quantum-well laser structure (using LASTIP software) is as follows: at 20° C, hole density in the QW near the p-side of the structure (*p-side* QW) is significantly higher than that QW on the *n-side* because of the poor hole mobility of InGaN. Thus the gain at the *p-side* QW is large and positive while for the other, *n-side* QW, the calculated gain is negative at this temperature (absorption). As temperature increases, the hole density on the *n-side* QW increases due to thermally enhanced hole transport from the *p-side* to the *n-side* QW, which then results in an increase in the gain on the *n-side* QW with increasing temperature. The hole density on the *p-side* QW does not change much with temperature, so the gain on the *p-side* QW decreases with increasing temperature due to the temperature-dependent reduction of material gain. Therefore, these opposite temperature behaviors of the gain in two–QWs could lead to the complicated and unusually stable temperature dependence of the threshold current in InGaN laser devices.
Also, simulation and experimental results for single wide QW InGaN laser structure with respect to thermal stability discussion were reported by Swietlik *et al.* [126]. The results were tentatively explained through the mechanisms of carrier loss decrease with increasing temperature – the electron current overflow

reducing lasers efficiency is enhanced by a ballistic transport of electrons through the active region. Simultaneously the probability of the transport is higher at low temperatures. And thus it would explain the observed anomalous temperature dependency.

Above 50° C the threshold current gradually increases, at 201° C the increment makes double of the initial value. Using equation 5.2 for the more linear part of the obtained results of $I_{th}(T)$ fitting data yielded $T_0 = 238.0 \pm 1.8\,K$, which is a relatively high value in comparison with conventional arsenic lasers. In addition, the slope efficiency of the device does not decrease substantially with increasing temperature. In Fig. 5.8 examples of registered L–I characteristics as a function of temperature are depicted. Significant difference appeared only at 201° C, where the slope efficiency of the L–I curve had dropped by 35%. Owing to the relatively high T_0 value the device showed very good thermal stability in the temperature range under investigation.

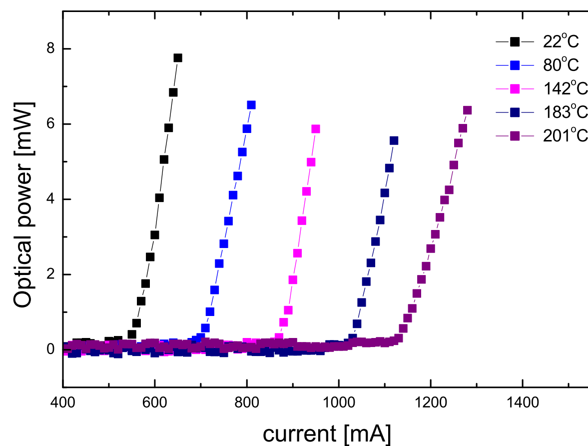

Figure 5.8: Light–current characteristic as a function of laser's ambient temperature. A very nice thermal stability of the efficiency is demonstrated. At 201° C the efficiency decreases by 35%.

5.3 Cavity Ring Down Spectroscopy

Blue laser diodes are conveniently applicable to detection of the lowest concentrations of various atoms and molecules, where the principle of trace matter detection relays on small absorption measurement. Cavity Ring-Down Spectroscopy (CRDS) and its modifications are among the most suitable techniques for such

investigations [129, 130, 131, 132, 133]. Fig. 5.9 illustrates the idea of a CRDS measurement. In essence, the laser pulse is trapped inside the optical resonator of a very high quality (**Q**). When the laser wavelength matches the absorption line of the matter filling the resonator this quality factor **Q** decreases. The absorption coefficient can be then found comparing the quality factors characterizing the empty resonator and the resonator filled with the absorber. We can use pulsed operated lasers as the light sources as well as cw lasers, amplitude modulated. It was already demonstrated that for pulsed lasers the sensitivity of the absorption coefficient determination can reach $10^{-9}\,m^{-1}$ while for cw lasers the measurement of the absorption of $10^{-12}\,m^{-1}$ is possible [134].

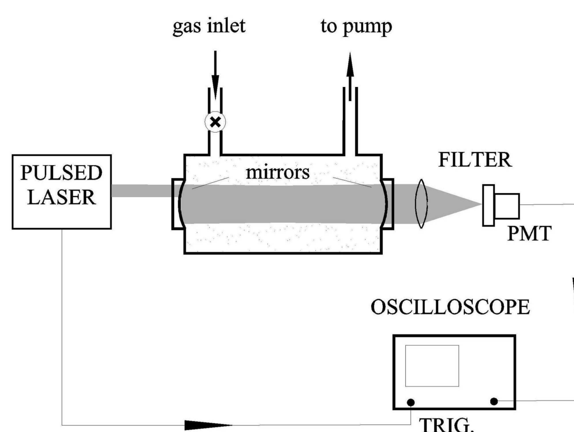

Figure 5.9: Schematic view of typical CRDS experimental setup. Quality factor of the optical resonator can be determined measuring either the decay time of light inside the resonator [129], or the phase shift between input and output light pulses [135], or the intensity of light stored in the cavity [130].

5.3.1 NO_2 detection with pulsed diode lasers

NO_2 occurs in the air due to various anthropogenic processes, industrial activity, fuel burning etc. It is the key factor that characterizes the quality of the atmosphere, therefore is frequently monitored. Nowadays, when the security problems attain more and more significance, sensitive detection of nitrogen dioxide becomes particularly important. NO_x compounds usually appear during decomposition of many military explosives and thus can serve as an indication of the presence of dangerous materials. Currently NO_2 is commonly detected using the

methods based on chemiluminescence [136, 137]. Their sensitivity reaches single ppb. The emission range of blue diodes (approximately 395 - 440 nm) fits well to NO_2 absorption spectrum. Within these wavelengths nitrogen dioxide has $^2A_1 - ^2B_1$ and $^2A_1 - ^2B_2$ absorption bands with a mean cross section of $6 \cdot 10^{-19}\, cm^{-2}$, varying about ±40% (Fig. 5.10). In addition, among common atmospheric gases there is no other compound that absorbs in this spectral range. Therefore pulsed violet and blue diode lasers with application of CRDS techniques (and their modifications) might lead to construction of fully optoelectronic sensor of this compound. First laboratory constructions have been demonstrated already [138, 139, 140, 141, 142]. Fig. 5.11 shows a scheme of a construction of a

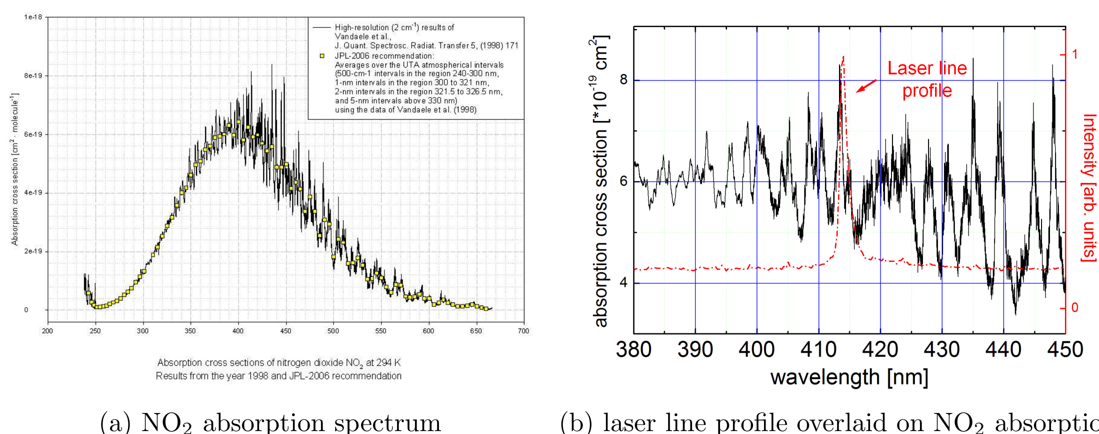

(a) NO_2 absorption spectrum

(b) laser line profile overlaid on NO_2 absorption

Figure 5.10: Absorption cross section of NO_2 [143] (a) the profile, (b) in the spectral range corresponding to violet-blue LDs emission, dashed line shows the emission line profile of the laser that was applied in the experiment.

NO_2 sensor, which was used in the experiment. The optical cavity was formed in a chamber with its two endings closed by high optical density mirrors (Los Gatos Research, nominal reflectivity of 99.995% at 405 nm). The mirror mounting provided precise adjustment of the tilt over the angle of $\pm 3°$ with respect to the cavity axis. The distance between the mirrors was 37 cm and the radii of curvature were 1 m in both cases.
Laser diode emitting around 414 nm was used as a light source. It was pulsed-operated generating pulses of peak power about 200 mW, duration time 100 ns and the repetition rate about 10 kHz. The laser beam illuminated a blazed grating (groove density of 2400 mm^-1). The beam reflected at the 0th diffraction order served as a reference signal, the 1st diffraction order beam passed through

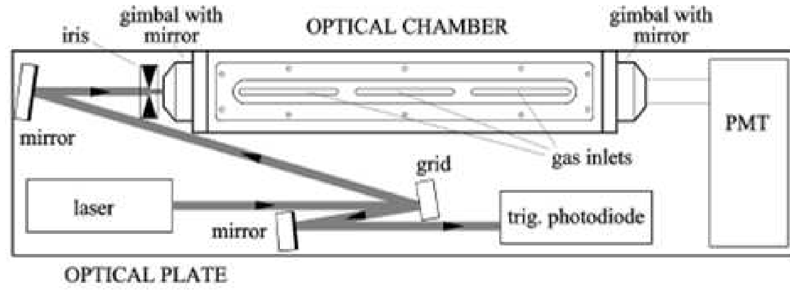

Figure 5.11: Schematic view of NO_2 sensor.

an iris diaphragm and illuminated the cavity. The combined use of the two spectral and spatial filters minimized the background signal of the LD's electro-luminescence. The spectrum of this luminescence is much broader than the width of high reflectivity band of the cavity mirrors and might strongly affect shape of the measured exponential decay signal. Applying the iris diaphragm also helps to avoid the multi-mode excitation of the cavity which may eventually lead to multi-exponential decay of trapped radiation and cannot be interpreted without doubt.

Laser light was injected into the cavity with the *off-axis* approach (see Fig. 5.9), which allows the laser beam to reflect hundreds of times inside the cavity without overlapping [144, 145]. In this way the problem of closely spaced longitudinal cavity resonances, usually present in the on-axis excitation method, was avoided. The off-axis method provides that the frequency spectrum of the cavity is characterized by a dense mode structure with weak and broad longitudinal modes. The cavity couples well to broadband and unstable laser radiation (dynamically changing from pulse-to-pulse) and does not need any additional system of cavity length control or laser frequency tuning. Finally, with this arrangement the back-reflected laser beam by a convex surface of the front mirror does not reach the diode laser and does not disturb its operation.

To determine the cavity **Q** factor, which is necessary for measurements of NO_2 concentration, the radiation trapping time was measured. Then the absorption coefficient was found using the following relation:

$$\alpha = \frac{1}{c}\left(\frac{1}{\tau} - \frac{1}{\tau_0}\right) \tag{5.3}$$

In case of empty resonator, we observed the decay time of $\tau_0 \approx 8\,\mu s$. During the measurement the cavity was supplied with a gas (NO_2 - air) mixture of $50\,ppm$

mixing ratio. The mixture was additionally diluted in pure nitrogen using two gas flow controllers (Beta-Erg) so that the mixing ratio of the gas inside the cavity was precisely admeasured. To ensure homogeneity of the medium in the cavity the gas flow was reduced to $3\,l/min$. The output signal was recorded with a fast 8-bit digital oscilloscope (HP 54520) and a lock-in amplifier.
Fig. 5.12 displays the obtained results, there is a good agreement between the measured absorption coefficients and the corresponding NO_2 concentrations when the absorption cross section of $5 \cdot 10^{-19}\,cm^{-2}$ is assumed. At the emission wavelength of the LD, $\lambda = 414\,nm$, the value of the cross section is $5.5 \cdot 10^{-19}\,cm^{-2}$ (Fig. 5.10). The discrepancy is attributed to both uncertainty of the CRDS technique and the preparation of a gas mixture. Sensitivity of single ppb, which was achieved in presented here measurements, can be further increased with the use of more specialized electronics providing more precise measurements of the radiation decay time.

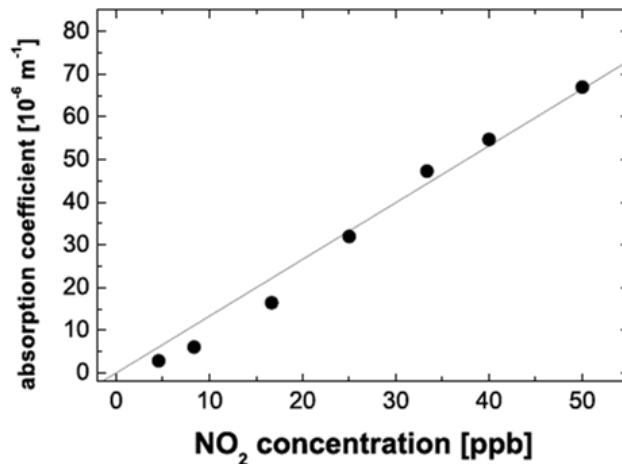

Figure 5.12: Measured absorption coefficient of NO_2 versus the concentration of prepared mixture.

5.3.2 The outlook: cw LDs for atomic spectroscopy

The external cavity configuration can be also used to obtain stable frequency operation of a cw laser diode with fine tuning available by small changes in the driving current. Using a broad-ridge ($7\,\mu m$ stripe) cw-operated (Al,In) GaN LD in Littrow configuration and providing temperature stability of 0.01° C a single narrow line emission was achieved. The LD was operating at $405\,nm$, the output power was $5\,mW$. The result is shown in Fig. 5.13, where measured emission

line using a $1\,GHz$ FRS (Free Spectral Range) Fabry-Perot interferometer is displayed. The output signal from the interferometer was registered by a photodioe and a digital oscilloscope. A diffraction grating of $3600\,lines/mm$ formed the external resonator of a length of $5\,cm$. Stability of generation was better than $100\,MHz$ within the time periods of $30\,min$ without any active feedback system. These results are promising in terms of the applicability of presented here nitride LDs as light sources to atomic spectroscopy at Doppler broadened lines, which usually are characterized by widths of $\sim\ GHz$.

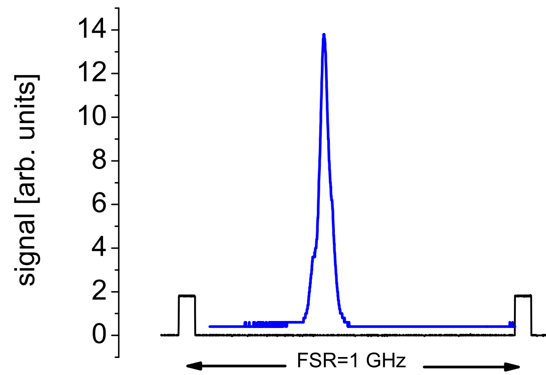

Figure 5.13: Single mode emission of a cw-operated InGaN LD ($\lambda = 405\,nm$. Rectangular line represents Free Spectral Range markers of a Fabry-Perot interferometer ($\Delta\nu = 1\,GHz$).

Chapter 6

SLEDs

In chapter 6 I introduce the concept of a Superluminescent Light Emitting Diode. The structure and fabrication of SLEDs I describe in section 6.1. In section 6.2. results of basic electrical and spectral characterization of these devices are shown, which I measured at room temperature. In the last section, 6.3, results of a detailed study on superluminescence and its temperature dependence are reported. I present experimental data and introduce a simple model in which I explain the character of temperature dependence of superluminescence.

Superluminescent Light Emitting Diodes (SLEDs) are semiconductor devices that emit broadband light by means of electrical current flow. They feature lasers spatial coherence and beam directionality. However, as no optical resonator is introduced, the spectrum is broad and continuous - similar to the emission from LEDs. Due to unique properties of the emitted radiation SLEDs find applications e.g. in biomedical and industrial imaging based on optical coherence tomography (OTC) [146]. The beam directionality results in high efficiency coupling with lens systems or optical fibers enabling SLEDs to find applications in navigation systems that use fiber-optics gyroscopes (FOGs) [147] for precise rotation measurements.

In the past few decades a lot of work has been done to improve the performance of SLEDs as well as to expand the spectral range in which they can operate. Much of the effort was centered around InP and GaAs materials, providing devices which operate in the infrared and red spectral range and cover the wavelengths from 650 to 1300 nm. Recent interest in imaging applications has focused attention on producing blue SLEDs using nitride material system. The first successful demonstration of a blue SLED was reported last year by the group from EPFL (Lausanne) [148]. Feltin *et al.* demonstrated a GaN based SLED operating cw

at room temperature, emitting at 420 nm with the bandwidth of 5 nm in the superluminescence regime.
The subject of the study presented in this part of the dissertation was focused on deeper understanding the superluminescence mechanism and its temperature dependence. The experimental study was performed on InGaN SLED structures that were grown and fabricated at the Institute of High Pressure Physics, Polish Academy of Sciences and its *spin-off* company TopGaN Ltd.

6.1 SLED structure and fabrication

The epitaxial structure of a SLED is identical to an *in-plane* laser structure, discussed in detail in previous chapters, the only difference is in the fabrication of each type of device. Our samples were grown (by MOVPE) on plasmonic bulk GaN substrates with the following epi-layers configuration: a 600 nm Si-doped $Al_{0.08}Ga_{0.92}N$ bottom cladding was deposited on the gallium side of the substrate, followed by a 50 nm Si-doped lower GaN waveguide, 50 nm $In_{0.02}Ga_{0.98}N$ injection layer, three pairs of $In_{0.1}Ga_{0.9}N/In_{0.02}Ga_{0.98}N$: Si (3.5 / 8 nm) quantum wells, 20 nm $Al_{0.2}Ga_{0.8}N - p^+$ electron blocking layer, 80 nm GaN waveguide layer, 330 nm $Al_{0.08}Ga_{0.92}N$: Mg upper cladding layer and a 30 nm GaN: Mg-p^+ subcontact layer.
SLEDs were fabricated in a similar manner to ridge-waveguide oxide-isolated laser devices with chip dimensions of 300 x 700 μm^2. Mesa structures of approximately 3 μm wide by 300 nm height were fabricated using reactive ion etching of the p-type cladding. The most critical issue in the fabrication of a SLED is to avoid an optical feedback and allow only a single pass of the propagating optical mode along the waveguide. One of the methods employed to prevent forming of a standing wave between the cleaved facets is to tilt the ridge at a certain angle with respect to the cleavage plane [149]. In our case the tilt was 5°. SLEDs and laser diodes were processed side-by-side on a wafer to allow for direct comparison between these two types of devices and for that reason no dielectric coatings were applied on the facets of the structures under investigation. A photo of a processed wafer is shown in Fig 6.1.

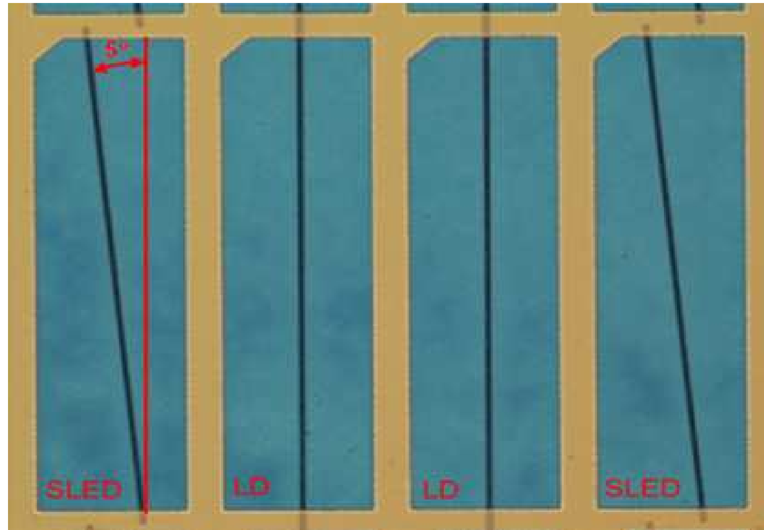

Figure 6.1: A photo of a processed wafer with SLEDs side-by-side with laser diodes.

6.2 Device characterization

To provide best temperature stabilization processed SLEDs were soldered p-side down on diamond heat-spreaders and mounted in a custom copper package. Devices were tested under constant current conditions and the corresponding light-current characteristics and optical spectra were registered. A thermoelectric cooler (TEC) was used to vary the temperature of the copper packaging and a constant flow of dry nitrogen was supplied in order to avoid water vapor condensation. Figure 6.2 shows a comparison between the light-current characteristics of a laser diode and a SLED fabricated on the same wafer, measured at room temperature. An obvious difference is seen in the character of these two curves. SLED $L - I$ characteristic shows an exponential dependence without a sharp threshold. In contrast, the laser diode has a clear threshold around $250\,mA$ and then a typical linear dependence of the optical power. A large difference in the output power, of more than an order of magnitude, between the SLED and LD is observed. This effect is assigned to overheating of the active region, which causes a drop in efficiency and gives rise to a more pronounced temperature sensitivity of SLED devices as comparing to LDs (the latter were reported to have high temperature stability with T_0 parameter well above $200\,K$, see e.g. Swietlik *et al.* [126]).

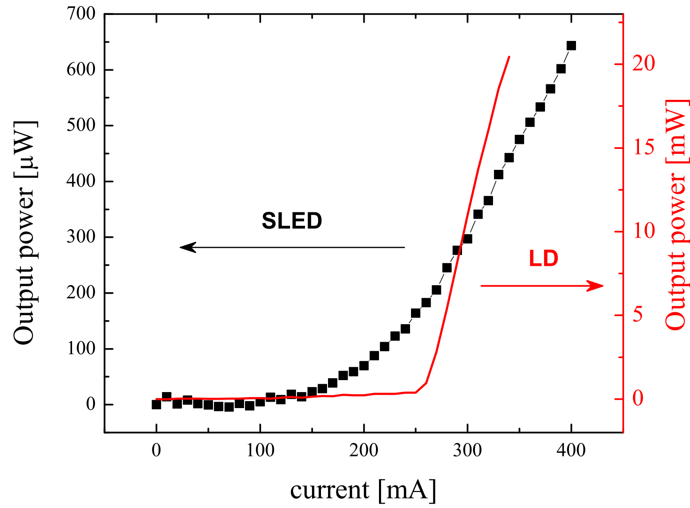

Figure 6.2: Comparison of light-current characteristics of a SLED and a laser diode fabricated on the same wafer.

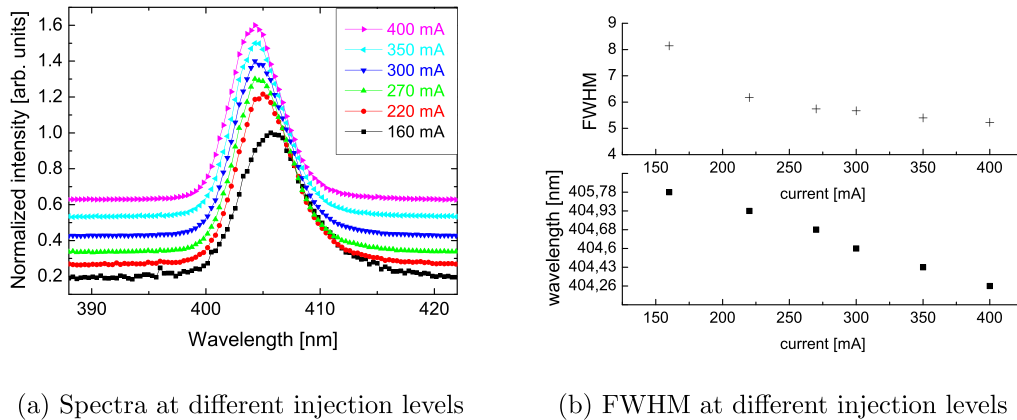

(a) Spectra at different injection levels

(b) FWHM at different injection levels

Figure 6.3: (a) SLED's electroluminescence spectra measured at different injection levels, (b) central emission wavelength at different currents and corresponding FWHM values.

Electroluminescence spectra of a SLED sample measured at room temperature are relatively broad, as depicted in Fig 6.3. The spontaneous emission peak is at 407.78 nm at 160 mA with a full with at half maximum (FWHM) of 8.14 nm. Along with increase of injection current spectra become narrower, at 400 mA FWHM reads 5.23 nm, but the broad and smooth appearance remains unchanged. The character of these curves results from the amplified spontaneous emission (ASE) process and is very different from a typical multi-mode laser emission

spectrum. In order to avoid temperature-induced wavelength shift this measurement was performed under pulsed operation with $50\,ns$ pulse duration and at repetition rate of 10 kHz. The central wavelength of emission, however (as can be seen in Fig 6.3), shifts towards shorter wavelengths with increasing drive current. This effect is a result of a known problem of the strong built-in piezoelectric fields present in polar nitride-based structures and lead to the quantum confined Stark effect (QSCE). At higher pumping levels, more electrons fill-in the conduction band and screen the polarization charges at the interfaces of a quantum well. A blue-shift of the emission wavelength is observed.

6.3 Temperature dependence of superluminescence

Different nature of SLEDs emission, as compared to laser diodes, originates from the amplification process of only spontaneous emission. Superluminescence occurs when the spontaneously generated photons are replicated as they travel along the waveguide. The onset of the superluminescence is directly correlated with the positive modal gain, which usually means high pumping levels and hence makes these structures very sensitive to temperature. In this section a simple model to describe this rather large temperature dependence of gain, considered for a 3D (bulk) system, is presented.

Using a simple approximation, the emitted power due to the superluminescence, if we are far away from the gain saturation regime, can be expressed by [148, 150]

$$P(L) = \frac{A}{\Gamma g - \alpha}\,[e^{(\Gamma g - \alpha)L} - 1], \tag{6.1}$$

where A is a parameter proportional to the spontaneous emission, g is the material gain and L is the cavity length. Γ is the confinement factor and α stands for the optical losses in the waveguide. Parameters A, g, and α depend on the current density J and the wavelength λ.

If we look in more detail how the gain is expressed we find [18] that the material gain is composed of the following two factors:

$$g = g_m(E_{21})\,(f_2 - f_1), \tag{6.2}$$

where $g_m(E_{21})$ is the material property given by the matrix element and the density of available state pairs corresponding to the transition energy E_{21}. The difference $(f_2 - f_1)$ is the Fermi factor, dependent on the injection level and f_2 and f_1 are occupation probabilities described by the Fermi statistics in the conduction and valence bands, respectively. For a given temperature $T > 0$, at a given carrier density N this Fermi factor shapes the gain curve as the transition energy E_{21} increases in a way depicted schematically in Fig 6.4.

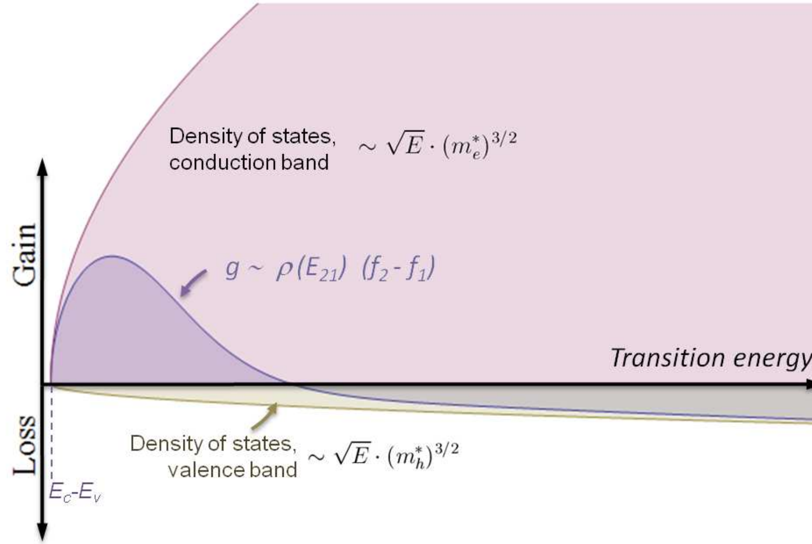

Figure 6.4: Schematic illustration of gain distribution as a function of transition energy E_{21} for a given carrier density and temperature $T > 0$. Density of states is approximated by a square root dependence on energy (bulk system, parabolic bands with curvatures defined by the carriers' effective masses m_e^* and m_h^*.), $E_c - E_v$ is the distance between the bottom of the conduction band and the top of the valence band, respectively.

In order to find what is the influence of the pumping level (at a given temperature T) on gain distribution one needs to calculate the position of the *quasi-Fermi* level in the conduction band, E_{F_c}. Using a simple, parabolic band approximation the curvature of the conduction band is much larger than the valence band curvature and hence the *quasi-Fermi* level in the latter (E_{F_v}) does not move significantly within the current injection levels corresponding to normal operating conditions of the device and can be assumed to be roughly constant. E_{F_c} is calculated using the inverse Fermi-Dirac integral with Nilson's global approximation (see e.g. [18] for reference).

In Fig. 6.5 simulation results demonstrating material gain dependence on the carrier density N and a well-known logarithmic character of $g_{max}(N)$ are displayed.

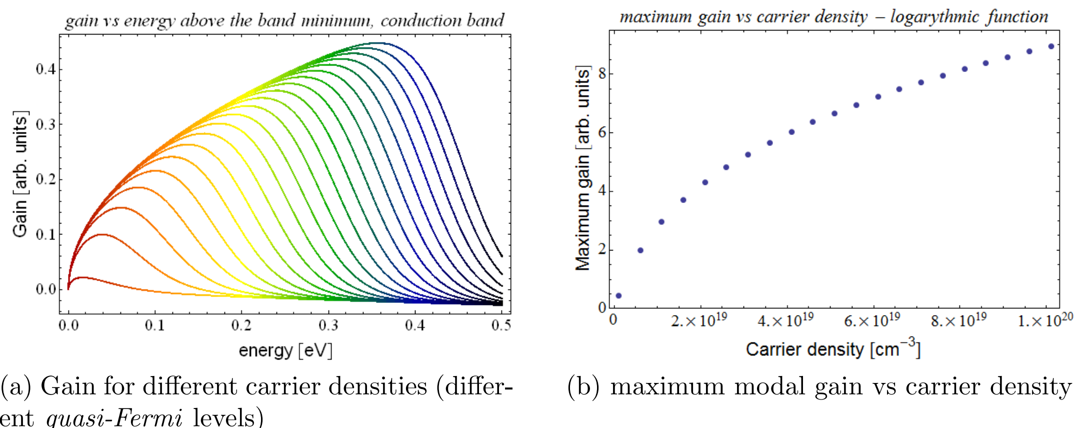

(a) Gain for different carrier densities (different *quasi-Fermi* levels)

(b) maximum modal gain vs carrier density

Figure 6.5: Carrier density dependence of gain for given temperature $T = 295\,\mathrm{K}$, calculated from the Fermi integral (see e.g. [18] for reference).

The above mentioned considerations lead to the following conclusions:

- the population of carriers in the valence band (f_1) does not change very much with temperature, nor does it move substantially when pumped (as long as we do not approach gain saturation levels), mainly due to the low curvature of the band,

- f_2, on the other hand, is very sensitive to the carrier injection level as well as to temperature changes. In consequence the peak gain will follow f_2, and hence the emission wavelength blueshifts toward higher energies with increased injection level. Similarly f_2 is very sensitive to temperature changes – the dependence of the peak gain versus carrier density calculated at different temperatures is shown in Fig. 6.6, below.

The output power at a SLED's facet is found by calculating the amplification of the optical mode as it propagates over a distance L during a single pass along the waveguide. Analyzing again Eq. 6.1 we see two factors that shape the output signal. The first is connected with the probability of spontaneous emission, the second one describes amplification. We can rewrite Eq. 6.1 in the following form:

$$P(L) \propto B\ exp\,[A'_{spont} \cdot (\Gamma g - \alpha)L]. \quad (6.3)$$

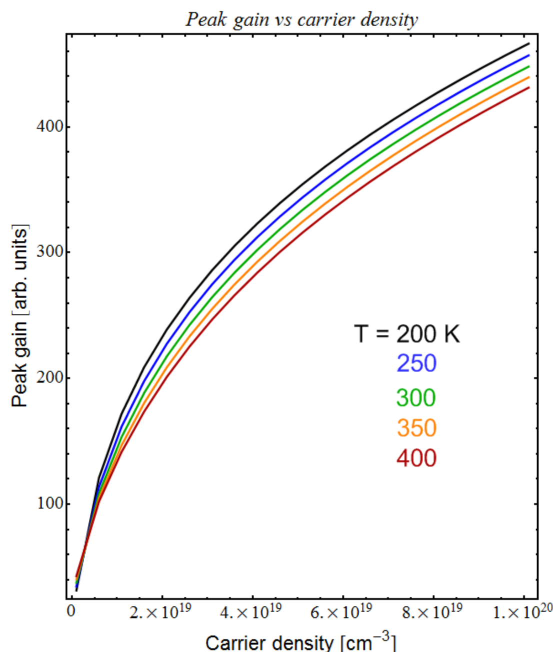

Figure 6.6: Peak gain dependence on the carrier density calculated at different temperatures.

where B is a constant and A'_{spont}, g, and α depend on the current density J, the wavelength λ and on temperature. For the case of an *in-plane* waveguided structure, the modal gain needs to be considered, which is the material gain g adjusted by the optical confinement factor Γ, as we must account for the very small overlap between the optical mode and the active region.

Results of measurements and simulations carried out at temperatures of 295, 283, 272 and 263 K are presented in Fig. 6.7 and 6.8. In order to avoid junction heating under cw operation, the measurements were carried out at pulsed regime. Figure 6.7 shows measured spontaneous emission signals as a function of temperature, registered at different current pumping levels. For low drive currents of up to 10 mA the spontaneous emission probability is almost constant within this temperature range (black curve in Fig. 6.7). With increasing current this temperature dependence becomes stronger, which indicates that we must take into account amplification of the spontaneous signal. If we assumed that the probability is constant and evaluate the output signal considering only the material gain dependence on temperature the result is different from what was measured.

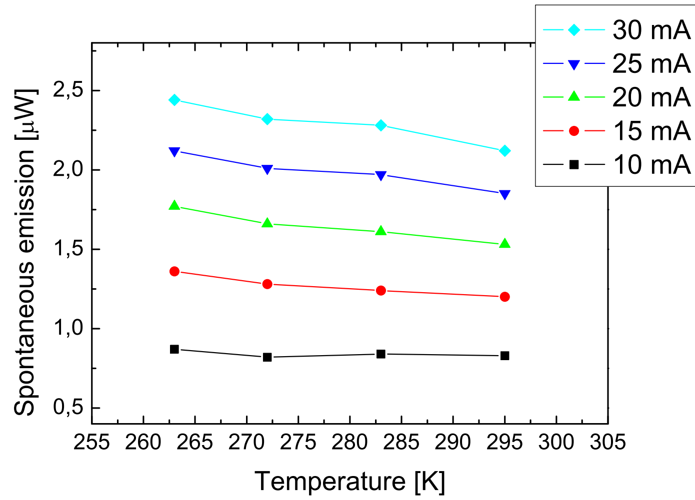

Figure 6.7: Spontaneous emission vs temperature measured at different drive currents.

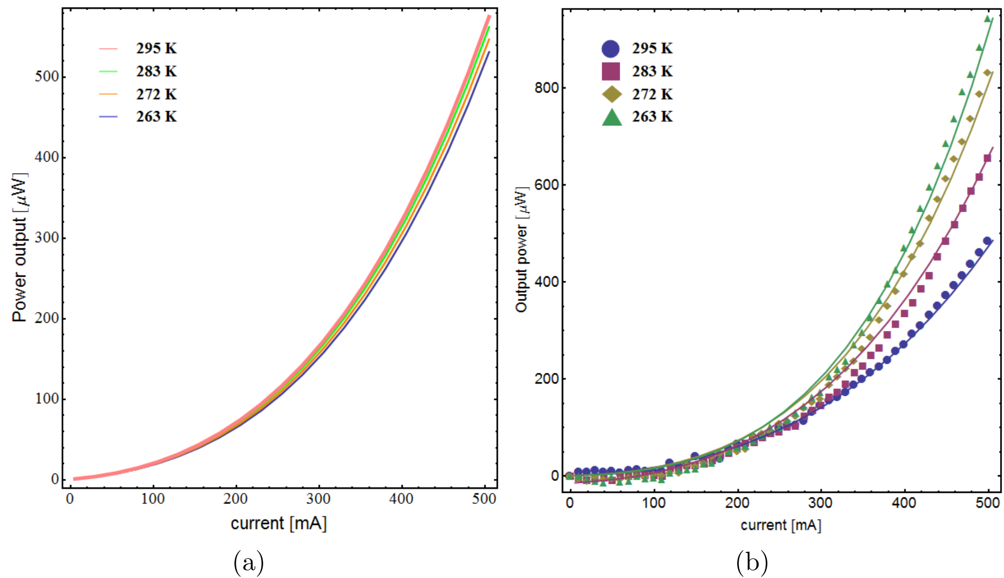

(a) (b)

Figure 6.8: (a) Calculated output power vs injection current including only gain dependence on temperature and (b) measured SLED output power (symbols) and calculated signal (solid line) taking into account the spontaneous emission temperature dependence

Figure 6.8 a shows the result of the calculated output signal, taking into account only the peak gain dependence on temperature and carrier density, without the spontaneous factor. As can be seen in this plot, the calculated power does not change significantly with temperature, contrary to experimental observations.

Figure 6.8 b plots experimental data of SLED's optical output power versus drive current (symbols in the graph), measured at different temperatures from 263 to 295 K. The strong dependence of the output signal as a function of temperature can be seen in this plot, with almost a factor of two in the decrease in power for a temperature increase of 30 K. If we include the temperature dependent spontaneous emission factor A'_{spont}, the calculation agrees very well with the experimental data.

The results obtained from this simple model indicate that the strong temperature dependence of a SLED output power is related to the spontaneous emission factor A'_{spont} in ASE signal and that the temperature dependence of gain is of secondary importance. In consequence, reduction of nonradiative recombination is crucial for stable SLED operation and tight temperature control of all the elements of the device is of great importance.

Chapter 7

Nitride Laser Diode Arrays

Chapter 7 describes results of experimental study on integrated mini laser arrays. In section 7.1 I start with description of the construction of the mini arrays fabricated at TopGaN Ltd., next I report on their characterization. Basic characteristics providing information on electrical and spectral properties of mini-arrays are followed by the near-field and far-field measurements, which I carried out both at the Institute of High Pressure Physics and during my visit to Regensburg University. The measurements revealed that the devices possessed a weak transversal confinement of the optical mode, which was responsible for coupling between the emitters within a single array. Finally, in section 7.2 I present the new generation of arrays fabricated at TopGaN Ltd., which incorporated the new epitaxial design with improved optical confinement. For these structures I did not observe any coupling between emitters on an array chip. Fabrication of arrays with improved design resulted in 2.5 W of optical output power from a three stripe mini laser array.

One of the required features of nitride-based laser diodes is the possibility to obtain high output powers, which is essential from the point of view of many applications, e.g. RGB displays, lithography or high speed printing. Multi-emitter structures such as laser arrays are the most straightforward solution for obtaining higher optical power from semiconductor optoelectronic devices. In addition, the possibility of a multi-pixel operation in case of individually addressable arrays makes them particularly interesting for printing applications [151]. These array systems, based on conventional arsenic materials, are well-known devices that have been developed and improved for almost four decades [152]. In case of gallium nitride-based structures there are only few reports on their fabrication,

an interesting example was published by Goto *et al* [153] on demonstration of a 44 stripes array producing up to 4.2 W of optical output power in the violet wavelength range. The research presented throughout this chapter was focused on the optical properties of a relatively simple system of closely-spaced, three-emitter violet-blue multi-quantum-well (MQW) InGaN/GaN laser mini-array. All structures were designed and fabricated at the Institute of High Pressure Physics, Polish Academy of Sciences and its *spin-off* company, TopGaN.

7.1 Mini-array structure - first constructions

In order to construct this type of device two main tasks need to be accomplished. The first one is related to the necessity of having large dislocation-free areas on the GaN substrate. The second one is related to the proper thermal managing of heavily loaded devices. The idea of a three-emitter device is illustrated in Fig. 7.1, below.

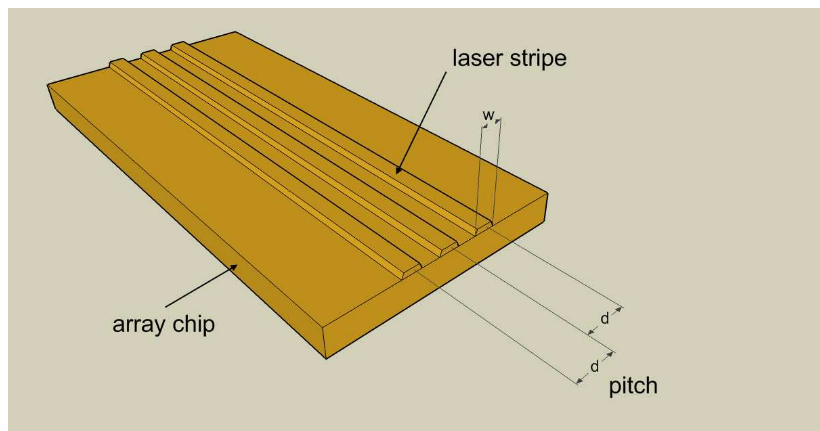

Figure 7.1: Schematic view of the mini array geometry: w - laser stripe width, d - pitch.

Similar to previously described case of laser diodes, the epitaxial structure was fabricated using MOVPE vertical flow reactor on the high-pressure grown gallium nitride substrate [31]. The initial density of dislocation in the substrate material was below 10^2 cm^{-2}. The active region consisted of three, 3.5 nm-thick, undoped $In_{0.09}Ga_{0.91}N$ quantum wells separated by $8-15\,nm$, silicon-doped $In_{0.02}Ga_{0.98}N$ barriers. The electron blocking layer (EBL) was formed by a 200 Å-thick, Mg-doped $Al_{0.2}Ga_{0.8}N$ layer. The $Al_{0.08}Ga_{0.92}N$ cladding layers (0.35 and 0.55 μm for

the upper and lower layer, respectively) sandwiched 0.1 μm-thick GaN waveguides. The mini arrays were processed as oxide-isolated structures with the mesa etched by ICP RIE, down to the middle of the upper AlGaN cladding layer. The resonator length was 500 μm. A photo of processed mini-arrays is shown in Fig. 7.2. To study the influence of the stripe width w and the spacing between the stripes d, laser arrays were fabricated in different configurations. Detailed comparison of the performance of three types of structures A (stripe width: 3 μm, pitch: 40 μm), B (stripe width: 7 μm, pitch: 40 μm) and C (stripe width: 7 μm, pitch: 20 μm) will be presented in this section.
The final density of dislocations for these structures, as measured by selective ion etching, was between $5 \cdot 10^4\, cm^{-2}$ and $1 \cdot 10^5\, cm^{-2}$. The chips of the dimensions of 300 x 500 μm were mounted p-side down on a diamond submount. The individual stripes were electrically connected in parallel. Laser arrays were operated at constant current conditions and at stabilized temperature of 20 °C.

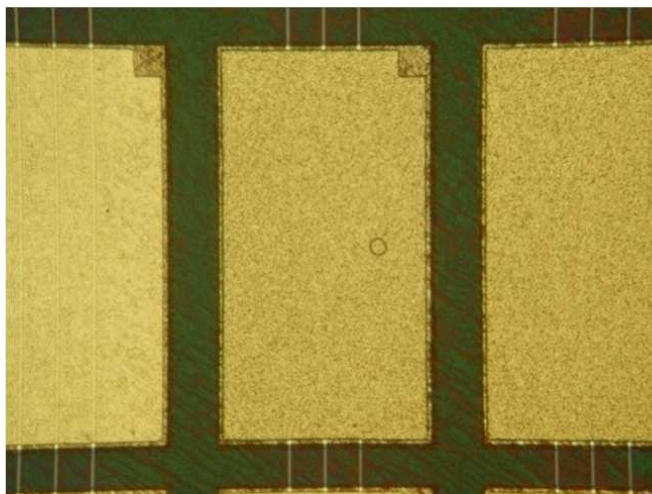

Figure 7.2: A photo of a processed mini-array (old-generation structures).

7.1.1 Characterization

Electrical and spectral parameters

Starting from basic characterization, light-current characteristics and spectral measurements were performed, Fig. 7.3 shows the results obtained for *structure A*. The distinctive feature of the differential slope efficiencies, $\eta = 0.7\, W/A$, was that

they were at least as good or better than typical value for single stripe devices fabricated with the same epitaxial design [83]. This observation indicates that all three stripes participate in lasing, otherwise the slope efficiency should be proportionally lower. The obtained output powers of around 250 mW (cw) were quite satisfactory, even though the kinks exposed in the $L - I$ curve indicated the need for optimizing thermal management of the structure. Unexpected and

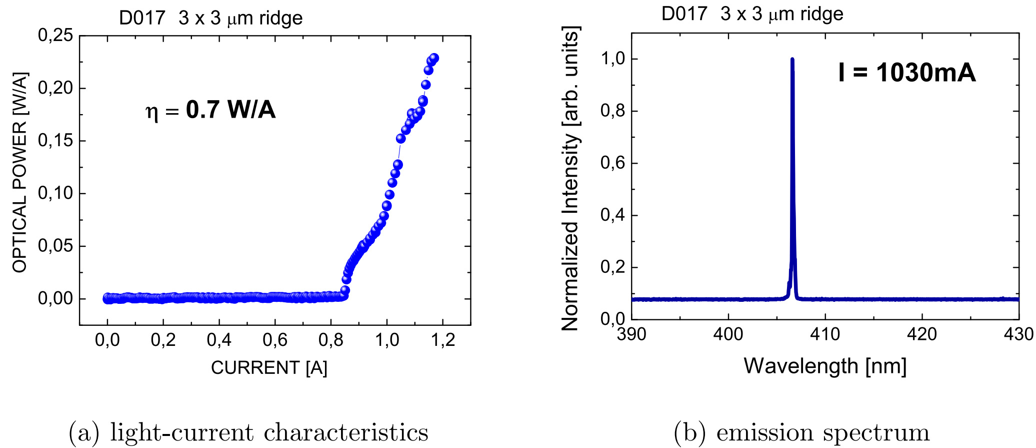

(a) light-current characteristics (b) emission spectrum

Figure 7.3: (a) Light-current characteristics and (b) emission spectrum of *structure A*.

most surprising feature of the emission from this device at lasing condition was its very narrow (on the order of 1.4 Å) single spectral line, obviously not showing typical lateral modes (see Fig. 7.3b). Spectra of the emitted light were analyzed by Acton Spectrometer (500 mm focal length) equipped with a CCD detector. Most of the experimental data show that in order to suppress the lateral modes (in case of a single-stripe device) it is necessary to use very narrow stripe width - below 2 μm [92, 98]. Longitudinal modes are not visible in the measurement because of the insufficient spectrometer's resolution. This observation of a single mode emission is even more surprising in the case of a multi-stripe device like the discussed here mini-array. In order to elucidate the character of the emitted laser mode, measurements of the far-field patterns were performed.

Far-field patterns

The far field pattern measurements were carried out by direct projection (without using any collimating optics) on an active matrix of a CCD camera (640 x 480

pixels array, Duma Optronics Ltd.) The images were registered using camera's software, SpotOnCCD. Fig. 7.4a shows the far field pattern of *structure A* observed in case of the emitting mini–array below its lasing threshold. It was found that at lasing threshold the far field pattern changed from "normal" behavior (three maxima) into a single common mode, centered at the middle stripe. Such pattern was observed for all measured devices. This phenomenon is explained by assuming that a large optical mode leakage of the optical field occurs in each stripe of the system and leads to the coupling of emission through the evanescent waves. This type of behavior was observed in the past for red and infrared laser diode arrays [154, 155]. Further research on laser structures confirmed that in these structures the problem of weak transversal confinement of the mode was pronounced and a strong leakage of the optical field into the substrate was observed, as it was discussed in detail in chapter 4. Another confirmation of the diagnosis can be directly deduced from intensity distribution in the far field pattern shown in Fig 7.4 which exhibits the shape of a higher (not fundamental) transversal mode with side lobes away from the center.

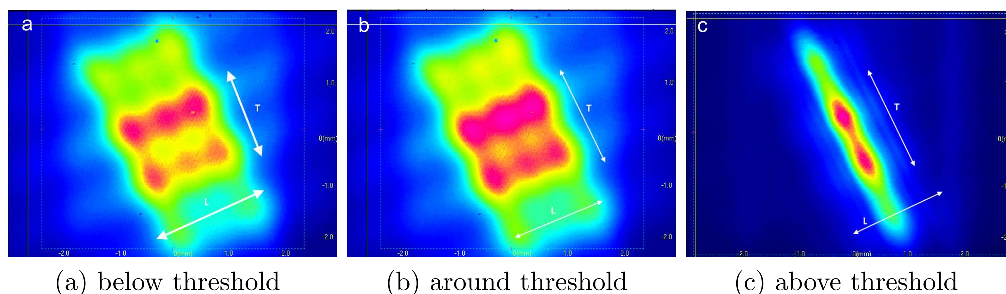

(a) below threshold (b) around threshold (c) above threshold

Figure 7.4: Far field patterns of *structure A* operating: a) below threshold, b) around threshold, c) above threshold (the middle stripe emitting), L - lateral direction, T - transversal direction.

In addition, at lower input currents (below threshold) formation of the mode peaked at two outer stripes was observed. This evolution of the array mode may be, apart from the leakage, simultaneously influenced by temperature induced modification of the refractive index. Other explanation is attributed to packaging-induced as well as temperature-induced stress in the structure resulting in nonuniform current spreading through the top contact layer.

For structures *B* and *C* first quick characterization measurements showed similar far-field patterns, with comparable electrical characteristics of the mini-array.

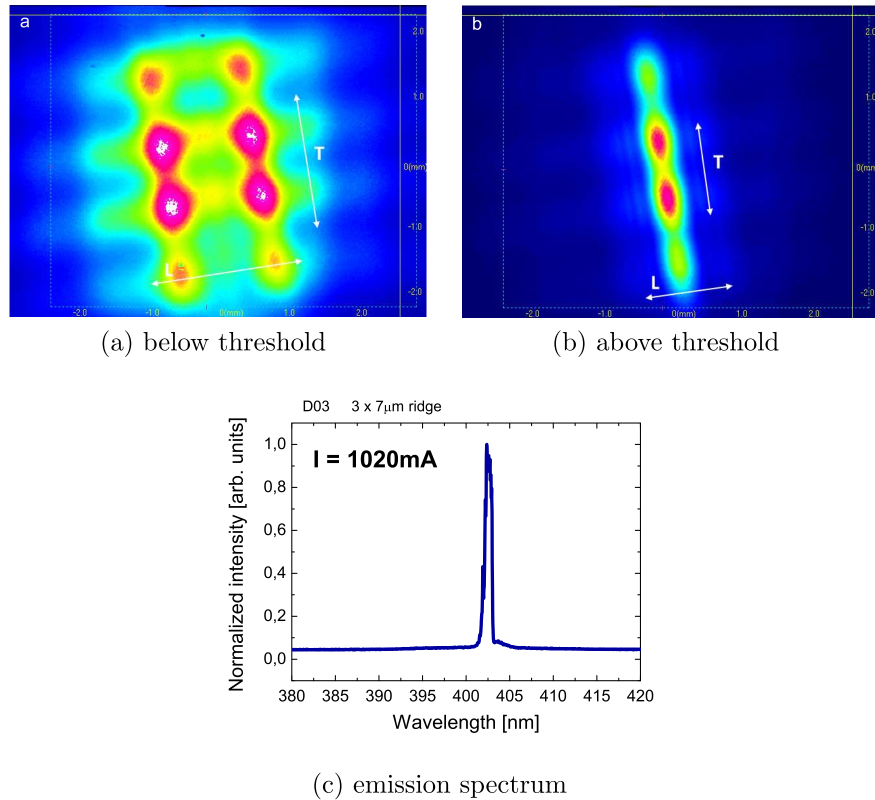

(a) below threshold

(b) above threshold

(c) emission spectrum

Figure 7.5: Far field patterns of *structure B* operating: a) under threshold, b) around threshold. L - lateral direction, T - transversal direction. (c) Emission spectra of *structure B* at lasing.

The main difference above threshold, in comparison with the case of previously grown *structures A*, was a spectrally multimode emission (see Fig. 7.5c) very much alike to that observed for the typical broad area single stripe device. For *structure B*, in the far field pattern below threshold, depending on the current a stronger emission of light in the outer stripes of the structure was observed.

Near-field measurements

Near-field measurements performed on mini-arrays, similar to previously described case of laser diodes, confirmed the weak optical confinement of the waveguide modes. An imaging setup utilizing *Gaussian telescope* (see Fig. 4.7 for reference) with magnification of 35 was used to register the near-field patterns.
In case of 7 microns wide ridge structures the most interesting sample was the one of structure C, where coupling of the optical mode was most pronounced.

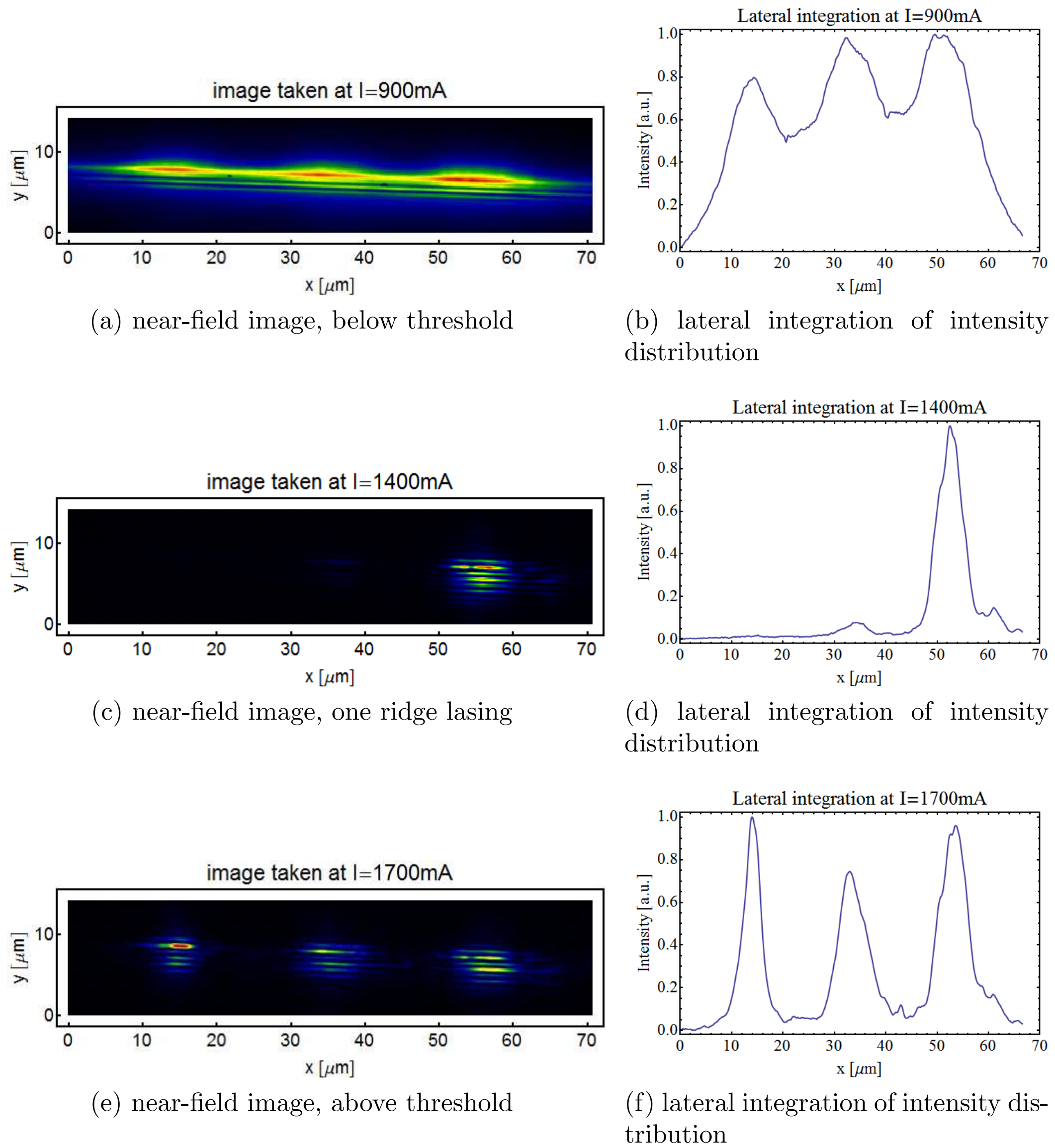

(a) near-field image, below threshold

(b) lateral integration of intensity distribution

(c) near-field image, one ridge lasing

(d) lateral integration of intensity distribution

(e) near-field image, above threshold

(f) lateral integration of intensity distribution

Figure 7.6: Near-field intensity distribution and its lateral integration: below and above lasing threshold, measurements for *structure C* with 7 μm wide ridges spaced by 20 μm.

Fig. 7.6 shows images of the near-field intensity distribution and its lateral integration at currents below and above lasing threshold. Below threshold (a) and (b) the optical field spreads along lateral direction in the whole area of the ridges and also outside them, therefore the lateral integration results in a broad intensity profile with three peaks corresponding to individual ridges. Images taken at 1400 mA, (c) and (d), show that only one of the ridges is lasing, which is tentatively attributed to the already mentioned temperature-induced and also

packaging-induced stress in the structure causing a nonuniform current spreading through the top contact layer. Figures (d) and (e) show results obtained at a current level of 1700 mA, well above threshold with all three ridges participating in lasing. The lateral distribution of the optical field observed in the near-field plane is more discrete above threshold, but the pattern in transversal direction is strongly modulated by the pronounced mode leakage and the presence of substrate modes. The latter effect is also the reason for high current densities at threshold of lasing action.

7.1.2 Optical coupling between emitters

To have a closer look into the optical behavior of the array system, in particular to address issues of optical coupling between the laser stripes within the mini-array, measurements of the beam propagation were performed. Using the experimental setup employing a Gaussian telescope (previously described in detail in chapter 4) with magnification of 18, the beam pattern was registered by taking images along the beam path from the near-field plane to the far-field up to a distance of several centimeters. An example of such propagation profile, measured for sample LD4551 d012 is shown in Fig. 7.7. The evidence of a coherent interaction between the stripes can be seen in the registered profile from the way in which these three beams overlap, particularly that a strong bent of the trace on the right-hand side towards the center occurs. Assuming that in the near-filed plane the beam profile is described by a superposition of Gaussian modes (given by a complex field), with amplitudes and width of filaments as fitting parameters to the measurement, reconstruction of the beam trace can be performed calculating a superposition of filaments (Gaussian modes) as they propagate along a distance z. Depending on the case of a coherent or incoherent superposition, using phase as a fitting parameter to the propagation, different intensity distribution patterns are obtained. A comparison between Fig. 7.7 (measurement) and Fig. 7.8 (calculation, coherent superposition of filaments) confirms that in case of the presented sample these beams are coherently coupled.

Another evidence of coherent coupling between these emitters was found from spectral measurements in the near-field plane. Fig. 7.9 shows a contour plot of the near-field intensity distribution and a corresponding lateral, spectrally resolved characteristics of the near-field profile measured for the studied sample.

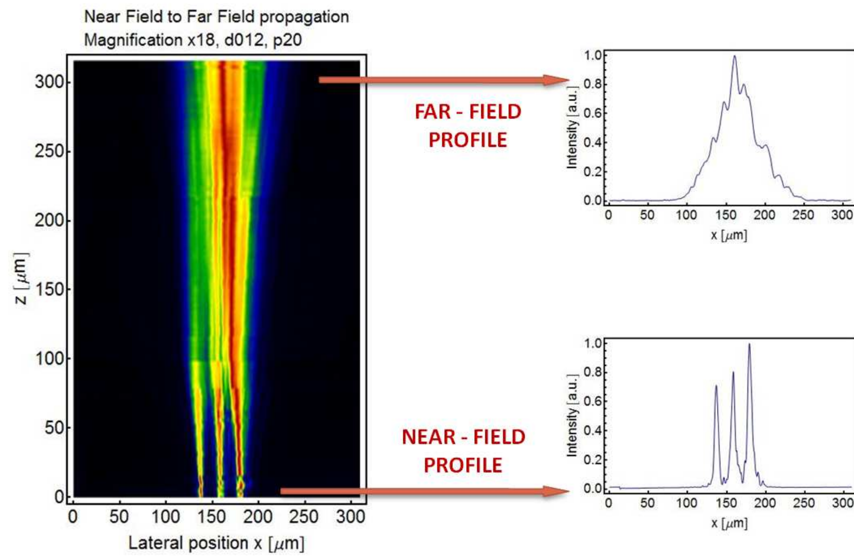

Figure 7.7: Propagation trace of the output beam from a three stripe laser array. Sample LD4551 d012, the width of individual ridges was $7\,\mu m$, the pitch was $20\,\mu m$.

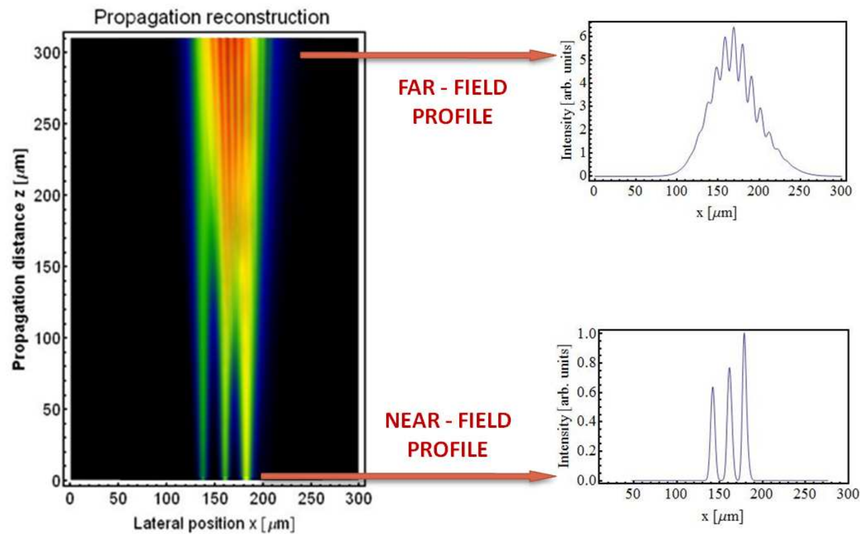

Figure 7.8: Reconstruction of a propagation trace of the optical field from a 3-stripe laser array. Field distribution at the input to simulations is fitted to the measured near-field profile. The obtained pattern is a result of coherent superposition of filaments.

The measurement was carried out by scanning the near-field plane with a single-mode fiber used in combination with a high resolution spectrometer (res. of about 0.005 nm), equipped with a CCD camera as a detector. The laser array was operating cw at a driving current $I = 1660\,mA$, in order to provide good temperature stability a specially designed packaging was combined with the proper cooling system. Similarly to all other measurements one of the ridges was emitting with stronger intensity and for that mode a pattern of combined two components (one dominating and the other weak) was observed. The other two ridges emitting weaker signals show a perfect phase matching, which means that these beams are coherently coupled. For the strongest ridge a small shift in the spectral signal between this and the other two modes was present (Fig. 7.9b). The effect can be explained by a possible change in temperature distribution during a relatively long time of scanning.

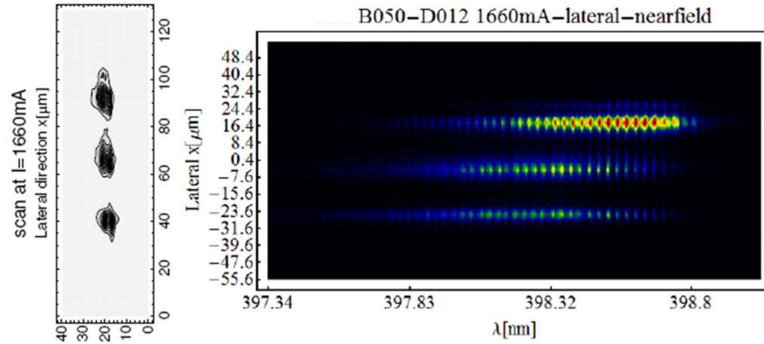

(a) Laterally resolved spectra of an array, *sample C* (LD4551 series)

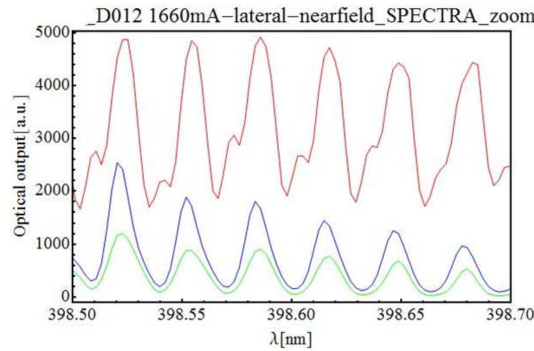

(b) section of the spectra showing almost matching modes

Figure 7.9: Near-field image and its laterally resolved spectral characteristics, above threshold at $I = 1660\,mA$, *structure C* (LD4551 series), (b) section of the spectra revealing the nearly phase-matched longitudinal modes.

7.2 New generation arrays

The new generation of mini arrays incorporated an optimized structure design with better transversal waveguiding, which was realized by a plasmonic substrate or by using thick layers of conventional AlGaN bottom cladding. Additionally new devices were fabricated applying TopGaN's improved processing procedures, in particular newly design photolithographic masks. A photograph of a processed wafer with state-of-the-art devices is shown in Fig. 7.10. Laser arrays were fabricated simultaneously with standard LDs to have the possibility of direct reference for characterization. The chip dimensions were of $300\,x\,700\,\mu m$ with three or five laser stripes per array. The available ridge widths were 3, 5, 7 and $10\,\mu m$, the distance between the stripes was 12, 20, 40 and $80\,\mu m$. The applied dielectric coatings were designed to yield 20% reflectivity for the output facet and 90% for the back mirror.

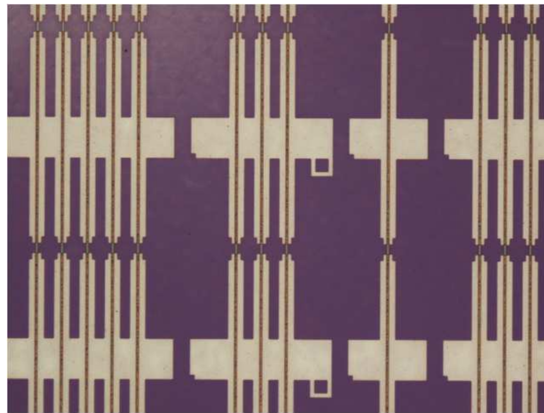

Figure 7.10: New generation arrays fabricated simultaneously with standard LDs. A photo of a processed wafer showing an LD and two arrays with 3 and 5 laser stripes per chip.

The goal in fabricating devices with different ridge widths and pitch was to study the influence of these parameters on the overall performance of devices, especially to find out if an optical coupling between the emitters occurs. A series of measurements of the near-field patterns was performed using a CCD camera combined with a Gaussian telescope, magnification of 45 was applied. Spectra were registered by placing an optical fiber in the plane of the near-field image, separately for each of the ridge. The fiber was connected with an Ocean Optics HR4000 spectrometer, which allowed to take measurements with spectral reso-

lution of 0.02 nm. Contrary to the previously studied samples, for all samples under investigation from the new generation arrays, independent emission from each stripe was observed. Fig. 7.11 shows results obtained for sample D63 (series LD5090), i.e. a mini-array with pitch of 12 μm and the ridge-width of 3 μm. In the near-field a nicely confined optical mode was observed (small intensity shadows visible between the ridges in Fig. 7.11a are some reflections originating from a filter plate), confirmed by lateral integrated profile. Registered spectra showed independent lasing from each stripe with relatively broad multimode emission line (FWHM of about 2 nm), centered around 405 nm (Fig. 7.11b). It was clear that the previously observed optical coupling between emitters originated from the leakage of the weakly confined mode.

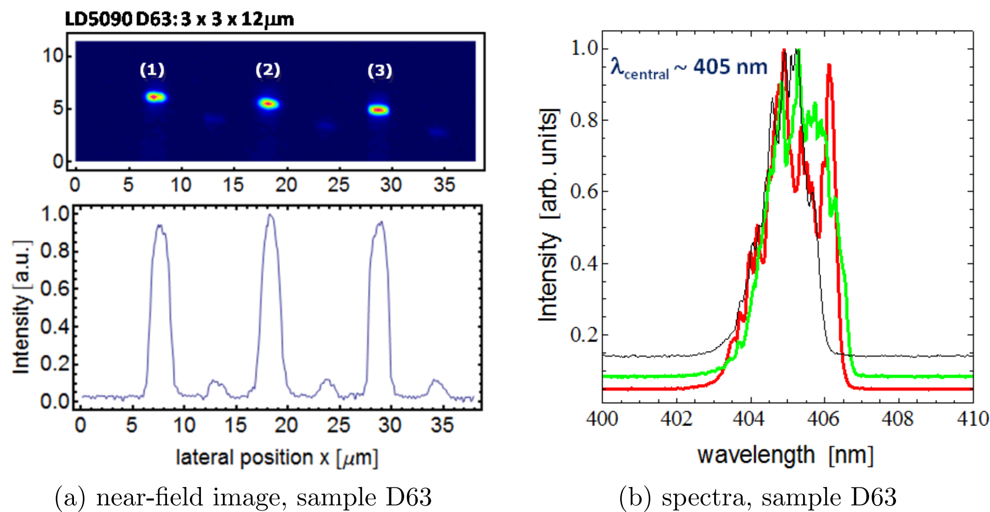

(a) near-field image, sample D63

(b) spectra, sample D63

Figure 7.11: Results of optical characterization of a mini array D63 from series LD5090: (a) near-field image taken with the magnification of 45 and below the corresponding lateral profile - integrated signal from the CCD camera, (b) spectra measured separately for each of the ridge – red (1), green (2) and black (3).

The best results in terms of high output powers and overall characteristics was obtained for structures grown on bulk ammonothermal GaN crystals (supplied by Ammono Ltd.). Fig.7.12 shows current-output power ($L - I$), current-voltage ($I - V$) and spectral characteristics for a three-emitters mini array of 10 μm wide ridges spaced by a distance of 80 μm. This structure was grown using a conventional, thick (2 μm) $Al_{0.05}Ga_{0.95}N$ bottom cladding. The device was operating cw at room temperature, stripes were addressed in parallel. The threshold cur-

rent was around $1\,A$, operating voltage between $7-8\,V$ and the slope efficiency (dP/dI) was $1.1\,W/A$ with a slight bending of the curve due to thermal effect at higher driving currents. The obtained optical output power reached $2.5\,W$ at a wavelength of $408\,nm$.

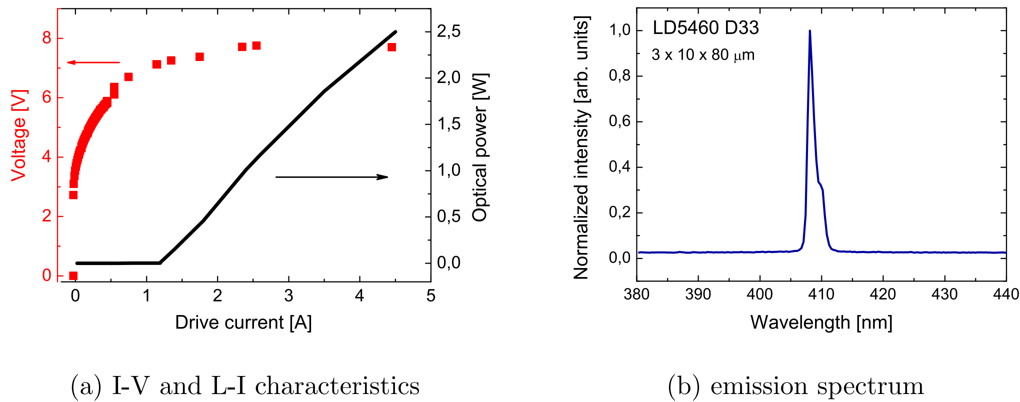

(a) I-V and L-I characteristics

(b) emission spectrum

Figure 7.12: High output power, new generation mini laser array: (a) current-voltage (red) and current-optical output power (black) characteristics of a sample D33 from series LD5460, i.e. a three-stripe array with ridge width of $10\,\mu$m and pitch of $80\,\mu$m, (b) emission spectrum is centered around 408 nm.

Many research and efforts put into optimization of the epistructure, the use of good quality substrates but also the complex and demanding processing procedures proved invaluable in achieving an excellent quality, high power nitride-laser-based devices.

Chapter 8

Conclusions

Presented dissertation was devoted to the research on optical properties of integrated systems based on GaN laser diodes. The progress in design and fabrication of nitride LDs has brought these devices to maturity. Based on this experience, constructions of more complex systems started to be in reach, greatly expanding the range of possible applications. All devices subject to my study were entirely fabricated at the Institute of High Pressure Physics Polish Academy of Sciences and its *spin-off* company TopGaN Ltd., which hold the requisite facility and know-how of manufacturing high-tech nitride-based instruments.

In the course of my research I started to work with ridge-type waveguide nitride laser diodes. A detailed characterization of these devices and study upon their construction allowed to identify the problem of weak transversal confinement of the optical mode. This mode leakage resulted in the presence of substrate modes deteriorating performance of structures with our old epi-design. Particularly important were the near-field measurements, which gave a direct insight into the optical field distribution on the laser facet and provided an excellent tool for evaluating structure design. The system for near-field and far-field measurements also made it possible to carry out the systematic characterization of InGaN laser mini-arrays and a detailed analysis of optical coupling between integrated emitters.

Fabrication of blue Superluminescent Light Emitting Diodes was reported with detailed analysis on their temperature characteristics. SLEDs are particularly important devices due to their applications in Optical Coherence Tomography (OCT). Other important usage is connected with SLED-based gyroscopes. Due to the unique properties of a SLED emission (broadband spectrum without speckles,

spatial beam coherence) there is a great interest in their application to RGB displays.
Part of my research was devoted to adapting nitride LDs to spectroscopic applications.

The main results of this research can be summarized in the following:

- PLASMONIC CLADDINGS
  A novel idea of waveguide construction in nitrides was presented. Using highly doped GaN layer (which show plasmonic properties due to high free electron concentrations) in the construction of bottom cladding of the laser structure, we were able to eliminate the problem of the optical mode leakage into the substrate. Although the concept is known from the construction of quantum cascade lasers, the main difference is that we work relatively far away from the plasma-edge frequency. This specific case does not introduce substantial optical losses to the system. Simultaneously it provides sufficient refractive index contrast to obtain required optical confinement. This approach greatly facilitates waveguide design for InGaN laser diodes operating in longer wavelength range (450 - 530 nm), which are essential for development of laser RGB emitters.

  A patent application was filed on this subject.

- NITRIDE LDS FOR SPECTROSCOPIC APPLICATIONS
  A comprehensive study on tunability of nitride laser diodes was performed in terms of their applicability to spectroscopic measurements. Using temperature tuning and external cavity tuning these devices can be successfully adapted to molecular and atomic spectroscopy requirements. By means of external cavity I obtained the tuning range of $5.5\,nm$, temperature tuning resulted in wavelength shift range of $16\,nm$ at $\Delta T = 200\,K$. In collaboration with prof. Tadeusz Stacewicz (Warsaw University) and Jacek Wojtas and prof. Zbigniew Bielecki (Military University of Technology), a sensitive detector (to the level of single *ppb*) of NO_x compounds was constructed, based on the Cavity Ring Down Spectroscopy (CRDS) and InGaN laser diode operating in the violet-blue spectral range.

- SUPERLUMINESCENT LIGHT EMITTING DIODES
  The second in the world (after Feltin *et al.* [148], EPFL) demonstration of

nitride SLEDs and a detailed study upon their temperature properties were provided.

- LASER DIODE ARRAYS
  The first in the world systematic characterization of nitride laser diode arrays was performed, in particular the issue of optical coupling between emitters was analyzed. It was found that the observed coherent emission from a multi-stripe device originated from the coupling through the substrate modes. Laser arrays with improved waveguide design featured independent emission from individual ridges. Optimized structure resulted in demonstration of high power devices - e.g. an array consisting of three emitters provided $2.5\,mW$ of optical output power.

- MEASUREMENT SETUP FOR NEAR- AND FAR-FIELD CHARACTERIZATION
  Based on the experience which I gained during my visit to Regensburg University (a collaboration with prof. Ulrich Schwarz), a construction of an experimental setup based on a Gaussian telescope for near-field and far-field measurements was provided. The setup is currently being used as a part of a standard characterization of devices fabricated at the Institute of High Pressure Physics, Polish Academy of Sciences and its *spin-off* TopGaN Ltd.

- FREQUENCY STABILIZED, TUNABLE EXTERNAL CAVITY LD
  A construction of a frequency stabilized laser diode was provided. The external cavity uses a $3600\,l/mm$ diffraction grating in Littrow configuration and an additional mirror providing a proper control of the output beam direction, when the operation wavelength is tuned. Stability of generation in this system is better than $100\,MHz$ within the time periods of $30\,min$ without any active feedback system. The construction meets the requirements to use this system as a light source to atomic spectroscopy at Doppler broadened lines, which usually are characterized by widths of $\sim\ GHz$.

Bibliography

[1] J.I. Pankove and E.A. Miller and J.E. Berkeyheiser. GaN Electroluminescent Diodes. *RCA Rev.*, 32:383, 1971.

[2] Wataru Utsumi, Hiroyuki Saitoh, Hiroshi Kaneko, Tetsu Watanuki, Katsutoshi Aoki, and Osamu Shimomura. Congruent melting of gallium nitride at 6 GPa and its application to single-crystal growth. *Nature Materials*, 2:735 – 738, 2003.

[3] H. P. Maruska and J. J. Tietjen. The preparation and properties of vapor-deposited single-crystal-line gan. *Applied Physics Letters*, 15(10):327–329, 1969.

[4] S. Nakamura, S. Pearton, and G.Fasol. *The Blue Laser Diode*. Springer-Verlag, Berlin, 2000.

[5] S. Yoshida, S. Misawa, and S. Gonda. Improvements on the electrical and luminescent properties of reactive molecular beam epitaxially grown gan films by using aln-coated sapphire substrates. *Applied Physics Letters*, 42(5):427–429, 1983.

[6] H. Amano, N. Sawaki, I. Akasaki, and Y. Toyoda. Metalorganic vapor phase epitaxial growth of a high quality gan film using an aln buffer layer. *Applied Physics Letters*, 48(5):353–355, 1986.

[7] S. Nakamura. GaN Growth Using GaN Buffer Layer. *Japanese Journal of Applied Physics*, 30:L1705–L1707, 1991.

[8] Hiroshi Amano, Masahiro Kito, Kazumasa Hiramatsu, and Isamu Akasaki. P-Type Conduction in Mg-Doped GaN Treated with Low-Energy Electron Beam Irradiation (LEEBI). *Japanese Journal of Applied Physics*, 28:L2112–L2114, 1989.

[9] S. Nakamura, T. Mukai, M. Senoh, and N. Iwasa. Thermal Annealing Effects on P-Type Mg-Doped GaN Films. *Japanese Journal of Applied Physics*, 31:L139–L142, 1992.

[10] Jörg Neugebauer and Chris G. Van de Walle. Atomic geometry and electronic structure of native defects in gan. *Phys. Rev. B*, 50(11):8067–8070, Sep 1994.

[11] Shuji Nakamura and Takashi Mukai. High-Quality InGaN Films Grown on GaN Films. *Japanese Journal of Applied Physics*, 31(Part 2, No. 10B):L1457–L1459, 1992.

[12] Shuji Nakamura, Takashi Mukai, Masayuki Senoh, Shin ichi Nagahama, and Naruhito Iwasa. $\mathrm{In_xGa_{1-x}N/In_yGa_{1-y}N}$ superlattices grown on GaN films. *Journal of Applied Physics*, 74(6):3911–3915, 1993.

[13] S. Nakamura, M. Senoh, S. Nagahama, N. Iwasa, T. Yamada, T. Matsushita, H. Kiyoku, and Y. Sugimoto. InGaN-Based Multi-Quantum-Well-Structure Laser Diodes. *Japanese Journal of Applied Physics*, 35:L74–L76, 1996.

[14] Shuji Nakamura, Masayuki Senoh, Shin ichi Nagahama, Naruhito Iwasa, Takao Yamada, Toshio Matsushita, Yasunobu Sugimoto, and Hiroyuki Kiyoku. Room-temperature continuous-wave operation of ingan multi-quantum-well structure laser diodes. *Applied Physics Letters*, 69(26):4056–4058, 1996.

[15] S. Nakamura, M. Senoh, S. Nagahama, N. Iwasa, T. Yamada, T. Matsushita, H. Kiyoku, Y. Sugimoto, T. Kozaki, H. Umemoto, M. Sano, and K. Chocho. InGaN/GaN/AlGaN-Based Laser Diodes with Modulation-Doped Strained-Layer Superlattices. *Japanese Journal of Applied Physics*, 36:L1568–L1571, 1997.

[16] S. Nakamura, M. Senoh, S. Nagahama, N. Iwasa, T. Yamada, T. Matsushita, H. Kiyoku, Y. Sugimoto, T. Kozaki, H. Umemoto, M. Sano, and K. Chocho. Violet InGaN/GaN/AlGaN-Based Laser Diodes with an Output Power of 420 mW. *Japanese Journal of Applied Physics*, 37:L627–L629, 1998.

[17] S. Nakamura, M. Senoh, S. Nagahama, T. Matsushita, H. Kiyoku, Y. Sugimoto, T. Kozaki, H. Umemoto, M. Sano, and T. Mukai. Violet InGaN/GaN/AlGaN-Based Laser Diodes Operable at 50C with a Fundamental Transverse Mode. *Japanese Journal of Applied Physics*, 38:L226–L229, 1999.

[18] L. A. Coldren and S. W. Corzine. *Diode Lasers and Photonic Integrated Circuits*. Willey Interscience, 1995.

[19] Hadis Morkoç. *Handbook of Nitride Semiconductors and Devices, Vol.3: GaN-based Optical and Electronic Devices*. WILEY-VCH Verlag GmbH & Co. KGaA, Weinheim, 2008.

[20] Hadis Morkoç. *Handbook of Nitride Semiconductors and Devices, Vol.1: Materials Properties, Physics and Growth*. WILEY-VCH Verlag GmbH & Co. KGaA, Weinheim, 2008.

[21] Shuji Nakamura, Masayuki Senoh, Shin ichi Nagahama, Naruhito Iwasa, Takao Yamada, Toshio Matsushita, Hiroyuki Kiyoku, Yasunobu Sugimoto, Tokuya Kozaki, Hitoshi Umemoto, Masahiko Sano, and Kazuyuki Chocho. InGaN/GaN/AlGaN-based laser diodes with modulation-doped strained-layer superlattices grown on an epitaxially laterally overgrown GaN substrate. *Applied Physics Letters*, 72(2):211–213, 1998.

[22] S. F. Chichibu, H. Marchand, M. S. Minsky, S. Keller, P. T. Fini, J. P. Ibbetson, S. B. Fleischer, J. S. Speck, J. E. Bowers, E. Hu, U. K. Mishra, S. P. DenBaars, T. Deguchi, T. Sota, and S. Nakamura. Emission mechanisms of bulk gan and ingan quantum wells prepared by lateral epitaxial overgrowth. *Applied Physics Letters*, 74(10):1460–1462, 1999.

[23] Jr. Jaime A. Freitas, Ok-Hyun Nam, Robert F. Davis, Gennady V. Saparin, and Sergey K. Obyden. Optical characterization of lateral epitaxial overgrown gan layers. *Applied Physics Letters*, 72(23):2990–2992, 1998.

[24] S. J. Rosner, G. Girolami, H. Marchand, P. T. Fini, J. P. Ibbetson, L. Zhao, S. Keller, U. K. Mishra, S. P. DenBaars, and J. S. Speck. Cathodoluminescence mapping of epitaxial lateral overgrowth in gallium nitride. *Applied Physics Letters*, 74(14):2035–2037, 1999.

[25] P. Kozodoy, J. P. Ibbetson, H. Marchand, P. T. Fini, S. Keller, J. S. Speck, S. P. DenBaars, and U. K. Mishra. Electrical characterization of gan p-n junctions with and without threading dislocations. *Applied Physics Letters*, 73(7):975–977, 1998.

[26] T. Mukai, K. Takekawa, and S. Nakamura. InGaN-Based Blue Light-Emitting Diodes Grown on Epitaxially Laterally Overgrown GaN Substrates. *Japanese Journal of Applied Physics*, 37:L839–L841, 1998.

[27] C. Sasaoka, H. Sunakawa, A. Kimura, M. Nido, A. Usui, and A. Sakai. High-quality ingan mqw on low-dislocation-density gan substrate grown by hydride vapor-phase epitaxy. *Journal of Crystal Growth*, 189-190:61 – 66, 1998.

[28] S. Nakamura, M. Senoh, S. Nagahama, N. Iwasa, T. Yamada, T. Matsushita, H. Kiyoku, Y. Sugimoto, T. Kozaki, H. Umemoto, M. Sano, and K. Chocho. High-Power, Long-Lifetime InGaN/GaN/AlGaN-Based Laser Diodes Grown on Pure GaN Substrates. *Japanese Journal of Applied Physics*, 37:L309 – L312, 1998.

[29] T. Paskova, E. M. Goldys, and B. Monemar. Hydride vapour-phase epitaxy growth and cathodoluminescence characterisation of thick GaN films. *Journal of Crystal Growth*, 203(1-2):1–11, 1999.

[30] T. Paskova, V. Darkchieva, P.P. Paskov, U. Södervall, and B. Monemar. Growth and separation related properties of HVPE-GaN free-standing films. *Journal of Crystal Growth*, 246:207–214, 2002.

[31] Izabella Grzegory. High pressure growth of bulk GaN from solutions in gallium. *Journal of Physics: Condensed Matter*, 13(32):6875, 2001.

[32] R. Dwilinski, R. Doradzinski, J. Garczynski andL.P. Sierzputowski, A. Puchalski, Y. Kanbara, K. Yagi, H. Minakuchi, and H. Hayashi. Bulk ammonothermal GaN. *Journal of Crystal Growth*, 311:3015–3018, 2009.

[33] R. Dwilinski, R. Doradzinski, J. Garczunska, L.P. Sierzputowski, M. Zajac, and M. Rudzinski. Homoepitaxy on bulk ammonothermal GaN. *Journal of Crystal Growth*, 311:3058–3062, 2009.

[34] E. Fred Schubert. *Light-Emitting Diodes*. Cambridge University Press, 2003.

[35] Hadis Morkoç. *Handbook of Nitride Semiconductors and Devices, Vol.2: Electronic and Optical Processes in Nitrides*. WILEY-VCH Verlag GmbH & Co. KGaA, Weinheim, 2008.

[36] I. Gorczyca, T. Suski, N. E. Christensen, and A. Svane. Limitations to band gap tuning in nitride semiconductor alloys. *Applied Physics Letters*, 96(10):101907, 2010.

[37] T. Matsuoka and N. Yoshimoto and T. Sasaki and A. Katsui. Wide-gap semiconductor InGaN and InGaAlN grown by MOVPE. *Jornal of Electronic Materials*, 21(2):157, February 1992.

[38] I. Ho and G. B. Stringfellow. Solid phase immiscibility in GaInN. *Applied Physics Letters*, 69:2701, 1996.

[39] Masaya Shimizu, Kazumasa Hiramatsu, and Nobuhiko Sawaki. Metalorganic vapor phase epitaxy growth of (inxga1-xn/gan)n layered structures and reduction of indium droplets. *Journal of Crystal Growth*, 145(1-4):209 – 213, 1994.

[40] Kozo Osamura, Shigehisa Naka, and Yotaro Murakami. Preparation and optical properties of ga[sub 1 - x]in[sub x]n thin films. *Journal of Applied Physics*, 46(8):3432–3437, 1975.

[41] L. K. Teles, J. Furthmüller, L. M. R. Scolfaro, J. R. Leite, and F. Bechstedt. First-principles calculations of the thermodynamic and structural properties of strained $InxGa1-xN$ and $AlxGa1-xN$ alloys. *Phys. Rev. B*, 62(4):2475–2485, Jul 2000.

[42] T. Sugahara, M. Hao, T. Wang, D. Nakagawa, Y. Naoi, K. Nishino, and S. Sakai. Role of Dislocation in InGaN Phase Separation. *Japanese Journal of Applied Physics*, 32:L1195–L1198, 1998.

[43] H. Sato, T. Sugahara, Y. Naoi, and S. Sakai. Compositional Inhomogeneity of InGaN Grown on Sapphire and Bulk GaN Substrates by Metalorganic Chemical Vapor Deposition. *Japanese Journal of Applied Physics*, 37:2013–2015, 1998.

[44] N. Wieser, O. Ambacher, H.-P. Felsl, L. Gorgens, and M. Stutzmann. Compositional fluctuations in gainn/gan double heterostructures investigated by selectively excited photoluminescence and raman spectroscopy. *Applied Physics Letters*, 74(26):3981–3983, 1999.

[45] K. Kojima, M. Funato, Y. Kawakami, H. Braun, U. Schwarz, S. Nagahama, and T. Mukai. Inhomogeneously broadened optical gain spectra of InGaN quantum well laser diodes. *physica status solidi (c)*, 5:2126–2128, 2008.

[46] M. Krysko, G. Franssen, T. Suski, M. Albrecht, B. Lucznik, I. Grzegory, S. Krukowski, R. Czernecki, S. Grzanka, I. Makarowa, M. Leszczynski, and P. Perlin. Correlation between luminescence and compositional striations in ingan layers grown on miscut gan substrates. *Applied Physics Letters*, 91(21):211904, 2007.

[47] J. E. Northrup, L. T. Romano, and J. Neugebauer. Surface energetics, pit formation, and chemical ordering in InGaN alloys. *Applied Physics Letters*, 74(16):2319–2321, 1999.

[48] T. Suski, E. Litwin-Staszewska, R. Piotrzkowski, R. Czernecki, M. Krysko, S. Grzanka, G. Nowak, G. Franssen, L. H. Dmowski, M. Leszczynski, P. Perlin, B. Lucznik, I. Grzegory, and R. Jakiela. Substrate misorientation induced strong increase in the hole concentration in Mg doped GaN grown by metalorganic vapor phase epitaxy. *Applied Physics Letters*, 93(17):172117, 2008.

[49] B. Yang, O. Brandt, A. Trampert, B. Jenichen, and K. H. Ploog. Growth of cubic GaN on Si(001) by plasma-assisted MBE. *Applied Surface Science*, 123-124:1–6, 1988.

[50] C.H. Wei, Z. Y. Xie, L. Y. Li, Q. M. Yu, and J. Edgar. MOCVD growth of cubic GaN on 3C-SiC deposited on Si (100) substrates. *Journal of Electronic Materials*, 29:317–321, 2000.

[51] M. Mizuta, S. Fujieda, Y. Matsumoto, and T. Kawamura. Low Temperature Growth of GaN and AlN on GaAs Utilizing Metalorganics and Hydrazine. *Japanese Journal of Applied Physics*, 25:L945–L948, 1986.

[52] O. Ambacher, J. Smart, J. R. Shealy, N. G. Weimann, K. Chu, M. Murphy, W. J. Schaff, L. F. Eastman, R. Dimitrov, L. Wittmer, M. Stutzmann,

W. Rieger, and J. Hilsenbeck. Two-dimensional electron gases induced by spontaneous and piezoelectric polarization charges in n- and ga-face algan/gan heterostructures. *Journal of Applied Physics*, 85(6):3222–3233, 1999.

[53] F. Bernardini, V. Fiorentinni, and D. Vanderbilt. Accurate calculation of polarization-related quantities in semiconductors. *Phys. Rev. B*, 63:193201, 2001.

[54] F. Bernardini and V. Fiorentinni. Spontaneous polarization and piezoelectric constants of III-V nitrides. *Phys. Rev. B*, 56:R10024–R10027, 1997.

[55] Alexei Bykhovski, Boris Gelmont, and Michael Shur. Strain and charge distribution in gan-aln-gan semiconductor-insulator-semiconductor structure for arbitrary growth orientation. *Applied Physics Letters*, 63(16):2243–2245, 1993.

[56] Alexei Bykhovski, Boris Gelmont, and Michael Shur. The influence of the strain-induced electric field on the charge distribution in gan-aln-gan structure. *Journal of Applied Physics*, 74(11):6734–6739, 1993.

[57] A. D. Bykhovski, B. L. Gelmont, and M. S. Shur. Elastic strain relaxation and piezoeffect in gan-aln, gan-algan and gan-ingan superlattices. *Journal of Applied Physics*, 81(9):6332–6338, 1997.

[58] Ch. Wetzel, T. Takeuchi, H. Amano, and I. Akasaki. Piezoelectric Stark-like Ladder in GaN/GaInN/GaN Heterostructures. *Japanese Journal of Applied Physics*, 38:L163–L165, 1999.

[59] F. Renner, P. Kiesel, G. H. Dohler, M. Kneissl, C. G. Van de Walle, and N. M. Johnson. Quantitative analysis of the polarization fields and absorption changes in ingan/gan quantum wells with electroabsorption spectroscopy. *Applied Physics Letters*, 81(3):490–492, 2002.

[60] D. A. B. Miller, D. S. Chemia, T. C. Damen, A. C. Gossard, W. Wiegmann, T. H. Wood, and C. A. Burrus. Band-Edge Electroabsorption in Quantum Well Structures: The Quantum-Confined Stark Effect. *Phys. Rev. Lett.*, 53:2173–2176, 1984.

[61] J. Wang, J.B. Jeon, Yu.M. Sirenko, and K.W. Kim. Piezoelectric effect on optical properties of pseudomorphically strained wurtzite GaN quantum wells. *IEEE Photonics Technology Letters*, 9:728–730, 1997.

[62] G. Franssen, T. Suski, P. Perlin, R. Bohdan, A. Bercha, W. Trzeciakowski, I. Makarowa, P. Prystawko, M. Leszczynski, I. Grzegory, S. Porowski, and S. Kokenyesi. Fully-screened polarization-induced electric fields in blue/violet InGaN/GaN light-emitting devices grown on bulk GaN. *Applied Physics Letters*, 87(4):041109, 2005.

[63] Andrea Reale, Gianluca Massari, Aldo Di Carlo, Paolo Lugli, Anna Vinattieri, Daniel Alderighi, Marcelo Colocci, F. Semond, N. Grandjean, and J. Massies. Comprehensive description of the dynamical screening of the internal electric fields of algan/gan quantum wells in time-resolved photoluminescence experiments. *Journal of Applied Physics*, 93(1):400–409, 2003.

[64] D. Fuhrmann, U. Rossow, H. Bremers, G. Ade, P. Hinze, and A. Hangleiter. Optimizing the internal quantum efficiency of GaInN SQW structures for green light emitters. *physica status solidi (c)*, 3:1966–1969, 2006.

[65] V. Bougrov, M. Levinshtein, S. Rumyantsev, and A. Zubrilov. *Properties of advanced semiconductor materials: GaN, AlN, InN, BN, SiC, SiGe.* John Willey & Sons, 2001.

[66] W. Götz, N. M. Johnson, J. Walker, D. P. Bour, and R. A. Street. Activation of acceptors in Mg-doped GaN grown by metalorganic chemical vapor deposition. *Applied Physics Letters*, 68(5):667–669, 1996.

[67] W. Götz, N. M. Johnson, C. Chen, H. Liu, C. Kuo, and W. Imler. Activation energies of Si donors in GaN. *Applied Physics Letters*, 68(22):3144–3146, 1996.

[68] Shuji Nakamura, Masayuki Senoh, Shin ichi Nagahama, Naruhito Iwasa, Takao Yamada, Toshio Matsushita, Yasunobu Sugimoto, and Hiroyuki Kiyoku. Ridge-geometry InGaN multi-quantum-well-structure laser diodes. *Applied Physics Letters*, 69(10):1477–1479, 1996.

[69] Ulrich T. Schwarz, Markus Pindl, Evi Sturm, Michael Furitsch, Andreas Leber, Stephan Miller, Alfred Lell, and Volker Härle. Influence of ridge

geometry on lateral mode stability of (Al,In)GaN laser diodes. *physica status solidi (a)*, 202(2):261–270, January 2005.

[70] Ulrich T. Schwarz and Bernd Witzigmann. *Nitride Semiconductor Devices: Principles and Simulation*, chapter Optical Properties of Edge-Emitting Lasers: Measurement and Simulation, pages 405–422. WILEY-VCH Verlag GmbH & Co. KGaA, 2007.

[71] M. J. Bergmann and H. C. Casey Jr. Optical-field calculations for lossy multiple-layer $Al_xGa_{1-x}N/In_xGa_{1-x}N$ laser diodes. *Journal of Applied Physics*, 84(3):1196–1203, 1998.

[72] M. Röwe, P. Michler, J. Gutowski, S. Bader, G. Brüderl, V. Kümmler, S. Miller, A. Weimar, A. Lell, and V. Härle. Influence of the Layer Design on the Far Field Pattern in GaN Based Laser Structures. *physica status solidi (a)*, 194(2):414–418, December 2002.

[73] T. Asano, T. Tojyo, T. Mizuno, M. Takeya, S. Ikeda, K. Shibuya, T. Hino, S. Uchida, and M. Ikeda. 100-mW kink-free blue-violet laser diodes with low aspect ratio. *IEEE Journal of Quantum Electronics*, 39(1):135–140, January 2003.

[74] Grennady A. Smolyakov and Marek Osiski. *Nitride Semiconductor Devices: Principles and Simulation*, chapter Resonant Internal Transverse-Mode Coupling in InGaN/GaN/AlGaN Lasers, pages 381 – 404. WILEY-VCH Verlag GmbH & Co. KGaA, 2007.

[75] Gen-ichi Hatakoshi. *Nitride Semiconductor Devices: Principles and Simulation*, chapter Fundamental characteristics of Edge-Emitting Lasers, pages 353–379. WILEY-VCH Verlag GmbH & Co. KGaA, 2007.

[76] D. A. Stocker, E. F. Schubert, W. Grieshaber, K. S. Boutros, and J. M. Redwing. Facet roughness analysis for ingan/gan lasers with cleaved facets. *Applied Physics Letters*, 73(14):1925–1927, 1998.

[77] A. T. Ping, I. Adesida, and M. Asif Khan. Study of chemically assisted ion beam etching of gan using hcl gas. *Applied Physics Letters*, 67(9):1250–1252, 1995.

[78] M. Kneissl, D. P. Bour, N. M. Johnson, L. T. Romano, B. S. Krusor, R. Donaldson, J. Walker, and C. Dunnrowicz. Characterization of AlGaInN diode lasers with mirrors from chemically assisted ion beam etching. *Applied Physics Letters*, 72(13):1539–1541, 1998.

[79] Shuji Nakamura, Masayuki Senoh, Shin ichi Nagahama, Naruhito Iwasa, Takao Yamada, Toshio Matsushita, Hiroyuki Kiyoku, Yasunobu Sugimoto, Tokuya Kozaki, Hitoshi Umemoto, Masahiko Sano, and Kazuyuki Chocho. Ingan/gan/algan-based laser diodes with cleaved facets grown on gan substrates. *Applied Physics Letters*, 73(6):832–834, 1998.

[80] M. P. Mack, G. D. Via, A. C. Abare, M. Hansen, P. K. Kozodoy, S. Keller, J. S. Speck, U. K. Mishra, L. A. Coldren, and S. P. DenBaars. Improvement of GaN- based laser diode facets by FIB polishing. *Electronic Letters*, 34:1315–1316, 1998.

[81] own AFM measurements.

[82] M. Asif Khan, C. J. Sun, J. W. Yang, Q. Chen, B. W. Lim, M. Zubair Anwar, A. Osinsky, and H. Temkin. Cleaved cavity optically pumped ingan–gan laser grown on spinel substrates. *Applied Physics Letters*, 69(16):2418–2420, 1996.

[83] P. Wisniewski, R. Czernecki, P. Prystawko, M. Maszkowicz, M. Leszczynski, T. Suski, I. Grzegory, S. Porowski, L. Marona, T. Swietlik, and P. Perlin. Broad-area high-power cw operated InGaN laser diodes. In David P. Bou and Carmen Mermelstein, editors, *Novel In-Plane Semiconductor Lasers V*, volume 6133 of *Proc. SPIE*, page 61330Q, 2006.

[84] M. Leszczynski, P. Prystawko, R. Czernecki, J. Lehnert, T. Suski, P. Perlin, P. Wisniewski, I. Grzegory, G. Nowak, S. Porowski, and M. Albrecht. III-N ternary epi-layers grown on the GaN bulk crystals. *Journal of Crystal Growth*, 231:352–356, 2001.

[85] B.W. Hakki and T.L. Paoli. cw egradation at 300 k of gaas double-heterostructure junction lasers. *Journal of Applied Physics*, 44:4113–4119, 1973.

[86] B.W. Hakki and T.L. Paoli. Gain spectra in gaas double-heterostructure injection lasers. *Journal of Applied Physics*, 46:1299–1306, 1975.

[87] U. T. Schwarz, E. Sturm, W. Wegscheider, V. Kummler, A. Lell, and V. Harle. Optical gain, carrier-induced phase shift, and linewidth enhancement factor in ingan quantum well lasers. *Applied Physics Letters*, 83(20):4095–4097, 2003.

[88] W.W. Chow and S.W. Koch. *Semiconductor Laser Physics*. Springer-Verlag, Berlin, 1994.

[89] D. Courjon. *Near-Field Microscopy and Near-Field Optics*. Imperial College Press, 2003.

[90] S. Rogowsky, H. Braun, U. T. Schwarz, S. Bruninghoff, A. Lell, and U. Strauss. Multidimentional near- and far-field characterization of broad ridge (al,in)gan laser diodes. *physica status solidi (c)*, 2009.

[91] T. Takeuchi, T. Detchprohm, M. Iwaya, N. Hayashi, K. Isomura, K. Kimura, M. Yamaguchi, H. Amano, I. Akasaki, Yw. Kaneko, R. Shioda, S. Watanabe, T. Hidaka, Y. Yamaoka, Ys. Kaneko, and N. Yamada. Improvement of far-field pattern in nitride laser diodes. *Applied Physics Letters*, 75(19):2960–2962, 1999.

[92] S. Uchida, M. Takeya, S. Ikeda, T. Mizuno, T. Fujimoto, O. Matsumoto, S. Goto, T. Tojyo, and M. Ikeda. Recent progress in high-power blue-violet lasers. *IEEE Journal of selected Topics In Quantum Electronics*, 9:1252 – 1259, 2003.

[93] Daniel Hofstetter, David P. Bour, Robert L. Thornton, and N. M. Johnson. Excitation of a higher order transverse mode in an optically pumped in[sub 0.15]ga[sub 0.85]n/in[sub 0.05]ga[sub 0.95]n multiquantum well laser structure. *Applied Physics Letters*, 70(13):1650–1652, 1997.

[94] W. W. Chow and H. Ammano. Analysis of lateral-mode behavior in broad-area InGaN quantum-well lasers. *IEEE Journal of Quantum Electronics*, 37:265, 2001.

[95] W. W. Chow, H. Amano, and I. Akasaki. Theoretical analysis of filamentation and fundamental-mode operation in InGaN quantum well lasers. *Applied Physics Letters*, 76(13):1647–1649, 2000.

[96] T. Swietlik, G. Franssen, R. Czernecki, M. Leszczynski, C. Skierbiszewski, I. Grzegory, T. Suski, P. Perlin, C. Lauterbach, and U. T. Schwarz. Mode dynamics of high power (inal)gan based laser diodes grown on bulk gan substrate. *J. Appl. Phys*, 101:083109, 2007.

[97] Markus Pindl and Ulrich T. Schwarz. Waveguide mode dynamics of blue laser diodes. *physica status solidi (a)*, 203:414–418, 2006.

[98] C. Eichler, D. Hofstetter, W.W. Chow, S. Miller, A. Weimar, A. Lell, and V. Harle. Microsecond time scale lateral-mode dynamics in a narrow stripe ingan laser. *Appl. Phys. Lett.*, 84:2473–2475, 2004.

[99] Marcin Sarzynski, Marcin Krysko, Grzegorz Targowski, Robert Czernecki, Agnieszka Sarzynska, Adam Libura, Wiktor Krupczynski, Piotr Perlin, and Michal Leszczynski. Elimination of algan epilayer cracking by spatially patterned aln mask. *Applied Physics Letters*, 88(12):121124, 2006.

[100] G.A. Smolyakov, P.G. Eliseev, and M. Osinski. Effects of resonant mode coupling on optical Characteristics of InGaN-GaN-AlGaN lasers. *IEEE Journal of Quantum Electronics*, 41:517–524, 2005.

[101] V. Laino, F. Roemer, B. Witzigmann, C. Lauterbach, U.T. Schwarz, C. Rumbolz, M.O. Schillgalies, M. Furitsch, A. Lell, and V. Härle. Substrate Modes of (Al,In)GaN Semiconductor Laser Diodes on SiC and GaN Substrates. *IEEE Journal of Quantum Electronics*, 43:16–24, 2007.

[102] S. Nagahama, N. Iwasa, M. Senoh, T. Matsushita, Y. Sugimoto, H. Kiyoku, T. Kozaki, M. Sano, H. Matsumura, H. Umemoto, K. Chocho, and T. Mukai. High-Power and Long-Lifetime InGaN Multi-Quantum-Well Laser Diodes Grown on Low-Dislocation-Density GaN Substrates. *Japanese Journal of Applied Physics*, 39:L647–L650, 2000.

[103] Peter Y. Yu and Manuel Cardona. *Fundamentals of Semiconductors:Physics and Materials Properties*. Springer Berlin Heidelberg New York, 2001.

[104] P. Perlin, E. Litwin-Staszewska, B. Suchanek, W. Knap, J. Camassel, T. Suski, R. Piotrzkowski, I. Grzegory, S. Porowski, E. Kaminska, and J. C. Chervin. Determination of the effective mass of gan from infrared reflectivity and hall effect. *Applied Physics Letters*, 68(8):1114–1116, 1996.

[105] M. Leszczynski, H. Teisseyre, T. Suski, I. Grzegory, M. Bockowski, J. Jun, S. Porowski, K. Pakula, J. M. Baranowski, C. T. Foxon, and T. S. Cheng. Lattice parameters of gallium nitride. *Applied Physics Letters*, 69(1):73–75, 1996.

[106] B. Lucznik, B. Pastuszka, I. Grzegory, M. Bockowski, G. Kamler, E. Litwin-Staszewska, and S. Porowski. Deposition of thick gan layers by hvpe on the pressure grown gan substrates. *Journal of Crystal Growth*, 281(1):38 – 46, 2005. The Internbational Workshop on Bulk Nitride Semiconductors III.

[107] H. Y. Ryu, K. H. Ha, J. K. Son, H. S. Paek, Y. J. Sung, K. S. Kim, H. K. Kim, Y. Park, S. N. Lee, and O. H. Nam. Comparison of output power of ingan laser diodes for different al compositions in the algan n-cladding layer. *Journal of Applied Physics*, 105(10):103102, 2009.

[108] G. M. Laws, E. C. Larkins, I. Harrison, C. Molloy, and D. Somerford. Improved refractive index formulas for the al[sub x]ga[sub 1 - x]n and in[sub y]ga[sub 1 - y]n alloys. *Journal of Applied Physics*, 89(2):1108–1115, 2001.

[109] T. Suski, G. Franssen, P. Perlin, R. Bohdan, A. Bercha, P. Adamiec, F. Dybala, W. Trzeciakowski, P. Prystawko, M. Leszczynski, I. Grzegory, and S. Porowski. A pressure-tuned blue-violet ingan/gan laser diode grown on bulk gan crystal. *Applied Physics Letters*, 84(8):1236–1238, 2004.

[110] Cunyun Ye. *Tunable External Cavity Diode Lasers*. World Scientific, 2004.

[111] A. Zybin, J. Koch, H. D. Wizemann, J. Franzke, and K. Niemax. Diode laser atomic absorption spectrometry. *Spectrochimica Acta B*, 60:1–11, 2005.

[112] H. Leinen, D. Glssner, H. Metcalf, R. Wynands, D. Haubrich, and D. Meschede. Gan blue diode lasers: a spectroscopists view. *Applied Physics B: Lasers and Optics*, 70:567–571, 2000. 10.1007/s003400050863.

[113] Lars Hildebrandt, Richard Knispel, Sandra Stry, Joachim R. Sacher, and Frank Schael. Antireflection-coated blue gan laser diodes in an external cavity and doppler-free indium absorption spectroscopy. *Appl. Opt.*, 42(12):2110–2118, 2003.

[114] Kazuhiro Hayasaka. Frequency stabilization of an extended-cavity violet diode laser by resonant optical feedback. *Optics Communications*, 206(4-6):401 – 409, 2002.

[115] S. Uetake, K. Hayasaka, and M. Watanabe. Saturation spectroscopy of potassium for frequency stabilization of violet diode lasers. *Japanese Journal of Applied Physics*, 42:L332, 2003.

[116] K. Toyoda, A. Miura, S. Urabe, K. Hayasaka, and M. Watanabe. Laser cooling of calcium ions by use of ultraviolet laser diodes: significant induction of electron-shelving transitions. *Opt. Lett.*, 26(23):1897–1899, 2001.

[117] T. Hard. Laser Wavelength Selection and Output Coupling by Grating. *Applied Optics*, 9:1825, 1970.

[118] A.M. Hennel. Temperature dependence of the energy gap in GaAs. *physica status solidi (a)*, 8:K111–K113, 1971.

[119] J. S. Blakemore. Semiconducting and other major properties of gallium arsenide. *Journal of Applied Physics*, 53(10):R123–R181, 1982.

[120] H. Teisseyre, P. Perlin, T. Suski, I. Grzegory, S. Porowski, J. Jun, A. Pietraszko, and T. D. Moustakas. Temperature dependence of the energy gap in gan bulk single crystals and epitaxial layer. *Journal of Applied Physics*, 76(4):2429–2434, 1994.

[121] A. S. Zubrilov, V. I. Nikolaev, D. V. Tsvetkov, V. A. Dmitriev, K. G. Irvine, J. A. Edmond, and Jr. C. H. Carter. Spontaneous and stimulated emission from photopumped gan grown on sic. *Applied Physics Letters*, 67(4):533–535, 1995.

[122] U. Tisch, B. Meyler, O. Katz, E. Finkman, and J. Salzman. Dependence of the refractive index of al[sub x]ga[sub 1 - x]n on temperature and composition at elevated temperatures. *Journal of Applied Physics*, 89(5):2676–2685, 2001.

[123] L. Viña, S. Logothetidis, and M. Cardona. Temperature dependence of the dielectric function of germanium. *Phys. Rev. B*, 30(4):1979–1991, Aug 1984.

[124] J. Petalas, S. Logothetidis, S. Boultadakis, M. Alouani, and J. M. Wills. Optical and electronic-structure study of cubic and hexagonal gan thin films. *Phys. Rev. B*, 52(11):8082–8091, Sep 1995.

[125] W. Shan, W. Walukiewicz, E. E. Haller, B. D. Little, J. J. Song, M. D. McCluskey, N. M. Johnson, Z. C. Feng, M. Schurman, and R. A. Stall. Optical properties of in[sub x]ga[sub 1 - x]n alloys grown by metalorganic chemical vapor deposition. *Journal of Applied Physics*, 84(8):4452–4458, 1998.

[126] T. Swietlik, G. Franssen, P. Wisniewski, S. Krukowski, S. P. Lepkowski, L. Marona, M. Leszczynski, P. Prystawko, I. Grzegory, T. Suski, S. Porowski, P. Perlin, R. Czernecki, A. Bering-Staniszewska, and P. G. Eliseev. Anomalous temperature characteristics of single wide quantum well ingan laser diode. *Applied Physics Letters*, 88(7):071121, 2006.

[127] H. Y. Ryu, K. H. Ha, S. N. Lee, T. Jang, H. K. Kim, J. H. Chae, K. S. Kim, K. K. Choi, J. K. Son, H. S. Paek, Y. J. Sung, T. Sakong, O. H. Nam, and Y. J. Park. Highly stable temperature characteristics of ingan blue laser diodes. *Applied Physics Letters*, 89(3):031122, 2006.

[128] J. Piprek, R. Kehl Sink, M.A. Hansen, J.E. Bowers, and S.P. DenBaars. Simulation and Optimization of 420 nm InGaN/GaN Laser Diodes. In *SPIE Proc.*, 2000.

[129] A. OKeefe and D. A. G. Deacon. Cavity ring-down optical spectrometer for absorption measurements using pulsed laser sources. *Rev. Sci. Instrum*, 59:2544 2551, 1998 1998 1998.

[130] A. OKeefe. Integrated cavity output analysis of ultra-weak absorption. *Chem. Phys. Letters*, 293:331–336, 1998.

[131] R. Engeln, G. Berden, R. Peeters, and G. Meier. Cavity enhanced absorption and cavity enhanced magnetic rotation spectroscopy. *Rev. Sci. Instrum*, 69:3763 3769, 1998.

[132] V.L. Kasyutich, C. S. E. Bale, C. E. Canosa-Mas, C. Pfrang, S. Vaughan, and R. P. Wayne. Cavity-enhanced absorption: detection of nitrogen dioxide and iodine monoxide using a violet laser diode. *Applied Physics B*, 76:691697, 2003.

[133] Giel Berden and Richard Engeln, editors. *Cavity Ring-Down Spectroscopy: Techniques and Applications*. Wiley-Blackwell, 2009.

[134] Kenneth W. Busch and Marianna A. Busch, editors. *Cavity-Ringdown Spectroscopy, An Ultratrace-Absorption Measurement Technique*. American Chemical Society, 1999.

[135] M. Herbelin, J. A. McKay, M. A. Kwok, R. H. Ueunten, D. S. Urevig, D. J. Spencer, and D. J. Benard. Sensitive measurement of photon lifetime and true reflectances in optical cavity by a phase-shift method. *Applied Optics*, 19:144147, 1980.

[136] A. M. Winer, J. W. Peters, J. P. Smith, and J. N. Pitts Jr. Response of commercial chemiluminescent nitric oxide-nitrogen dioxide analyzers to other nitrogen-containing compounds. *Environ. Sci Technology*, 8:1118–1121, 1974.

[137] W. A. McClenny, E. J. Williams, R. C. Cohen, and J. Stutz. Methods for ambient air monitoring of no, no2, noy, and individual noz species. *Journal of Air Waste and Management Associacions*, 52:542–562, 2002.

[138] V.L. Kasyutich, C.E. Canosa-Mas, C. Pfrang, S. Vaughan, and R.P. Wayne. Off-axis continuous-wave cavity-enhanced absorption spectroscopy of narrow-band and broadband absorbers using red diode lasers. *Applied Physics B*, 75:755–761, 2002.

[139] P. L. Kebabian, S. C. Herdon, and A. Freedman. Detection of nitrogen dioxide by cavity attenuated phase shift spectroscopy. *Anal. Chem.*, 77:724, 2005.

[140] J. Wojtas, A. Czyewski, T. Stacewicz, and Z. Bielecki. Detection of no2 using cavity enhanced methods. *Optica Applicata*, 36:461467, 2006.

[141] J. Wojtas and Z. Bielecki. Signal processing system in the cavity enhanced spectroscopy. *Opto-Electron. Rev*, 16:44–51, 2008.

[142] M. Nowakowski, J. Wojtas, Z. Bielecki, and J. Mikoajczyk. Cavity enhanced absorption spectroscopy sensor. *Acta Phys. Polonica*, 116:363–367, 2009.

[143] HITRAN database, http://www.cfa.harvard.edu/hitran.

[144]] D. R. Herriott, H. Kogelnik, and R. Kompfner. Off-axis paths in spherical mirror interferometers. *Applied Optics*, 3:523–526, 1964.

[145] K. K. Lehmann and D. Romanini. superposition principle and cavity ring-down spectroscopy. *J. Chem. Phys.*, 105:10263–77, 1996.

[146] J.M. Schmitt. Optical coherence tomography (OCT): a review. *IEEE Jouurnal of Sel. Top. Quantum Electronics*, 5:1205–1215, 1999.

[147] W.K. Burns, C. Chen, and R.P. Moeller. Fiber-optic gyroscopes with broadband sources. *Journal of Lightwave Technology*, 1:98–105, 1983.

[148] E. Feltin, A. Castiglia, G. Cosendey, L. Sulmoni, J.-F. Carlin, N. Grandjean, M. Rossetti, J. Dorsaz, V. Laino, M. Duelk, and C. Velez. Broadband blue superluminescent light-emitting diodes based on gan. *Applied Physics Letters*, 95(8):081107, 2009.

[149] G. A. Alphonse, D. B. Gilbert, M.G. Harvey, and M. Ettenberg. High-power superluminescent diodes. *IEEE Journal of Quantum Electronics*, 24:2454, 1988.

[150] M. Loeser and B. Witzigmann. Multidimensional Electro-Opto-Thermal Modeling of Broad-Band Optical Devices. *IEEE Journal of Quantum Electronics*, 44:505–514, 2008.

[151] K. Kincade. Diode lasers dominate prepress applications. *Laser focus world*, 41:145–151, 2005.

[152] D. Botez and D. R. Scifres. *Diode Laser Arrays.* Cambridge University Press, Cambridge, 2005 (second edition).

[153] S. Goto, T. Tojyo, S. Ansai, Y. Yabuki, T. Hino, H. Yamanaka, Y. Moriya, Y. Ito, Y. Hamaguchi, S. Uchida, and M.Ikeda. Super high output powerof 4.2 w in algainn-based blue violet laser diode array. In Y. Arakava, Y. Hirayama, K. Kishino, and H. Yamaguchi, editors, *Compound Semiconductors 2001*, volume 170 of *Proc. Of the 28th International Symposium on Compound Semiconductors, Tokyo*, pages 177–182, 2001.

[154] D. Botez, L. Mawst, P. Hayashida, T. J. Roth, and E. Anderson. Stable, single-(array)-mode operation from phase-locked, interferometric arrays of index-guided algaas/gaas diode lasers. *Appl. Phys. Lett.*, 52:266, 1988.

[155] D. Botez, P. Hayashida, L. Mawst, T. J. Roth, and E. Anderson. Diffraction-limited-beam, high-power operation from x-junction coupled phase-locked arrays of algaas/gaas diode lasers. *Appl. Phys. Lett.*, 53:1366, 1988.